Harri Merisaari

Algorithmic Analysis Techniques for Molecular Imaging

Turku Centre *for* Computer Science

TUCS Dissertations
No 217, November 2016

Algorithmic Analysis Techniques for Molecular Imaging

Harri Merisaari

To be presented, with the permission of the Faculty of Mathematics and Natural Sciences of the University of Turku, for public criticism in Publicum 3 on November 18, 2016, at 12 noon.

University of Turku
Department of Information Technology
Vesilinnantie 5, 20014 University of Turku, Finland

Turku PET Centre
and
Department of Diagnostic Radiology
and
Medical Imaging Center of Southwest Finland
Turku University Hospital
Kiinamyllynkatu 4-8, 20520 Turku, Finland

2016

Supervisors

Professor, PhD, Olli Nevalainen
Department of Information Technology
20014 University of Turku
Turku, Finland

Professor, PhD, Mika Teräs
Institute of Biomedicine, University of Turku
Department of Medical Physics, Turku University Hospital
Turku PET Centre, c/o Turku University Hospital, P.O. Box 52, 20521 Turku, Finland

Reviewers

Adjunct professor, PhD, Jussi Tohka
Department of Bioengineering and Aerospace Engineering
Universidad Carlos III de Madrid
Escuela Politécnica Superior, Avd. de la Universidad, 30. 28911 Leganés, Spain

UCL Academic Physics Head, Professor, PhD, Brian Hutton
Institute of Nuclear Medicine
University College of London
Institute of Nuclear Medicine, 5th floor, Tower
University College Hospital
235 Euston Road, London, United Kingdom

Opponent

Adjunct Professor, PhD Computer Science, Jussi Parkkinen
School of Computing
University of Eastern Finland
Joensuu Science Park, 3rd floor
Länsikatu 15, 80110 Joensuu, Finland

The originality of this thesis has been checked in accordance with the University of Turku quality assurance system using the Turnitin OriginalityCheck service.

ISBN 978-952-12-3442-2
ISSN 1239-1883

On an opening being made through the obstacle in the process of investigation, there results scientific contemplation
– The Stromata, Clement of Alexandria

Abstract

This study addresses image processing techniques for two medical imaging modalities: Positron Emission Tomography (PET) and Magnetic Resonance Imaging (MRI), which can be used in studies of human body functions and anatomy in a non-invasive manner.

In PET, the so-called Partial Volume Effect (PVE) is caused by low spatial resolution of the modality. The efficiency of a set of PVE-correction methods is evaluated in the present study. These methods use information about tissue borders which have been acquired with the MRI technique. As another technique, a novel method is proposed for MRI brain image segmentation. A standard way of brain MRI is to use spatial prior information in image segmentation. While this works for adults and healthy neonates, the large variations in premature infants preclude its direct application. The proposed technique can be applied to both healthy and non-healthy premature infant brain MR images. Diffusion Weighted Imaging (DWI) is a MRI-based technique that can be used to create images for measuring physiological properties of cells on the structural level. We optimise the scanning parameters of DWI so that the required acquisition time can be reduced while still maintaining good image quality.

In the present work, PVE correction methods, and physiological DWI models are evaluated in terms of repeatabilityof the results. This gives information on the reliability of the measures given by the methods. The evaluations are done using physical phantom objects, correlation measurements against expert segmentations, computer simulations with realistic noise modelling, and with repeated measurements conducted on real patients. In PET, the applicability and selection of a suitable partial volume correction method was found to depend on the target application. For MRI, the data-driven segmentation offers an alternative when using spatial prior is not feasible. For DWI, the distribution of b-values turns out to be a central factor affecting the time-quality ratio of the DWI acquisition. An optimal b-value distribution was determined. This helps to shorten the imaging time without hampering the diagnostic accuracy.

Acknowledgements

First, I want to thank my supervisors Professor Olli Nevalainen, and Professor Mika Teräs for their tireless guidance and encouragement through the completion of this work. I also wish to thank my former supervisor Mikko Kankaanpää, PhD for instructions in the beginning of the thesis project, and Jukka Teuhola, PhD, for giving valuable instructions and help when needed. I would like to thank the University of Turku, Turku Graduate School for Clinical Investigation, Instrumentarium Science Foundation, Nokia Science Foundation, State research funding for university-level health research of the Turku University Hospital and Turku University Science Foundation for making this work possible.

I want to thank the director of Turku PET Centre, Juhani Knuuti, and Turku PET Centre personnel with whom I worked during completion of this work. Their collaboration gave me valuable insight into the practical side of the data handling processes inside the hospital environment. I thank Professor Riitta Parkkola for collaboration with neonatal PIPARI cohort, and Professor Hannu Aronen for fruitful collaboration in the research of the prostate cancer.

I thank Ivan Jambor for close collaboration that led to various new insights related to DWI imaging. I thank my research collegues, Marco Bucci, Han Chunlei, Sergey Nesterov, Lauri Tuominen, Juho Joutsa, Jetro Tuulari and Aida Kiviniemi for giving instructions and support in their research fields, and I want to give special thanks to Vesa Oikonen for precious insight in modelling-related discussions.

My thanks go to various collegues and friends with whom I have spent time at work and leisure. My special thanks go to Sauli Piirola, Timo Laitinen and other IT team members. I thank various friends for being present in my life and for giving support, thus making it possible to rest in-between working on this thesis.

List of original publications

P1 Merisaari H., Teräs M., Hirvonen J., Nevalainen O.S., Hietala J., 2007. Evaluation of partial volume effect correction methods for brain positron emission tomography: Quantification and reproducibility, Journal of Medical Physics, 32(3), pp.108-117.

P2 Merisaari H., Parkkola R., Alhoniemi E., Teräs M., Lehtonen L., Haataja L., Lapinleimu H., Nevalainen O.S., 2009. Gaussian mixture model-based segmentation of MR images taken from premature infant brains, Journal of Neuroscience Methods, 182(1), pp.110-122.

P3 Jambor I., Merisaari H., Aronen H.J., Järvinen J., Saunavaara J., Kauko T., Borra R., Pesola M., 2014. Optimization of b-value distribution for biexponential diffusion-weighted MR imaging of normal prostate, Journal of Magnetic Resonance Imaging, 39(5), pp.1213-1222.

P4 Jambor I., Merisaari H., Taimen P., Boström P., Minn H., Pesola M., Aronen H.J., 2014. Evaluation of different mathematical models for diffusion-weighted imaging of normal prostate and prostate cancer using high b-values: A repeatability study, Magnetic Resonance in Medicine, 73(5), pp.1988-1998.

P5 Merisaari H., Jambor I., 2014. Optimization of b-value distribution for four mathematical models of prostate cancer diffusion-weighted imaging using b values up to 2000sec/mm^2: Simulation and repeatability study, Magnetic Resonance in Medicine, 73(5), pp.1954-1969.

P6 Toivonen J., Merisaari H., Pesola M., Taimen P., Boström P.J., Pahikkala T., Aronen H.J., Jambor I., 2015. Mathematical models for diffusion-weighted imaging of prostate cancer using b values up to 2000sec/mm^2: Correlation with Gleason score and repeatability of region of interest analysis, Magnetic Resonance in Medicine, 74(4), pp.1116-1124.

Contents

Nomenclature

$\mathcal{L}$ Likelihood of parameter setting with given data

ρ Spearman's rank correlation coefficient

AIC Akaike Information Criteria

AUC Area Under Curve of Receiver Operating Characteristics

CI Confidence Interval

e Euler's constant

$RMSE$ Root Mean Squared Error

SSR Sum of Squares Residual between model and the signal

TSS Total Sum of Squares distance to the signal mean

AD Alzheimer's disease

ADC Apparent Diffusion Coefficient

b-value Factor of Diffusion Weighted Imaging sequence

CNR Contrast to Noise Ratio, ratio between contrast of the image and noise

CR Coefficient of Repeatability

Cross Validation A technique to validate a model with cross-validation data that is separate from validation

CSF Cerebrospinal fluid

CT Computed Tomography

CV Coefficient of Variation

DCE-MRI Dynamic Contrast-Enhanced MRI, a MRI imaging technique involving injected contrast agent

DTI Diffusion Tensor Imaging

DWI Diffusion-Weighted Imaging

EM Iterative algorithm for finding parameters of statistical models

F-ratio F-test between two models using squared deviations to the observed data

FBP Filtered Back Projection algorithm

FDG PET tracer Fluorodeoxyglucose [^{18}F]

FOV Field Of View, region that is observed by an imaging system

Gleason score Grading of prostate cancer estimated visually

GM Brain gray matter

GoF Goodness of Fit of model to the data

Golden standard Method giving assumed perfect answer to which other methods are compared

i.i.d. independent, indentically distributed residuals, as assumption for statistical measure

ICC Intraclass Correlation Coeffcient

IVIM Intravoxel Incoherent Motion, a DWI model estimating two fast diffusion components

LOR Line Of Response joining two detectors in PET scanner

MAP Maximum A Posteriori estimate, a propbability estimate that can be used i. e. in image segmentation

MLE Maximum Likelihood Estimation, method for model optimization

Monte Carlo method An algorithm that uses repeated random sampling to obtain results.

MRF Markov Random Field, a model of a joint probability distribution

MRI Magnetic Resonance Imaging

MSE Mean Square Error

PCa Prostate Cancer

PET Positron Emission Tomography

PSF Point Spread Function, function describing displacements of intensity in imaging system

PVC Partial Volume Effect Correction

PVE Partial Volume Effect

R^2 Coefficient of Determination, indicating how well model fits to the data

RMSD Root Mean Squared Difference

ROC Receiver Operating Characteristics

ROI Region of Interest delineation in medical image for measurement

RSD Relative Standard Deviation

SNR Signal-to-Noise ratio

SPECT Single Photon Emission Computed Tomography

SSE Sum of Squared Error

SUV Standardized Uptake Value, general measure for uptake, used e. g. in PET tumour imaging

SVM Support Vector Machine, a model containing machine learned information about data

VOI Volume of Interest, 3D volume of interest as in ROI

WM Brain white matter

Chapter 1

Introduction

In the field of medicine, in addition to anatomical changes, the assessment of a disease is commonly based on changes on the cellular and molecular level. With molecular imaging one can identify states that are known to precede a particular disease or are signs of early stages of the disease. It also allows monitoring the effects of treatments and can be used to develop more efficient treatments for diseases. Molecular imaging is a general term for methods that produce images representing molecular level states of a target object. By the means of these methods, biological processes can be analysed *in vivo*. Molecular imaging aims to detect molecular and cellular changes in living tissues in a non-invasive manner, and it has currently a direct effect on patient care. The particular interest in molecular imaging is to find anomalies that are related to disease processes. There is currently a range of techniques that can be used for performing molecular imaging, creating images mainly at a specific region of the electromagnetic spectrum acquired from a target object.

Current modalities in molecular imaging include Positron Emission Tomography (PET), Single Photon Emission Computed Tomography (SPECT), Magnetic Resonance Imaging (MRI), and Computed Tomography (CT). The PET technique measures photons that travel to nearly opposite directions from a decaying radioactive molecule. A similar, more traditional technique is the SPECT, in which the emitted photons are measured [Dh2003]. Unlike PET, the SPECT is not so restricted to the availability of a nearby cyclotron that provides the source material for the radiolabelled tracers. In comparison to PET, SPECT has fewer tracers available, lower spatial resolution and sensitivity, which limit its usage, particularly in research. CT is another modality that involves radiation [Dh2003]. It has high contrast and is often used in conjunction to PET to give a corresponding anatomical reference image. MRI differs from the techniques above as it does not involve

radiation exposure, whereas the signal is acquired from changes in atomic spins under a large magnetic field.

As a specific application in this field, development of algorithms and optimisation of imaging sequences for quantification of Prostate Cancer (PCa) with Diffusion Weighted Imaging (DWI) of MRI can potentially have an effect on the treatment of PCa. Accurate characterisation of findings could have a major effect on the management of the disease. In brain imaging with PET, the quantification of Binding Potential [LaHu1997] of neuroreceptors can be improved by correcting the so-called Partial Volume Effect (PVE) in the images. In imaging the brains of small children, the large variations in the shape and size of the brain segments, and the existence of motion artefacts are challenging, since techniques to improve the image quality during scanning of infants are more limited than with adults. As an important step in the brain data analysis procedures, segmentation of the brain tissue of small children helps to build an understanding of brain development and related environmental factors.

1.1 Image Analysis

Reconstructed medical images may contain 3D or 4D information. In PET, the 4th dimension represents the time and for DWI, the 4th dimension stands for the gradient weighting which relates to the distance which the water molecule travels in the random walk like manner [Dh2003]. The 3D or 4D images are created in a workstation that accompanies the scanning device, even though the image reconstruction can also be performed elsewhere. The images are stored and analysed in the DICOM [Gr2005] data format, which contains essential information about data interpretation, additional information on the target subject and image acquisition process. All vendors offering imaging devices are required to provide a DICOM 3.3 Conformance statement [Na2011], which describes which parts of the DICOM standard their device supports. In principle, the DICOM data can be analysed in conventional personal computers or workstations. However, for quality reasons, in a clinical setting, the imaging data has to be analysed by an expert using a system which includes specific software (operating system, libraries, application) and hardware (CPU, high performance display device(s) for viewing). The performance of the imaging system has to be validated according to some international standard, such as the US Food and Drug Administration (FDA) in the U.S., or CE marking for MEdical Devices in Europe. While reliable quantitative and qualitative measures depend on the whole process starting from the image acquisition, software constitutes a fundamental part of the total imaging system, thus imposing the need for rigorous validation procedures regarding the software components [Le2006].

1.2 Structure of the Thesis

The data acquisition processes of PET and MRI are explained in Chapter 2, followed by a brief description of the physiological models of the techniques in Chapter 3. The data analysis techiniques of PET and MRI are surveyed in Chapter 4 followed by a literature review of these in Chapter 5. In chapter 6, the main effects that hamper the quantification of PET and MRI are explained. Chapter 7 gives a summary of the main results of the publications included in this work, which are then discussed in Chapter 8.

1.3 Aims of the Thesis

This thesis work addresses the analysis techniques of medical image data of PET and MRI devices. In PET imaging, repeatability of the kinetic model parameters can be improved by proper selection of the Partial Volume Effect (PVE) correction method, that recovers lost activity concentration.

In this study, a set of PVE correction methods are evaluated for brain PET images. For MRI, a new segmentation method that does not utilise atlas is developed for premature infant T1 weighted data. Finally, for Diffusion Weighted Imaging (DWI) of prostate in MRI, repeatability is improved by a design of the data acquisition setting in terms of gradient field weightings that are suited to the accompanying DWI model. Improved repeatability allows more reliable separation of normal and abnormal states in the prostate, and characterization of abnormal states in terms of severity of the cancer.

The main aims of this thesis are:

1. Evaluation of Partial Volume Effect (PVE) correction techniques for repeatability in brain PET studies
2. Segmentation algorithm for premature infant brain MR images
3. Methodological improvements for DWI of prostate MRI in terms of model evaluation and optimization of b-value distribution

Chapter 2

Principles of Image Formation

This work aims to present methods for analysing medical imaging data in a reliable manner that will eventually allow improved diagnostic accuracy. For PET and MRI we evaluate image analysis algorithms using image sets of humans and phantoms, whereas for DWI, the diagnostic accuracy is addressed by AUC which is described in Chapter 3. In order to achieve this, the methodologies themselves need to be studied, and are presented here in short detail. In section 2.1, we explain the principle of PET detection and reconstruction. In section 2.2, we discuss how information at a molecular level can be acquired by imaging spins of protons, i. e. by using the MRI technique. As there are various MRI scanning sequences, two basic ones are explained in section 2.2.1, while a more dedicated sequence that measures specifically the diffusion of water molecules, is explained in section 2.2.2.

2.1 Positron Emission Tomography Image Data Acquisition

Positron Emission Tomography (PET) technique measures the amount of (gamma) photons emitted as a result of a decaying process of radioactive isotopes [Dh2003]. The strength of PET is in the accuracy and sensitivity of measurements of molecular quantities. On the other hand, its main limitation is the relatively poor spatial resolution, affectedby the Partial Volume Effects (PVE). The organ movements (such as respiratory movement) and PVE together reduce the precision of the acquired data.

The PET technique uses a small amount of radioactively labelled molecules, i. e. a tracer that is inserted into the biological system under study by the means of injection, or inhalation. The tracer functions as its natural stable analog, which allows the imaging of various different functions of a living

organisms, depending on the tracer in question. Currently, there are a great number of PET tracers available both for clinical and for research use. The most common use of PET is in the detection and therapy responce of cancer.

2.1.1 Detection of Positron Emitters in PET

The source of information in a PET image is the decaying nucleus of radioactive isotopes (i. e. radioisotopes). The isotopes are commonly placed into a substance that is found in the biological system under study. When an isotope in molecule is replaced, the resulting molecule is called radiotracer. The most common radiotracer in PET is Fluorodeoxyglucose [^{18}F]FDG which is a glucose analog.

The production of a radiotracer starts with a cyclotron that produces radioactive nuclides, which are synthesized in a hot cell to radiolabelled molecules. The process is conducted according to Good Manufacturing Practise (GMP) [Eu2009] to allow injecting the resulting radiopharmaceutical safely into the subject prior to actual scanning with a PET, PET/CT or PET/MR device.

In the imaging process, the nucleus of an isotope decays and emits a positron, which then combines with an electron after travelling a short distance which depends on the excitation energy of the nuclide. When the travelling positron and an electron combine, they annihilate resulting in two photons travelling in nearly opposite directions (up to 0.25°). These photons are then detected with a cylindrical PET scanner as coincidence events, consisting of information about paired detectors located cylindrically. A straight line between a pair of detector pair is called a line of response (LOR). The activated LORs are stored in the computer memory. After acquiring a large number of events (conventionally 1-10 million) all LORs are histogrammed to a so-called sinogram (see Fig. 2.1).

2.1.2 Reconstruction of Event Data to 3D/4D Images

The sinograms from 2D planes (forming image slices) perpendicular to the scanner z-axis (straight line going through the scanner cylinder) and 2D planes at different angles are further reconstructed into a 3D image for visualization and further analysis, see Figure 2.2 for illustration of the process.

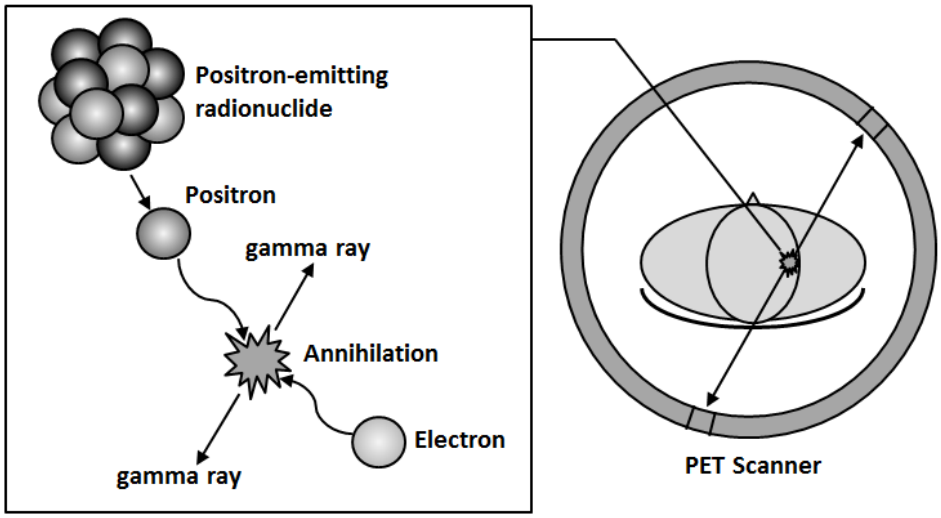

Figure 2.1: Illustration of the PET imaging process. A radionuclide emits a positron, which collides with an electron after travelling some distance (0-2 mm). In the collision, after annihilation, the resulting two gamma rays (photons) travel in nearly opposite directions. These events take place in the subject under study, and gamma rays are detected with a PET scanner, with which a 3D image can then be reconstructed.

The acquired sinogram contains several error factors which must be corrected before image reconstruction. Random events means that sometimes a coincidence is detected, which did not originate from a single annihilation, but instead from two distinctive random annihilations that were detected simultaneously. Attenuation and scatter depend on the subtances that are located between the annihilation event and the detectors, where attenuation causes reduction in the number of detected gamma photons, and scatter causes detection in a wrong detector, thus hampering proper localization of the annihilation events. A scanner device has limits in its sampling frequency for recording valid coincidence events. This effect is called the deadtime and it causes underestimation of intensities in the reconstructed PET image.

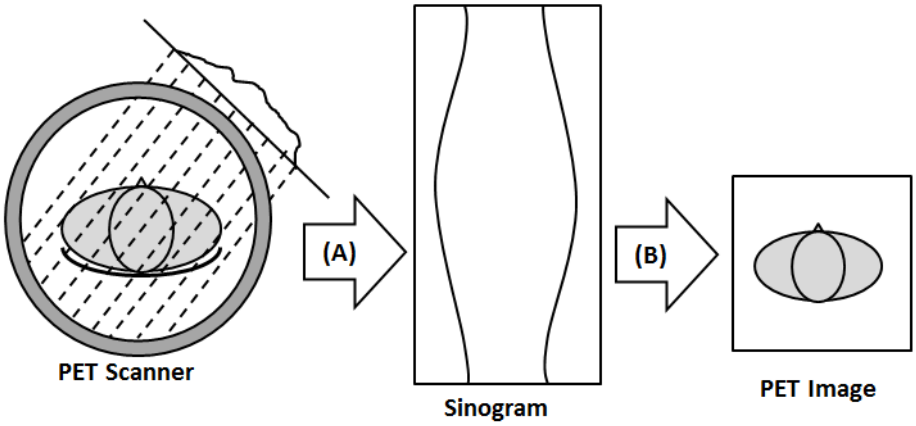

Figure 2.2: PET image reconstruction process. First, photons that are observed in PET scanner detectors are recorded as a sinogram (A). In the sinogram, each horizontal line of the sinogram has LORs at a particular angle. The sinograms are reconstructed to a static image volume with a reconstruction algorithm (B). The process can be repeated within various consecutive time windows, thus composing a time series of 3D images (i. e. dynamic imaging (4D)).

After sinograms have been corrected for random events, attenuation, scatter and deadtime, they are reconstructed to a 3D image. Mathematically, the sinogram data are acquired in the Radon space [Ra1917,De2007]. Each 2D slice can therefore be reconstructed as its corresponging xy-slice in spatial space with the inverse Radon transform

$$f(x,y) = \int_0^{\pi} \hat{g}(x * cos(\theta) + y * sin(\theta), \theta) d\theta \tag{2.1}$$

where $f(x,y)$ is the intensity of a 2D slice at the position (x,y), and $\hat{g}(s,\theta)$ is the filtered Radon domain signal of $g(s,\theta)$, and s is the location at the projection angle θ in $[0..\pi]$. In practise, the data are reconstructed as discrete approximation of Eq. 2.1.

Inversion of the Radon transform can be done in several ways. A commonly used technique for this is the Filtered Back Projection (FBP) [ShLo1974].

In present devices, an iterative Ordered Subsets Expectation Maximization (OSEM) [HuLa1994] approach is used instead of FBP. In the iterative OSEM reconstruction, the basic reconstruction step is iterated several times in order to get a better quantitative result. Another more recent approach uses a more complex system matrix to describe the relationship between the image space and the projection space, including position variant resolution. Further, in the newest reconstruction techniques, this kind of system matrix is utilized during each iteration of the reconstruction [Ir2016].

2.2 Magnetic Resonance Imaging

The Magnetic Resonance Imaging (MRI) technique is based on the detection of protons subjected to a large magnetic field. In this situation, nuclear spins of protons alter their direction and their radio frequency radiation is observed when the spins return to their original states under the large magnetic field. MRI provides structural and physiological information about the target tissue, but without involvement of ionising radiation. In MRI, the images give information about locations and properties of atomic nuclei, most commonly hydrogen nuclei H^1.

The image data of MRI are three or four dimensional like in PET. The fourth dimension depicts some characteristics of the scanning sequence (such as the b-value to be explained later), or time in the case of using a contrast agent (e. g. Gadolidium). Figure 2.3 (right) shows a charged proton with the direction of magnetic moment depicted by an arrow. When there is no external magnetic field affecting the nuclei, the orientations of the magnetization fields are completely random (A). However, when the target object is placed into a MRI scanner, the nuclei in the object have their magnetic fields aligned with (either along or against) the so-called B_0 field that is constantly present in the scanner (Fig. 2.3 (B)).

When the target object reaches a thermal equilibrium in the presence of the B_0 field, there are slightly more nuclei orientation along the B_0 than against it, which generates a net magnetization vector along the B_0 field. Then, a radiofrequency (RF) pulse can be transmitted to the object. The frequency of the pulse is determined by the gyromagnetic ratio of the target nuclei. The RF pulse affects the nuclei so that some of the nuclei oriented along B_0 flip their alignment against it. This results in a change in the net magnetization vector so that its orientation now deviates from the static B_0 field. With specific types of RF pulses the net magnetization field can be flipped in specific directions. This, in combination with the reading of the energy emitted during the relaxation process of the nuclei back to orientation along the B_0 field, allows the creation of various scanning sequences that reveal specific information about the locations and physiological properties of the target object.

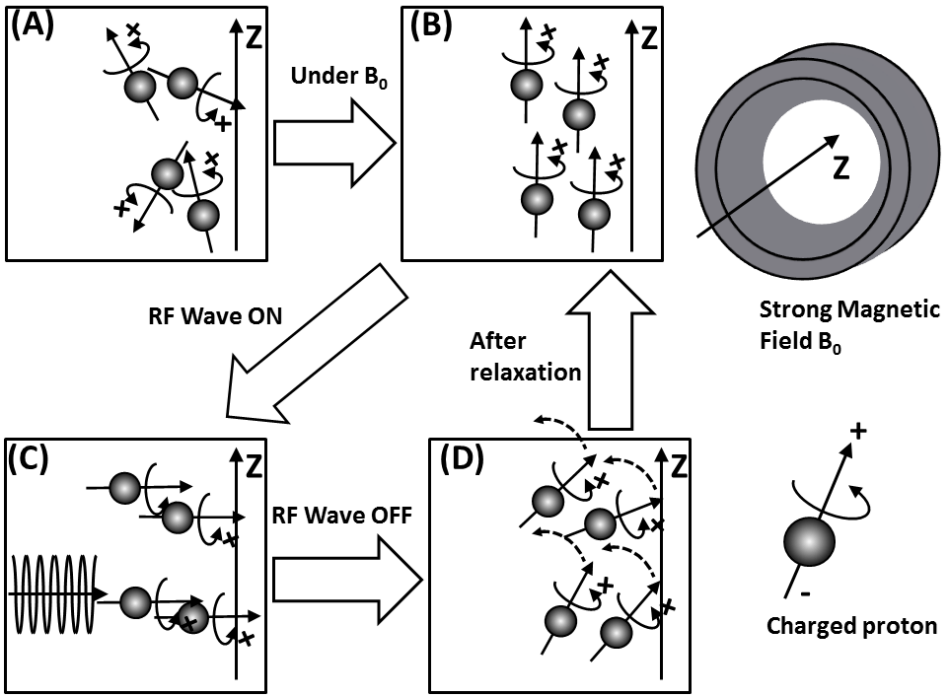

Figure 2.3: Principle of Magnetic Resonance Imaging (MRI). First, the spins of the protons are randomly oriented (A), but when brought under the effect of a strong magnetic field B_0 (Z) that is constantly on, they become aligned (B). A radiofrequency wave is used to flip the spins from the alignment (C). When the radiofrequency is turned off, the spins return back to equilibrium (D, relaxation to alignment with B_0), which can be measured by receiver coil in the MRI scanner.

Using different MRI pulse RF sequences, it is possible to reveal different characteristics at the molecular level, such as motion of the molecules and proton density, which furthermore can be utilised as indirect indicators of other features of the tissue. The Signal-to-Noise Ratio (SNR) [Di2007] of these observations can furthermore be enhanced by injecting so-called contrast agents, which react specifically to the magnetization field due to their particular paramagnetic characteristics. In total, normal anatomical MRI sequences have higher spatial resolution and soft tissue contrast in comparison to PET. However, the main challenges in MRI imaging are noise and various imaging artefacts that hinder more accurate measurements.

2.2.1 Principle of T1 and T2 Imaging

T1- and T2- imaging are basic MRI imaging techniques, which reveal different characteristics about tissues The T1 signal represents the amount of time that is required for proton spins in water molecules to return to the alignment with the B_0 field. The T2 represents the loss of coherence in the water molecule spins after ceasing of the RF pulse that caused them to be in the same phase. In terms of magnetization vectors $(M_z, M_{x,y})$, the T1 and T2 signals can be expressed as [Dh2003]:

$$M_z(t) = M_z^0 * (1 - e^{-t/T_1}) + M_z(0) * e^{-t/T_1} \tag{2.2}$$

$$M_{x,y}(t) = M_{x,y}(0) * e^{-t/T_2} * e^{-i*\omega_0*t}$$

where (2.3)

$$M_{x,y}(0) = M_{x',y'}(0) * e^{-i*\omega_0*\tau_p}$$

In (2.2), t is time, and T_1 refers to "longitudinal relaxation" by which the net magnetization returns to the alignment with the B_0 field with original maximum value M_z^0 of the vector. Correspondingly, T_2 in (2.3) refers to "transverse relaxation", loss of dephasing of spins that makes the total net sum magnetization vector of all spins to deviate from zero. $M_{x,y}(0)$ is the initial transverse magnetization vector at time zero. τ_p is the RF pulse duration. For the transverse relaxation, ω_0 is Larmor frequency which refers to the rate of precession of the spin axis around the direction of B_0. The frequency is related to the field strength of B_0 and gyromagnetic ratio of the imaged nuclei.

The T1 and T2 signals are used to recognize various pathologies in the target tissue. For brain imaging, T1 is often favoured due to its better Contrat to Noise Ratio (CNR) between brain gray and white matter, while T2 can be used for separating the skull from the brain tissue. See Fig. 2.4 for sample images of T1 and T2 weighted images in premature infant brain.

T1 and T2 images are not to be confused with other techniques such as T1-weighted imaging (T1*) and T2-weighted imaging (T2*) (not presented here).

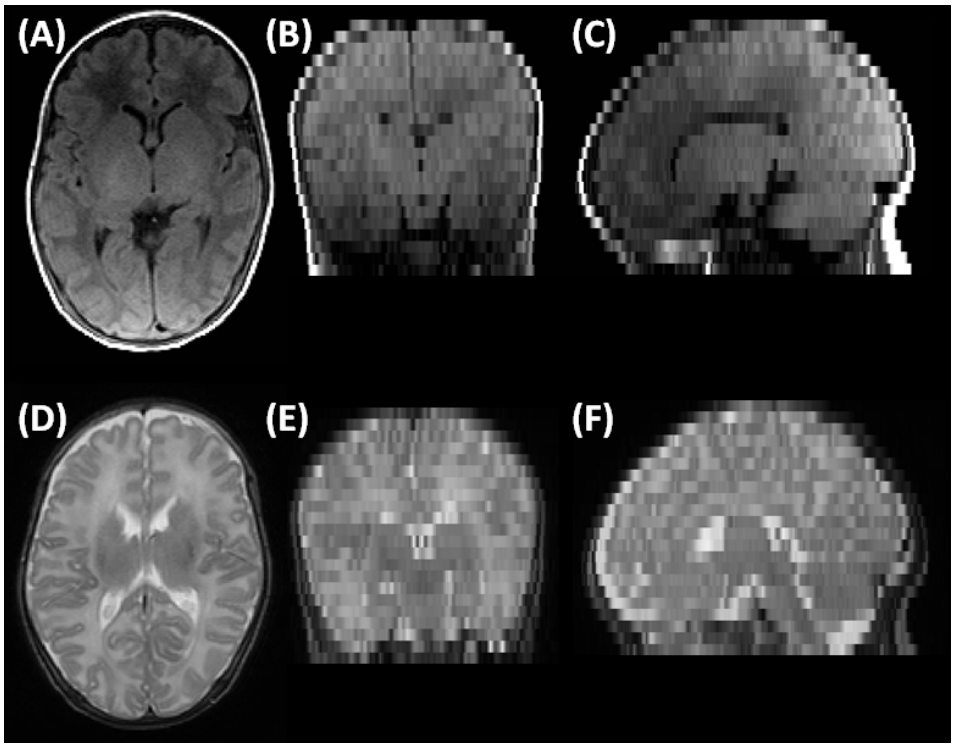

Figure 2.4: T1 and T2 -images of premature infant brain. Top row: T1-image. Bottom row: T2-image. Slice orientations are (A,D) transaxial, (B,E) coronal, (C,F) sagittal (1.5T Philips Intera, Philips Medical Systems, Best, the Netherlands).

2.2.2 Principle of Diffusion Weighted Imaging

Diffusion Weighted Imaging (DWI) [Mo1990, Ha2006] is a MRI technique that is targeted to reveal the proton mobility. The attenuation in the mobility of water protons can be used to characterize cellular properties such as cell density, cell boundaries, and shapes such as tubular shapes of nerve fibres in brain. The displacements of the water molecules appear in three modes. Completely *free diffusion* is Brownian motion, i. e. random thermal displacements of the molecules in the absence of any restrictions. When occuring in tissue, the displacements may be slowed down due to constant hinderance, causing *hindered diffusion*. Lastly, when the displacements may are completely blocked by the structure, *restricted diffusion* occurs. In practise, the measured attenuation in the DWI signal is often a mixture of these, and restriction of the diffusion may apply more to one orientation than to another. Figure 2.5 illustrates two types of diffusion; completely free diffusion (on the left) where the distribution of particle displacements is spherical, and

diffusion under tubular boundaries (on the right) which causes the shape of the distribution to be ellipsoid, i. e. anisotropic. Isotropic diffusion can be assumed for some tissue such as prostate [Re2005], while brain white matter contains fibers which cause anisotrophic diffusion.

An essential difference from conventional MRI (T_1, T_2) that utilises the H^1 signal from water is that the DWI signal presented in this section is based on the displacements of water mocelules. The technique is currently in widespread clinical use.

Expressed in terms of the magnetization vectors with T_1 and T_2, the diffusion can be explained by the Bloch-Torrey equation [To1956] as:

$$\frac{dM}{dt} = \gamma(M * B) - \frac{M_x \overrightarrow{i} + M_y \overrightarrow{j}}{T_2} - \frac{(M_z - M_0)\overrightarrow{k}}{T_1} + \bigtriangledown * (D \bigtriangledown M),$$

where

$$D = \begin{bmatrix} D_{xx} & D_{yx} & D_{zx} \\ D_{xy} & D_{yy} & D_{zy} \\ D_{xz} & D_{yz} & D_{zz} \end{bmatrix} \tag{2.4}$$

There, M is the vector defining the orientation of the spin in the (x,y,z)-space and D is the 3x3 matrix of diffusion tensor. Product $(D \bigtriangledown M)$ denotes the flow of particles in spin direction and $\bigtriangledown * (D \bigtriangledown M)$ is the rate of change in the concentration of particles. γ is the gyromagnetic ratio of the target particle or system.

In the case of DWI, the variable D is a scalar multiplied by a 3x3 identity matrix (i. e. all tensor directions have the same magnitude). Assuming that the diffusion occurring in the target tissue is isotropic (Fig. 2.5 left panel), three averaged measurements of orthogonal directions are conventionally used in DWI for defining D.

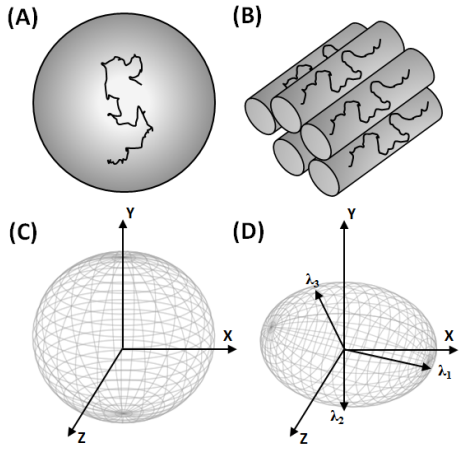

Figure 2.5: Principle of Diffusion Weighted Imaging (MRI). (A) Brownian motion in case of free diffusion. (B) Brownian motion in tissue with boundaries (here, tubular shapes). (C) Diffusion kernel in isotropic diffusion that is utilised in DWI. (D) Diffusion kernel in non-isotropic diffusion.

In Diffusion Tensor Imaging (DTI), a minimum of six directions are required to reconstruct the distribution of the ellipsoid shape (see Fig. 2.5 right panel). The signal is measured with two pulsed gradient fields. The first pulse makes the spins deviate (dephase). The second pulse cancels the first one in case of non-moving water molecules, but for freely moving protons (i. e. free diffusion) random phase shifts occur which causes signal attenuation without an altering phase shift (Eq. 2.3). For describing the phase shift of the molecules leads to signal attenuation. The so-called Diffusion sensitizing factor (b, i. e. b-value [s/mm^2]) can be used to describe the attenuation of the signal. The b-value is calculated for a spin echo sequence with the Stejskal-Tanner equation [StTa1965] as:

$$b = \gamma^2 * G^2 * \delta^2 * (\Delta - \frac{\delta}{3}), \tag{2.5}$$

where δ is the duration of the pulsed gradient field, G is the strength of the gradient and Δ is the time interval between two gradient pulses (see Fig. 2.6 for a diagram of pulse sequence). The DWI signal intensity decays with increased b-value, which represents restriction of the tissue to the free diffusion (see Figure 3.1, top row for examples of b-value images).

The signal intensity of the b-value depends on restricted mobility of the water protons in relation to free diffusion. In addition to diffusion, the strength of the gradient G in Eq. 2.5, and T2-relaxation time at higher b-values (e. g. b-values higher than 500 s/mm^2) also affect the signal [Ko2010]. Both of these effects can be addressed by measuring the amount of decay be-

tween the b-values. The easiest method for this is the calculation of the slope of mono-exponential fit of the signal, which is called the Apparent Diffusion Coefficient (ADC). The number of b-values required for ADC calculation is two at minimum (b=0 and one non-zero b-value), but more b-values are needed depending on the DWI model in question.

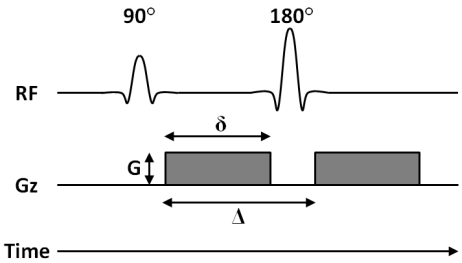

Figure 2.6: Pulse sequence diagram of Diffusion Weighted Imaging (DWI). RF: radiofrequency pulses. Gz: gradient pulses. Two diffusion sensitizing gradients (dark gray) are applied before and after 180° refocusing pulse. G: amplitude of diffusion gradient (millitesla/meter). δ: duration of the diffusion gradient (milliseconds). Δ: time interval between onset of the first and second gradient pulses (milliseconds).

Chapter 3

Quantification of the Physiological Parameters

The information in the medical imaging data is most commonly transformed into some clinically relevant output, preferably to measures of some physiological quantities. In order to obtain these measures, a model of the underlying physical and biological processes must be assumed. The model parameters are then adjusted so that the representation of the data with the model is as close as possible to what is observed. In PET, interaction of components of a natural system together with the decay of radioactive substance defines how the spatio-temporal signal behaves. This signal can be represented by Time Activity Curves (TAC), and then analysed with kinetic modelling. For DWI, decay curves generated from measurements with different b-values are affected by the movement of water molecules in time. Finally, after fitting a model to the data, the parameters of the model can be used to determine the underlying physiological state of the tissue under study.

3.1 Analysis of the Parameter Values

Conventionally, a Region of Interest (ROI) is delineated on the original data. If available, anatomical reference data of the same object can be aligned to match the position and orientation of the data modelled, and a visualization of the results can be created to help ROI delineation. The analysis of the data can be based on the mean or voxelwise intensities of the ROI. The first approach (use of mean intensities) is more widely used in research. In the voxelwise approach parameters of the model are determined for each individual voxel and statistics can be determined inside the ROI. Voxelwise analysis can also be applied to a so-called *parameter map* where each voxel represents a model parameter value calculated from the signal intensity curve

(e. g. b-value in DWI) at that location. If the SNR and resolution are high enough, this potentially allows us to perform additional analysis of the image data, such as texture [Ch2013, Ca2004] and shape analysis [Le2009].

In order to avoid inter-reader variability, automatic ROI placement (i. e. segmentation of organ area) can be applied to the image data, if a suitable segmentation algorithm is available for the medical image modality in question. For conventional adult MR T1 brain images, various segmentation techniques (e. g. "New Segment" tool in SPM8 [AsFr2005]) are available. On the other hand, for brain images with anomalies or in small children with different contrasts and motion artefacts the situation is more complicated, because a universal model is hard to create. A common technique is to use a standard brain map which is morphologically matched to the image [Ca2011]. Some efforts have recently been made to build such templates and use them for segmentation of normal brain images [Ku2011, Ha2010, WaKuSc2012]. This technique is however not so usable in cases with greater deviation from the standard shape, e. g. in anomalies (such as tumour) in the brain structure. For moving tissues such as the heart, the segmentation is difficult to carry out due to motion and PVE and other effects that lower the SNR (i. e. shorter scanning times at the cost of lowered SNR).

3.2 Modelling of the DWI Signal

In DWI, the signal is commonly modelled with one or more exponential functions. Apart from analytical methods, the simplest exponential model of the signal intensity $S(b)$ for a given gradient weighting b (i. e. b-value) is mono-exponential [Le1986, Th2007]:

$$S(b) = S(0) * e^{-b*ADCm}, \tag{3.1}$$

where $ADCm$ denotes Apparent Diffusion Coefficient of monoexponential decay. The ADC can be considered to correlate negatively with the density of the tissue. In addition to the $ADCm$, kurtosis K of the Gaussian probability function for displacement of water molecules can be modelled with a kurtosis model:

$$S(b) = S(0) * e^{-b*ADCk+\frac{1}{6}*b^2*ADCk^2*K} \tag{3.2}$$

The K parameter shows deviation from pure monoexponential decay, and can be understood to correspond to the amount of structure within the tissue [Je2005]. The third model for the decay curve is the so-called stretched model:

$$S(b) = S(0) * e^{-(b*ADCs)^{\alpha}}, \tag{3.3}$$

where α varies between 0 and 1. Smaller α-values indicate larger deviation from mono-exponential decay, i. e. the signal consists of multiple mono-exponentials in multiple water pools [Be2004]. For measuring separately two exponential components of the DWI curve for perfusion (occurring at b-values from 0 to around 150 s/mm^2) and so-called slow (from 0 to around 500) and fast diffusion (from 500 s/mm^2 onwards), a bi-exponential model can be used:

$$S_{IVIM}(b) = S(0) * (f_{IVIM} * e^{-b*D_{perfusion}} + (1 - f_{IVIM})e^{-b*D_{fast}})$$

$$S_{biexp}(b) = S(0) * (f_{biexp} * e^{-b*D_{fast}} + (1 - f_{biexp})e^{-b*D_{slow}}), \tag{3.4}$$

where the former model (S_{IVIM}, intravoxel incoherent motion model [Le1986]) has parameter $D_{perfusion}$ for measuring perfusion (also referred as pseudo diffusion D^* in the literature). The latter model (S_{biexp}) measures fast diffusion D_{fast} and slow diffusion D_{slow}. The f_{biexp} parameter is the fraction of the faster component of the biexponential (i. e. perfusion fraction f_{IVIM} for the IVIM model). Each model parameter expresses a different signal from the decay curve, which allows us to investigate various different characteristics from the DWI image. For parameter maps calculated from voxels of prostate DWI images, see Figure 3.1.

3.3 Fitting the Model to the Data

For a dataset consisting of N observed data pairs $(x_i, y_i), i = 1, ..., N$, a model describing the data can be given in the form of function $y = f(x, \lambda)$, where x is a sampling point in data (e. g. time in time series), and λ denotes the M model parameters $\lambda_1, ..., \lambda_M$. The setting of λ so that model fits the data as well as possible can be obtained by solving a constrained nonlinear optimization problem. The task here is to minimize the distances between the observed data samples and values from the model described by function f. A commonly used distance is the Mean Square Error (MSE) between the intensity values of the observed data y and corresponding data points of the model $f(x, \lambda)$:

$$MSE(x, y, \lambda) = \frac{1}{N} * \sum_{i=1}^{N} (y_i - f(x_i, \lambda))^2 \tag{3.5}$$

The MSE represents how much the model is expected to deviate from the original signal. Model fitting may also be performed with other objective

functions, such as different weighting schemes for samples [Mu2006], and considering non-normally distributed noise [Kr2012].

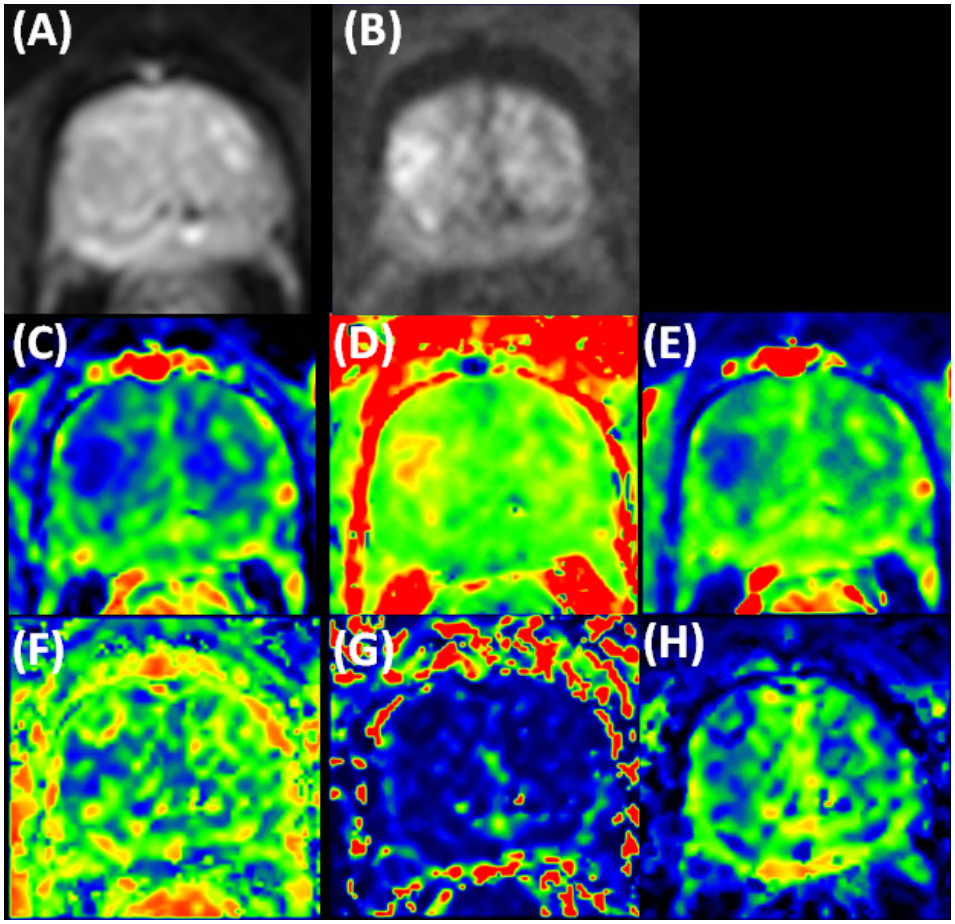

Figure 3.1: DWI image of prostate, and parameter maps of three DWI models. Original DWI signal samples are: (A) B_0-weighted image (b=0 ms/mm^2), and (B) B_{2000}-weighted image (b=2000 ms/mm^2). Sample images for parameter maps calculated with DWI models are kurtosis ADC (C) and K (D), monoexponential ADC (E) and biexponential f_{biexp} (F), D_{fast} (G) and D_{slow} (H). The images show a tumour on the left side of the central zone of the prostate (bright spot in B_{2000} image). The parameter maps allow us to make measurements in the tissue for tumour detection and characterization.

In optimization, λ is iteratively modified until the correspondence of f to the observed data is maximized. A common method for finding minimum of the fitting error is the Levenberg-Marquardt method [GiMuWr1981] which uses the gradient of f in respect to λ. In another approach, Nelder-Mead [NeMe1965] iterations are based on the evaluation points arranged as a simplex. If the objective function is quadratic, Newton's method [Ya2010] has potentially faster convergence. For regulating the length of steps in iterative optimization, the Trust Region Strategy for minimization procedure may be used [ByScSc1987]. Variations exist for all of these approaches. Their suitability for the given optimization task depends on the convergence between iterations and computational cost of evaluating the value of the objective function.

A limitation of these methods is that they often find only local minima of the objective function. This can be addressed with global optimization methods [FlGo2009] that try to maximise the chances that the global minimum is found. Another more simplistic technique is to start the optimization at multiple starting locations, and then choose the solution that has the smallest Sum of Squared Error (SSE). With low dimensionality of the parameter space (M) one can arrange the starting locations of the search in a grid form. With the assumption that the objective function's 'landscape' is not too mountainous between the grid points, the density of the grid limits the maximum amount of error that can occur for fitting [Si2006, Pi2013].

Finding a global minimum for the $SSE(x, y, f, \lambda)$ (see Eq. 3.9 below) does not mean that the parameters λ give reliable measurement that is relevant to the clinical question being evaluated. The parameter values at global minima of the $SSE(x, y, f, \lambda)$ may be biased or imprecise due to inaccuracies in the observed data y that the fitted model f does not address. This occurs when the model is overfitted to data that contains physiological and measurement noise.

Instead of minimizing the distance between the function and the observed data, one can search for parameter values that are most likely to have produced the observed data. This method is called Maximum Likelihood Estimation (MLE). In MLE, λ is optimised so that the likelihood function

$$\mathcal{L}(\lambda|y_1...y_N) = f(y_1...y_N|\lambda) \tag{3.6}$$

has its maximum value [Pr2009]. The likelihood $\mathcal{L}$ is used for inference about λ. The f is a function of the observed y values for a given parameter setting λ. Assuming that all observed values $y_1...y_N$ have the same probability distribution and that they are mutually independent, the Eq. 3.6 can be simplified to a product of samples:

$$\mathcal{L}(\lambda|y_1...y_N) = \prod_{i=1}^{N} P(y_i|\lambda) \tag{3.7}$$

where $P(y_i|\lambda)$ is the conditional probability of y_i-values on parameter setting λ. Logarithm of Eq. 3.7 is used for facilitating the computations:

$$\ln(\mathcal{L}(\lambda|y_1...y_N)) = \sum_{i=1}^{N} \ln(P(y_i|\lambda)) \tag{3.8}$$

Because logarithm is a monotonically increasing function, maximising Eq. 3.8 also maximises Eq. 3.7. The task of finding MLE can be further converted to the minimisation of $-\ln(\mathcal{L}(\lambda|x))$.

3.4 Model selection by Goodness of Fit

For a model in molecular imaging to be useful for research and diagnostics, it should be robust enough to separate unwanted variation (i. e. noise) from the signal, and sensitive enough for its parameters to carry relevant information about the characteristics of the target tissue. The quality of the model parameters can be evaluated using computer simulations and real data. Numerical measures are utilised in these tests. In addition to these two, it is desirable that the model fitted to the data properly explains the data, i. e. the observed signal can be understood to originate from the process described by the model. For this, the data points given by the model should be close to the observed data points, while still avoiding overfitted models. Common statistics in the related literature measuring the Goodness of Fit (GoF), are MSE, SSE and Root Mean Squared Error ($RMSE$):

$$\begin{aligned} &SSE(x, y, f, \lambda) = \textstyle\sum_{i=1}^{N}(y_i - f(x_i, \lambda))^2 = N * MSE \\ &RMSE = \sqrt{MSE} \end{aligned} \tag{3.9}$$

The $RMSE$ (Root Mean Squared Error) is derived from MSE, representing standard deviation of residuals. Another common statistics is R^2 which stands for the ratio of the Sum of Squares Residuals (SSR) of the model and the Total Sum of Squares (TSS) of the data:

$$\begin{aligned} &R^2 = \tfrac{SSR}{TSS} \\ &SSR = \textstyle\sum_{i=1}^{N}(f(x_i, \lambda) - \overline{y})^2 \\ &TSS = \textstyle\sum_{i=1}^{N}(y_i - \overline{y})^2 \end{aligned} \tag{3.10}$$

where $\overline{y}$ is the average of the observed data. The R^2 expresses how large a proportion of the variance in the observed data (e. g. 0.7 means 70%) is explained by the model. The underlying assumption for R^2 is that the fitted model is linear because for nonlinear data, the value of $SSR + SSE$ (Eq. 3.9, i. e. unexplained variance) is not TSS [SpNe2010]. In medical image data, the fitted models are often nonlinear. Also, the distribution of errors SSR may differ from normal. For model selection purposes, an adjusted version (adjusted R^2) can be used to penalize overly complex models. In the univariate linear least squares regression, R^2 is equal to the square of the Pearson correlation coefficient r.

A model containing as many parameters as there are observed data points can be expected to always produce a perfect fit, but a model of this kind generalizes very poorly. It is therefore important to penalize models that have numerous parameters. Parameter values may contain mostly noise and not the true signal that could be used for making a correct diagnosis. A commonly used measure in model comparison is the Akaike Information Criteria (AIC) [BuAn1998]:

$$AIC = -2 * \ln(\mathcal{L}(\hat{\lambda}|y)) + 2 * K, \tag{3.11}$$

where $\mathcal{L}(\hat{\lambda}|y)$ is the likelihood Eq. 3.6 with estimator $\hat{\lambda}$ of parameter setting λ of the model, and K is the number of model parameters. In the case of least squares estimation with independent, identically distributed (i.i.d.) errors between the model and observed data, the AIC can be expressed with SSE as:

$$AIC = N * \ln(\frac{SSE}{N}) + 2 * K, \tag{3.12}$$

where N is the number of samples. Assuming that the residuals are Gaussian distributed, the SSE/N can be considered to be the MLE of the model fit to the data. The AIC can be used for comparison of both nested and non-nested models [Gl2007]. Two models are nested if the more complex model can be created from the simpler one by adding new parameters without removing existing ones. Another very similar approach, *Bayesian Information Criteria* (BIC) [BuAn2004], differs from AIC only in how much it penalizes the model complexity.

For a small number of samples in relation to the number of parameters ($\frac{N}{K} < 40$), the AIC values are biased to favour models that contain more parameters [BuAn1998]. This is the case e. g. in DWI prostate datasets where the number of sample points is small. In such cases, a variant of AIC with a correction term has been proposed [BuAn2004]:

$$AICc = N * \ln(\frac{SSE}{N}) + 2 * K + \frac{2 * K * (K + 1)}{N - K - 1} \tag{3.13}$$

The $AICc$ was originally proposed for linear regression with normally distributed errors [Su1978]. When used with nonlinear regression models (such as exponential DWI models), the unbiasedness of $AICc$ is only approximate [HuTs1989].

The AIC and $AICc$ are measures on a relative scale, i. e. their values are usable only within a given observation dataset where they are calculated and are not transferrable to other datasets. Therefore in practise, for a group of models with a given observation dataset under comparison, the differences ΔAIC and $\Delta AICc$ values need to be calculated in comparison to the model having the smallest AIC, i. e. the model that has the best fit to the data in SSE sense. This means that for two models A and B, where A is simpler (containing fewer parameters) than B, the difference of $AICc$ is defined as:

$$\begin{aligned} &\Delta AICc = N * (\ln(\tfrac{SSE_B}{N}) - \ln(\tfrac{SSE_A}{N})) + 2 * (K_B - K_A) + \\ &2 * (\tfrac{K_B*(K_B+1)}{N-K_B-1} - \tfrac{K_A*(K_A+1)}{N-K_A-1}) \end{aligned} \tag{3.14}$$

Testing of the statistical significance between the models A and B in terms of their fits to the data can be done with the F-ratio :

$$\text{F-ratio} = \frac{(SSE_A - SSE_B)/SSE_B}{(DF_A - DF_B)/DF_B} \tag{3.15}$$

where SSE_A and SSE_B are the unexplained variances (3.9) of the simpler and more complex models, respectively. The Degrees of Freedom DF is the number of independent pieces of information that are used to calculate SSE, and it is smaller for the more complex model (B) that involves more parameters. In PET and DWI signals, DF is calculated as the number of adjusted parameters minus one.

With the F-ratio, the null hypothesis is that the fit with the more complex model is not better than that of the simpler model. If the null hypothesis is not rejected, the simpler model should be preferred, following the *parsimonian principle*. Rejecting of the null hypothesis would indicate that the data contain information that would be lost to the residuals if a simpler model were used. The F-ratio compares the simpler and more complex model that are nested within each other. It cannot be used to test e. g. two models with an equal number of parameters, or models that are not nested. Then, AIC may be used.

Chapter 4

Motivation

In order to use molecular imaging in an efficient way in scientific and clinical studies, various processing steps are required which in turn needs various image analysis techniques. Some of them are addressed here for different applications.

4.1 Partial Volume Effect Correction Used for Improving Quantification of PET

Partial Volume Effect (PVE) due to resolution loss hampers the quantification of PET signal and requires correction. The PVE displaces the true uptake that is acquired, mixing intensity values of neighbouring regions, and reducing intensity in small regions. In addition to PVE due to resolution, PVEs is also caused by cardiac and respiratory motion of the patient, which can cause additional challenges in organs that are affected by them. In addressing the PVE, Partial Volume Effect Correction (PVC) in its various forms has been proved important in the analysis of real patient data. There are three major applications where PVC has been used. In brain studies, there is loss of signal intensity due to the thin cortex. In tumour imaging, loss of intensity affects the SUV (Standardized Uptake Value). In heart, PVE affects distortion in the activity of myocardium or the coronaries.

When evaluating a PVC technique with [^{11}C]carfentanil receptor binding study with temporal lobe epilepsy [Mü1992], regional increase of intensity values was observed after PVC. In brain atrophy, the cortex is thin and thus PVE reduces intensity, making it difficult to know if its true intensity has reduced. In [Sa2007], there was reduced FDG uptake in Alzheimer's disease (AD) patients having atrophy. After PVC, it was concluded that the decrease in the signal activity was not due to the PVE, which helped studying early AD. The PVE smoothens PET images so that differences between subjects are not so clearly recognized. Further, in [Th2011] increase in

intersubject variability was reported with PVC in [18F]flutemetamol PET study of the AD, and also an improvement was observed in quantitative accuracy with a phantom study. Moreover, a PVC method [Al2004] increased intersubject variability, indicating its usefulness in group comparison studies. More recently, the importance of PVE correction for more reliable and accurate quantification of PET has been highlighted in [Bo2014].

When PET is used in the planning of radiotherapy treatments, it is important to correct activities for PVE because the effect affects the apparent tumour size and the measures characterizing uptake, e. g. SUV. The effect of PVE in PET tumour imaging has been discussed in [So2007]. In [Ho2010], PVC was demonstrated to improve the accuracy of tumour SUV estimation without decreasing the test-retest variability. In [Ty2010], the SUV values calculated after PVC had improved accuracy and reproducibility. Further, the mean uptake value of tumour region was improved in ^{18}F-FDG and ^{11}C-CO data [Te2007]. The importance of PVE correction in the diagnosis of tumour has been further noted in [Sh2006, Al2008, Pe2014].

The need for using PVC also in PET heart images has been presented in the literature. In myocardial perfusion imaging, the PVE affects a normally perfused heart wall [Pr2009b]. Also spillover from neighbouring organs is to be avoided [Re2016], which highlights the need for PVC. There are many PV correction methods but practiocioners are faced with the dilemma as to which approach is best. There is little published on cross-comparison of methods and therefore this ex explored in this thesis.

4.2 Infant Brain Image Segmentation Enabling Further Analysis

The brain MRI segmentation generally means labeling of the voxels into three tissue classes of Gray Matter (GM), White Matter (WM), and Cerebrospinal Fluid (CSF). The segmentation is usually done with T1 and T2 weighted MRI, that have good contrast between tissue classes. As an important step in the MRI brain data analysis procedures, segmentation of the brain tissue of small children helps in the study of brain development and related environmental factors. While there is a clear need for segmentation of neonatal brain images, there are some additional challenges in comparison to adult brain segmentation, which need to be addressed.

The neonatal brain goes through rapid changes including myelination. In myelination process, myelin forms around axons in brain. Myelination and other changes are visible in the changes of MRI signal intensity [Ha1991] and the brain volume [Hü1998], and therefore the segmentation of brain images of small children (i. e. less than approximately 2 years) differs from segmentation of adult brain images. More specificly, the intensity distribu-

tions of the brain regions are overlapping [Pr2005], and they change over time. In addition to the changes in the MR signal intensities, there are also changes in relative volumes of brain tissues and increase in the folding of the cortex. The smaller size of the brain requires smaller resolution, increasing noise levels in the image data. The infants cannot be sedated or constrained for ethical reasons, and therefore the scanning times need to be short, which further decreases the image quality. Even with short scan times, a infant may not stay still during the sequence, resulting in motion. Despite these challenges, there has been increase in neonatal brain MRI examinations, which requires new tools that address these problems.

4.3 Diffusion Weighted MRI Modelling for Cancer Diagnosis

Prostate cancer (PCa) continues to be a major health problem for men. For definitive diagnosis of the PCa risk, the two commonly applied methods are Prostate Specific Antigen (PSA) and Digital Rectal Examination (DRE). The systematic transrectal ultrasound (TRUS) guided prostate biopsy remains the most common way of the actual PCa diagnosis. While TRUS-guided biopsy is widely used, it is an unnecessary procedure when clinically insignificant cancer are detected [Ha2007, Ca2011b]. In addition, about 25-35% of cancers are missed on the first systematic TRUS guided biopsy [Dj2001]. When the biopsy is repeated with patients having continuously elevated or increasing PSA and previous negative TRUS-guided biopsy, it can lead into the increase of complications [La2009].

Diffusion Weighted Imaging (DWI), offers promising possibilities for the study of PCa [Ve2011]. DWI is noninvasive, easy to implement and has relatively short acquisition times. The process of DWI imaging involves typically few minutes scan during which the patient should be still in the MRI scanner. The DWI signal usually consists of at least two samples. When an exponential function is fitted across the samples, the resulting slope of the curve can be interpreted as attenuation of the water molecules. This allows qualitative and quantitative measurements of the signal.

Development of algorithms and optimisation of the imaging sequence for quantification of PCa with DWI of MRI can potentially have an effect on its treatment. The proper placement of the b-values may eliminate the need for Dynamic Constrast-Enhanced MRI (DCE-MRI) [Pa2013]. This would be an important advancement, because intravenous contrast media cannot be administered to patients that have severe allergies for the injected contrast agent. For the above reasons it is hypotized that accurate characterisation of findings could have a major effect on the management of the disease [La2010, Tu2011]. In addition to prostate cancer, the same DWI models have been

used in study conditions in brain [Pr1999], kidney and liver, which suggests that the results in prostate cancer may be applied to study of other diseases as well.

Chapter 5

Literature Review

5.1 PVE Correction in PET

Various approaches and modifications to previously presented methods have been proposed, see [Er2012] for a general review and [So2007] for discussion on the application of PVC in PET tumour imaging. In the correction procedure, supplementary information about the target object anatomy (e. g. from CT or MRI) may be used to improve the correction effect. The majority of the PVC methods have been developed by using PET brain data. For other source data, [Pr2009b] presented a method for cardiac SPECT imaging. Instead of image processing, PVC can also be included in PET kinetic modelling [Ii1991].

For validation of a PVC technique, there is commonly no golden standard. Therefore, phantom experiments (i. e. scanning containers modelling PVE effects) are often involved in these studies to show the performance of PVC, while the technique will finally be used for real *in vivo* data. In what follows, a short overview is given for techniques to apply PVC in PET and for the main factors affecting its performance. Details of most common approaches are left to be described later in Chapter 6.

From parameters affecting the performance of PVC, Point Spread Function (PSF) is known to vary across the scanner Field of View (FOV) [Ho1982, Ba2010]. In practise, however, this is considered to only contribute a small error to the results. Lately, an iterative EM technique involving spatially variant PSF has been implemented [Ba2010]. In comparison to uniformly distributed PSF, similar results were observed in [Ba2010] when a spatially variant PSF was used. However, an arbitrary selection of the parameters in PVC with spatially invariant PSF resulted in large differences. In [Al2010], more edge artefacts were observed with invariant PSF when PVC was included in the image reconstruction process.

Another, even more important factor affecting the performance of a PVC

technique is the way of utilizing the supplementary information on the edges in the images (i. e. delineation of anatomical regions). While the supplementary information is potentially beneficial, these methods may be affected by misregistration and segmentation errors. It has been observed that these errors hamper the performance of the PVC. The topic has been studied earlier in [Me1999], and later in [Qu2004, Za2006b]. The sensitivity of PVC to segmentation and coregistration errors has led the research interest to methods that are based on PET signals, only.

Correction for PVE was first applied in [Go1986] to CT, requiring knowledge of two contributing substance intensities, and their proportion. In PET, the development of PVC started with methods based on anatomy from MRI in 90's when spill out from GM+WM region of brain was applied in [^{11}C]carfentanil μ opiate receptor PET studies of AD patients [Me1990]. In [Mü1992], the correction involved GM for spill-out and WM for spill-in. Instead of producing a PVE corrected image, an approach using a *geometric transfer matrix* (GTM) was developed in [Ro1998]. The GTM estimates are accurate and suitable in situations where the mean intensity values inside ROIs are sufficient for further analysis. The technique of [Mü1992] depends on the estimate of the mean WM intensity when correcting the GM intensity. That estimation was further developed in [Al2004].

A multiresolution approach with undecimated wavelet transform was used in [Bo2006], allowing PVC without delineation of homogenous regions. A model which relates the wavelet coefficients of low (PET, SPECT) and high (CT, MRI) resolution images was used to recover lacking details in the image. The same technique was later enhanced by involving additional information from co-registered CT data [Bo2008]. Wavelet transform was used also in [Sh2009], where the wavelet coefficients of the details were recovered by using anatomical information from a segmented anatomical atlas that was co-registered to PET. The *dual-tree complex wavelet transform* (CWT) was used, and anatomical information was from T1 MRI in [Sh2009].

Another approach for performing PVE correction is to apply the deconvolution operation for which various methods have been proposed [Pa2007]. A well-known method for iterative deconvolution is the Van Cittert algorithm [Va1931]. Another common image intensity based approach is the Richardson-Lucy algorithm [Ri1972, Lu1974]. Comparing the two approaches, the Richardson-Lucy method is a Bayesian-based approach, which models the image and the PSF values by probability distributions [Lu1974]. In case of additive Poisson noise, Van Cittert method converges to the maximum likelihood estimate of the image [Sh1982]. The approach in [Va1931] searches for the solution by successive increments. It has similarities to other iterative methods of Landweber and steepest descent (see e. g. [Be1998, De2014]). It differs from them in the construction of the iteration step that is added to the current estimate. In both algorithms the iterations are con-

tinued until a convergence criterion is reached, e. g. the maximum number of iterations have been performed or the rate of change in the results becomes lower than a predetermined limit [GuLi2012]. A limitation for these algorithms as presented in [Va1931] and [Lu1974] is that in the presence of noise they generally do not find a realistic solution or they diverge as the noise propagates. Limiting the number of iterations may be used to regularize the solution.

For addressing the noise amplification in the iterations, constraints may be applied. One such method is the Jansson Van Cittert algorithm [Ja1970] where the updates are constrained between iterations. Other regularization methods (see e. g. [Pa2007]) can be applied to the iterative and Bayesian-based approaches. In PET, these include the Total Variation approach [ToRe2008] and wavelet-based noise removal [Bo2009]. Other voxel-wise PVE correction techniques include 3D wavelet decomposition [Bo2007], Hidden Markov Random Tree modelling for combining CT or MR with PET [Po2011], and recently, using GTM (Eq. 6.12) for delineation of homogenous structures from PET in an iterative manner [Xu2015].

PVC with deconvolution was used in [Te2007], where Volumes of Interest (VOIs) were used in Van Cittert's iterative procedure to estimate the PVE corrected maximum and mean intensity values. Similarly to other PVC approaches, the deconvolution procedure suffers from noise amplification of the input signal. In [Ki2008], the deconvolution technique was used with regularization for addressing noise amplification between iterations. In [ToRe2008], a reblurred variant of the Van Cittert iterative deconvolution technique was presented. This variant applies total variation-based regularization for noise. Another type of deconvolution algorithm (Richardson-Lucy) in combination with partial segmentation of homogenous regions was used in [Se2010]. The technique suits for situations where accurate segmentation is challenging, such as in the case of pathological abnormalities. A hybrid GTM and deconvolution based method was presented in [Th2011], where anatomical information was from MRI. As another method using MRI with PET, [Wa2012] used Maximum A Posteriori (MAP) approach, with edge preserving smoothness constraint from co-registered MRI.

In [Bo2014], more simple PVC methods were compared with some of the newer methods (e. g. [Al2004, Sh2009]), noting that the newly proposed techniques do not necessarily improve reliability. More recently, Local Regression Analysis (LoReAn)[Co2013] was applied; segmentation of anatomical regions from MRI was used with PSF in a linear PVE model for each voxel.

In addition to applying PVC as a post-processing step, it can also be included in the actual PET image reconstruction. In [Hu2007], the reconstruction algorithm (blob-based LOR-RAMLA) involved resolution preservation with noise suppression. PVC in the ordered subsets expectation max-

imization method was shown to have superior performance in comparison to more conventional reconstruction techniques in [Re2003], when the method was implemented in GE Advance PET scanner (GE HealthCare, Millwake, USA). This approach considers physical properties of the data acquisition process in *system matrix*, which describes the relationship between data and its sources (see [Ir2016] for review). The system matrix is used in an iterative reconstruction process to perform PET image reconstruction with PVC. The PVE correction with this approach has also been applied to correcting the respiratory motion [Pe2014] by using supplementary information from MRI. In [Al2006], the system matrix was created with Monte Carlo simulations and applied to reconstruction of simulated and measured data. The system matrix can be created with empirical measurements [Pa2006], with Monte Carlo simulations [Va2006], or analytically [OlGo1996, Lo2014]. The system matrix contains characteristics which vary between scanner producers (and between models within a vendor). Therefore, the system matrix must be created separately for each scanner model. The system matrix with PSF modelling was created for Siemens Biograph (Hi-Rez) scanner in [Pa2006] from empirical measurements. Also with empirical measurements in [Al2010], a spatially variant system matrix was created for GE Discovery STE (GE DSTE). In [Cl2010] the system matrix was created for a Philips Gemini 16 Power scanner, with a model of spatially variant, non-Gaussian PSF.

5.2 Infant Brain MR Segmentation

Neonatal brain MRI segmentation has additional challenges in comparison to adult brain segmentation, and most of the methods have been developed quite recently for it. The majority of the more recently developed techniques rely on anatomical *a priori* information, while some of the data-driven methods allow the cortex shape to deviate more from the normal brain. Currently, the segmentation of neonatal brain is considered to be in its early stages [De2015] of development. In particular, there are difficulties in segmentation of the myelinated white matter, and abnormalities in the brain are not considered, with only few exceptions.

In [To1995], the regions of GM and WM were segmented with semi-automatic discriminant analysis from Proton Density weighted and T2 weighted MR images. In [Hü1998] semiautomatic segmentation was performed with k-nearest-neighbour (k-NN) classification of the voxels into GM, WM, CSF, myelinated WM and subcortical GM. Another semi-automatic segmentation method using k-NN was presented in [Wa2000]. The segmentation proce-

dure classifies the features of the image, by using localization information from a template. In addition to segmentation of normal brain images, the method was also applied to brain including anomalies.

A maximum likelihood approach was used in [Co2000] to segment GM, WM and CSF of small children (of the age 26 months) MR images. The first fully automatic method for neonates was tested on 4 cases in [Pr2005]. Probabilistic *a priori* brain atlas was aligned to the image with affine co-registration by the means of Maximum Likelihood Estimation (MLE) with *Expectation Maximization* (EM). The method was specific for neonatals and involved the separation of the myelinated and non-myelinated brain segments. The MLE approach with *a priori* information was used again in [We2006]. The k-NN classifier was combined with a spatial homogeneity constraint from Markov Random Field (MRF) model. The related atlas was built from 20 cases. The EM-MRF scheme was applied in [Xu2007], where cortical surface reconstruction was created. The MRF was used for removing mislabeled voxels in the EM algorithm. Triangularized mesh reconstruction of the cortex region allowed calculation of the volume, surface area, curvature and thickness for the cortex. In [Sh2009b], imaging of neonatals involved specific head coil equipment in the MRI data acquisition. An atlas was created with rigid co-registration to standard adult atlas, followed by iterations of non-rigid co-registrations with the HAMMER tool [Sh2002]. Multiple atlases were used later together with a k-NN classifier in [Sr2012]. The initial segmentation with atlases provided spatial priors, which were then refined. The performance of atlas-based segmentation depends on the quality of the atlas and on the co-registration of the atlas to the image to be segmented [Sh2010]. Low CNR (Contrast to Noise Ratio) in neonatal images, variation in brain shape and size makes the use of an atlas challenging.

In [So2007b] the Maximum A Posteriori (MAP) segmentation was applied. The *a priori* information was acquired with fuzzy nonlinear Support Vector Machine (SVM), which was used in learning features from 9 images. In comparison to atlas-base spatial prior, the intensity-based prior with SVM was found to be more effective. Another approach without predefined brain atlases was presented in [Gu2011]. Instead of *a priori* information, morphological constraints were derived from anatomical knowledge.

5.3 DWI Modelling

The mathematical framework for stating the relation of experimental variables of the pulsed field gradient in MRI experimental variables was established in [StTa1965], and later, the principle of DWI was introduced in 1980's [Le1986, Le1988]. Since then, DWI has gained popularity because of its ability to estimate tumour cellularity with quantitative diffusion images.

For the quantification, the DWI signal must be modelled. However, the true biophysical meaning of the DWI signal is yet to be established, which makes challenges to the modelling and has resulted in various advanced techniques to interpret the signal. In the cancer studies, the modelling of the DWI signal focuses on models that describe the isotropic diffusion in the tissue. This is in contrast to the Diffusion Tensor Imaging (DTI) technique that measures the anisotropic diffusion. The DTI is mostly used to study features in the brain tissue with fibers in the White Matter (WM).

In the following, we give a short review of the modelling of the DWI signal focusing on prostate cancer studies, while the references to the literature of brain studies are used to reveal additional properties of DWI related models. The most commonly used DWI models are explained in more detail later in Chapter 3.2.

The DWI technique was initially presented with the Intra-voxel Incoherent Motion (IVIM) model [Le1986] Eq. 3.4. This model involves two components of perfusion (or pseudo-diffusion) $D_{perfusion}$, and fast diffusion D_{fast}. The IVIM model was further studied with Monte Carlo simulations in [Pe1992]. It was observed that a small proportion of perfusion fraction f_{IVIM} in IVIM contributes to the difficulty in measuring perfusion in the presence of noise, making $D_{perfusion}$ even harder to estimate from the signal than f_{IVIM}, independent of the applied fitting procedure. For the monoexponential model Eq. 3.1, the slope $ADCm$ of the monoexponential curve was used [Pr1999] to address the effect of T2-relaxation to individual b-values in the analysis of cerebral infarct. As distinct from physiological models, in [Be2004], a statistical fitting function called the stretched exponential model (Eq. 3.3) was evaluated, in a preclinical study of rat brain. Specifically, the α parameter of the model was shown to differ significantly between tumour and normal regions in the Gray Matter (GM). A model Eq. 3.2 that measures the deviation of the signal from Gaussian diffusion $ADCm$ was presented in [Je2005]. The kurtosity parameter K was used as a measure of the tissue structure.

5.3.1 Evaluation of the Models

In order to resolve the most suitable modelling technique, the above presented methods have been compared in various application fields. Starting from evaluations of how well a DWI model explains the observed DWI decay curve, monoexponential and biexponential models were evaluated in [Mu2006b]. The biexponential model is mathematically similar to IVIM, but it has bigger highest b-value in the DWI signal. It thus measures only the fast diffusion D_{fast} and the slow diffusion D_{slow}, without perfusion component $D_{perfusion}$. It was concluded in [Mu2006b] that the biexponential model characterizes the DWI curve in prostate better than the conventional

monoexponential model on the basis of F-test between residuals after fitting operations.

In [Ki2007], the biexponential model was compared againts the cumulant expansion model which has been derived from the formulation of DWI signal as power series. The cumulant expansion model was observed to describe the brain data equally well as the biexponential model, while it had less parameters. This in turn suggests that some parameters of the biexponential model may not be necessary in DWI modelling, at least in brain tissue.

In liver, the monoexponential and IVIM models were evaluated in [Lu2008]. While this pilot study was lacking comparisons on goodness-of-fits or performance measures, the DWI curve was considered to follow the biexponential pattern better in comparison to monoexponential curve.

Using multiple b-values, [Le2009b] showed that the f_{IVIM} parameter of the IVIM model was more suitable in the classification of healthy and non-healthy pancreatid tissues. In contrast, the IVIM model with prostate data was not found to have so good performance as the monoexponential model.

The IVIM model was compared to the monoexponential model in [Ri2009] with prostate data. They found that the IVIM model described the data better than the monoexponential model in b-value range from 0 to 800s/mm^2. However, it was noted that there was large variation in the parameter estimates of IVIM, which limits the utility of this model for prostate tumour diagnosis.

In continuation of DWI studies to prostate, it was observed that in [Sh2009c] the biexponential model provided better fit than monoexpoential according to F-test for cancer data.

The AIC performance measure (Eq. 3.12) considers also the number of model parameters. This measure was used in kidney data in [Wi2010], including also noise simulations. The monoexponential, stretched, kurtosis and biexponential functions were compared using AIC and F-ratio. While the biexponential model had the best fit when considering these statistical measures, the monoexponential model was the most robust againts noise.

For direct evidence from visual observations on the target tissue, the $ADCm$ parameter was evaluated together with pathology measures of prostate in [La2010]. It was observed that the value of ADC correlates with various structural features of the tissue.

Noise robustness of the IVIM model was considered in [Dö2011]. Similarly to the comparison with the biexponential model in [Wi2010], in [Dö2011] the IVIM described the DWI curve better, and monoexponential was more robust against noise in the low b-value range of 0-800s/mm^2. It was further observed in [Dü2011] that the value of $ADCm$ depends strongly on the range of the b-values in DWI, because the signal in prostate is clearly nonmonoexponential at higher b-values.

The study in [Tu2011] addressed the capability of $ADCm$ in the pre-

diction of the aggressiveness of the PCa. The $ADCm$ parameter correlated negatively with the Gleason score gradings, which suggests that the $ADCm$ can be useful in the prediction of aggressiveness. This observation was confirmed in [Ha2011], where the $ADCm$ had high classification performance between different grades of tumours located in the periferal zone of the prostate.

For characterizing the progression of the prostate cancer, different b-value fractions of 0-300s/mm^2, 300-800s/mm^2 and 0-800s/mm^2 were compared in [Gi2011]. The part of b-value range corresponding to the slow component of IVIM (0-800s/mm^2) was found to be a significant predictor for cancer progression (Cox's regression for hazard rate).

Physical validity of the IVIM model was tested with mouse in [Ki2012b]. The *interstitial fluid pressure* (IFP) correlated with $D_{perfusion}$, while for the monoexponential model this was not observed. The observation is notable for the use of the IVIM model. The IFP is an important variable in cancer treatment because it impedes the delivery of therapeutic drugs to the core of the tumours. Another mice study for IVIM was done in [Le2014]. The estimated model parameters were compared to histological property of microvessel density (MVD). Interestingly, the $D_{perfusion}$ and f_{IVIM} parameters had significant correlation (Spearman's ρ) with MVD, while D_{fast} did not. This suggests potential usefulness of the $D_{perfusion}$ and f_{IVIM} parameters in the future if noise can be solved for those parameters in *in vivo* human data.

An additional parameter f_{IVIM} for the monoexponential model was proposed in [Ma2012]. They suggested that D_{fast} in IVIM is more accurate with AUC measures than $ADCm$ in the classification of malignant from benign tissue in prostate.

5.3.2 Recent DWI Models

Lately, also the other DWI models have attained attention. The kurtosis model was evaluted in [Ro2012] for characterizing the prostate tumour aggressiveness. The K parameter of the model performed better than $ADCm$ when the classification performance was measured with the AUC values of the low and high grade cancers.

The stretched exponential function was compared in [Ma2012b] to IVIM model using Monte Carlo simulations and real DWI prostate images. Like the kurtosis model, the stretched function is less complex than IVIM. This may explain the better reproducibility of the stretched function in comparison to IVIM in terms of $ICC(3,1)$. When noise was increased in the simulations, also its precision and bias were superior to IVIM.

All four models, monoexponential, stretched, kurtosis and biexponential were compared in [Qu2012], with a set of 11 b-values ranging from 0 to

800s/mm^2 for fittings in ROIs delineated inside prostate tumours. The more complex models were shown to fit better to the signal curve than the simple monoexponential model. This was reported earlier [Mu2006b] for the monoexponential and biexponential models. However, the performance of the models for clinical context was not evaluated.

For liver, [An2013] evaluated the IVIM using the Bland-Altman analysis. The reproducibility was acceptable in D_{fast}, but f_{IVIM} and $D_{perfusion}$ had poor repeatability.

A very high range of b-values (up to 8252 s/mm^2) was used in [Bo2014b]. The study considered the goodness of fit and difference between normal and cancerous tissue, and compared the four models (of monoexponential, stretched exponential, kurtosis and biexponential) in prostate. The biexponential and kurtosis models had better fits than the stretched and monoexponential models when evaluated with AIC. The fit of the biexponential model was improved when largest b-value was set up to 8252 s/mm^2 in comparison to a lower b-value range. This suggests the use of high b-values, although the study did not make any attempt to address the repeatability of the parameter values or the actual correlation to pathology.

A study reporting limitations in robustness against noise of the IVIM model was in [Wu2015]. Overall, the biexponential and IVIM models have demonstrated to be more sensitive to the noise than the less complex models, which limits their usability for cancer studies. However, it can be expected that their performance improves with higher SNR in the DWI data (e. g. with advanced scanner technology).

A recently developed model (VERDICT) was proposed for DWI of prostate in [Pa2015]. The model considers restricted, hindered and restricted isotropic diffusions simultaneously. The model successfully differentiated between benign and cancer regions.

Recently, also another model for DWI signal modelling in prostate data was suggested in [Sh2015]. This so-called 'Gamma Distribution' model takes statistical measures from the distribution of diffusion decay coefficients of the DWI curve. Measures in area under the Gamma distribution curve of the diffusion coefficients were found to differ between cancer, benign and healthy tissue.

5.3.3 The Number of b-values

The samples of the DWI signal affect the performance of all of the models, and if a model provides parameter estimates of good quality, the number of b-values can be reduced in order to lessen the time spent in the MRI scanner. This has led to various studies aiming to optimise the b-value settings in such a way that the best trade-off between the performance and scanning time is achieved. Optimal b-value setting was determined by calculation

for $ADCm$ in [Sa2011]. The method needed an estimate of SNR and was applied to the DWI image acquisition scheme with two b-values for high resolution DWI data of the spinal cord. Curiously, this study addressed also the noise statistics in the DWI signal after taking logarithm, which is often omitted when DWI modelling is applied to transformed signal.

For the IVIM model, the b-value positioning was optimised in [Le2011]. In this study, Monte Carlo simulations were used to evaluate different combinations of the b-values. The authors suggested the use of 10 b-values for clinical setting, and noted that the parameter estimation depends strongly on the SNR level.

The selection of the b-value setting was studied for the biexponential model also in [Zh2012b] with Monte Carlo simulations and with real DWI acquisitions in kidney data. The estimation error reduced in comparison to conventional uniform distribution of the b-values, which highlights the importance of optimization for the placement of b-values when using the biexponential model. In more recent development [Pa2013], different b-value combinations were evaluated for the IVIM model using prostate DWI data. The considered b-value settings were limited to include up to 4 b-values.

The placement of b-values has also been optimised for the kurtosis model. In [Ya2013], 3 b-values were suggested for each gradient direction in the context of brain DTI studies.

The distribution of b-values was also optimised in [Dy2014], for liver data. The authors concluded that 4 b-values can be used to estimate the IVIM parameters in the liver tissue. The reproducibility of D_{slow} parameter did not substantially degrade when only 4 b-values were used instead of 16. However, the reproducibility was less for the other parameters of f_{biexp} and D_{fast} in the IVIM model.

The IVIM was further evaluated in [Co2015] with Monte Carlo simulations and liver data. They showed that excluding low b-values (0 < b-value < 50 s/mm^2) can lead to underestimation of $D_{perfusion}$ in liver studies.

5.3.4 Other DWI Analysis Techniques

It is evident that the individual DWI curve has low SNR with commonly used MR systems (i. e. for systems with 3T or below), making it challenging to obtain useful parameter estimates for otherwise promising biexponential and IVIM models. This invites development of other techniques for obtaining useful information from DWI image data. Instead of acquiring model parameters from a one-dimensional signal by fitting a model in the least squares sense, other techniques have also been proposed that either supplement or replace the traditional signal fitting procedure.

In [Mo2010], the prostate cancer diagnosis was carried out with a procedure involving segmentation, feature extraction and classification with MRF. In [Ca2012], the $ADCm$ was estimated in non-parametric manner, by using the Monte Carlo strategy to learn the underlying statistics of the DWI signal.

Monoexponential and two alternative approaches of biexponential fit were used in [He2013], for kidney DWI data. They used a parameter fitting without fixing any parameters, fixing D_{fast}, and fixing D_{slow}. The parameters that were not fixed were fitted in normal way. In the last approach, f_{biexp} was determined analytically. It was found that not only the model, but also the fitting procedure contributes to the parameter values. As an effect of image data processing, the performance of IVIM model parameter f_{IVIM} was found to increase when rigid co-registration was applied to pancreatic cancer images [Gr2013]. In [Pa2013], the IVIM model was fitted in similar manner as in [He2013] so that the parameters of D_{slow} and f_{IVIM} were estimated after taking logarithm of the DWI signal, while f_{IVIM} was extrapolated directly from the slope D_{slow}.

Still another variation of the IVIM fitting scheme was proposed in [Ma2013b], where the f_{IVIM} and $D_{perfusion}$ were fitted together by using fixed value of D_{fast}. The D_{fast} was obtained from fitting of the tail of the decay curve with monoexponential model. Multiple fitting steps were used also in [Ch2015], where the f_{IVIM} was extrapolated from the slope D_{slow} that was first fitted to the tail of the DWI curve. The approach had higher precision in voxelwise fitting in breast cancer than the conventional fitting method.

The $ADCm$ was used in [Ma2013] to extrapolate high b-value DWI images from low b-value data. Similar contrast-to-noise ratio was observed between normal and cancer tissue when extrapolated DWI images were compared to directly measured DWI images. However, this study presented no evaluation for clinical performance.

5.3.5 Noise in the DWI Signal

For a noisy DWI signal, it was shown in [Di2014] that Rician noise affects the parameter estimates when SNR is low. However, the authors failed to find any improvement after considering Rician type of noise when discriminating between benign and metastatic lymph nodes. Another study for Rician noise in the signal was done in [An2008] for DTI. The Rician noise was studied in diffusion-weighted MR image data when estimating the diffusion tensor. Addressing this type of noise in the fitting was noted to reduce bias in the results. However, the precision was weaker with the Rician noise model, and therefore it was speculated that the Gaussian estimates may be more reliable when the objective is to compare diffusion related parameters over time or across patient groups, which is the situation in cancer diagnostics.

Noise was considered also in [Or2014], where the parameters of the IVIM model were obtained with the Bayesian estimation approach. The distribution of the parameter values inside liver was assumed to be normal. Spatial neighbourhood of fitted voxels was considered in [Ku2014] for the IVIM model. The method reduced the parameter estimation errors for all IVIM parameters in Monte Carlo simulations and improved discrimination of patient groups of inflammatory bowel disease.

5.3.6 Some Other Developments in DWI Modelling

As other developments, an application tool to diagnosis was developed in [Vi2008]. As an example of other types of the MRI signal analysis, DCE-MRI (Dynamic Contrast-Enhanced MRI) heterogeneity index values are analysed from the parameter map of dynamics of the contrast agent. In[Ro2009], DCE-MRI was used with T2 weighted images to build a Computer Aided Diagnostic (CAD) scheme for prostate cancer, which was evaluated on the voxel-level.

Another specific approach for acquiring information from DWI the signal was presented in [Zh2015], where the IVIM model evaluation included an analysis of the parameter value histograms. The $D_{perfusion}$ and f_{IVIM} parameters were less useful in the classification of tumour aggressiveness, while D_{fast} parameter measuring slow diffusion was considered promising.

To sum up, the development of DWI modelling started with $ADCm$ of single exponential. While the more complex models of IVIM and the biexponential model provide closer fits to the data in least squares sense and are thus inviting, their performance has been weak in clinical settings. This suggest a clear need for improvements in either the scanning event or in the subsequent image analysis, or in the optimization of both of them.

Chapter 6

Algorithmic Analysis Techniques for Medical Images

The data acquisition processes of PET and MRI contain systematic and non-systematic observational errors, that must be accounted for. The former type of error affects the accuracy of the measurement, while the latter affects precision. If the systematic errors are known, they can be addressed with calibration for improved quantification. The precision may be improved with repeated measurements or techniques that improve the SNR of the acquisition process. In this chapter we explain the most essential error sources, and then provide techniques to quantify the quality of the measurements. Finally, we discuss some methods for reducing errors in order to improve the quality of the medical image data.

6.1 Numerical Measures

Image quality is often evaluated by visual inspection or by analyzing parameter values derived manually during image analysis. However, all methods containing manual interventions are vulnerable to subjectiveness from the operator, i. e. they contain intra- and inter-reader variance. Computed measures for image quality always produce the same output when assuming that the same input data and method was given. Measuring quality of medical images differs from that of ordinary photographs due to its intended purpose of helping to produce an accurate diagnosis, preferably based on measured physical characteristics rather than merely pleasing the eye, which is more subjective. In this chapter, we review common measures for the inaccuracy that reflects the quality of image data and its diagnostic accuracy in a mathematical manner. While the diagnosis of a disease is often performed by a

medical doctor by visual assessment of medical images, numerical quantitative values are also used when available as they bring more detailed information on the molecular level. Also, measures made by a human reader have repeatability of less than 1 (optimal repeatability), while computed measures always produce the same output, when assuming that the same input data and method was given.

Standard deviation is the most commonly used measure to depict dispersion of measurements $x = \{x_i | i = 1 \; to \; N\}$ around their mean $\overline{x}$:

$$SD(x) = \sqrt{\frac{\sum_i (x_i - \overline{x})^2}{n-1}} \tag{6.1}$$

When SD is expressed in proportion to the mean it is called the Relative Standard Deviation (RSD):

$$RSD(x) = \frac{SD(x)}{\overline{x}} \tag{6.2}$$

$$CV(x) = \frac{SD(x)}{\overline{x}} * 100\% \tag{6.3}$$

The Coefficient of Variation (CV) is a commonly used measure as it is unitless and allows comparisons between systems.

Another unitless measure is the *Intraclass Correlation Coefficient* (ICC). ICC can be used for evaluating the reliability of repeated measurements. There are six different forms of ICC, which are discussed in [ShFl1979]. $ICC(3,1)$ measures the expected reliability of a single measurement event, i. e. the consistency of measurements with a single scanning device without averaging over the repetitions:

$$ICC(3,1) = \frac{(MSB - MSE)}{(MSB + (k-1) * MSE)}, \tag{6.4}$$

where MSB is the mean squared difference between two groups of measurements, and MSE is the mean residual around the mean measurement of k repetitions of each case. The values of $ICC(3,1)$ vary in the range $[-1..1]$ where values are close to 1 when the measurements have high reliability for the purpose of differentiating between groups (e. g. measurements from normal tissue). Characterizing what is an acceptaple $ICC(3,1)$ value is a question that depends on the application and is therefore partially subjective. However, generally speaking, values below 0.4 have been considered unacceptable while values greater than 0.75 are excellent [Lo2015].

For individual subjects, variability between measurements can be measured by calculating *test-retest variability* (VAR) or *Coefficient of Repeatability* (CR) [Bl1999, Ko2009]:

$$VAR = 100\% * \frac{|scan_2 - scan_1|}{0.5 * |scan_2 + scan_1|}$$

$$RMSD = \sqrt{\sum_{i=1}^{N} \frac{d_i^2}{(N-1)}} \tag{6.5}$$

$$CR = 1.96 * RMSD,$$

where $scan_1$ and $scan_2$ are the parameter values of the first and second repetition and d_i stands for the difference between two repeated measurements of the same variable. VAR gives the relative difference of the repetitions in percentages, while $RMSD$ (Root Mean Squared Difference) and CR are expressed in absolute values.

Validation of an image processing technique can be based on statistics which are calculated from the available image data that has accompanied Golden standard (i. e. measures from the best reasonable analysis). Then, it becomes important to know how well the technique will generalize to newly introduced, independent data sets. This can be done with the cross-validation technique [Ar2010]. First, the available dataset is divided into *training* and *testing* datasets. Then, only the *training* dataset is used when creating the analysis procedure which is then evaluated (cross-validated) against the *testing* dataset. In order to address the variability from the selection of the datasets, the final results for the evaluation come from multiple cross-validation rounds using different partitions of the original data. This allows to build models and techniques which are partially or completely based on statistically expected performance. The cross-validation technique can be used when knowledge-based (e. g. knowledge about physiological phenomena) modelling is hard to build in such a way that it provides high enough performance.

In order to obtain measures that relate more closely to the diagnosis of diseases in real life situations, the relevance of a parameter can be evaluated by making a binary classifier from it with dichotomization, e. g. defining each value below a certain threshold limit to indicate a healthy case, and all values higher than the limit to indicate the presence of the disease. The classifier can then be evaluated against the Golden standard to evaluate its performance.

A classification result belongs then to one of four categories in relation to the Golden standard: True Positive (TP), True Negative (TN), False Positive (FP) and False Negative (FN). Two conventional statistical measures of *Sensitivity* and *Specificity* can be derived from these, see Figure 6.1. Sensitivity of a technique represents the classifier's ability to detect a disease if it is present, (Number of True Positives found by the classifier in relation to the total number of positive cases in the population, i. e. diseased subjects). Specificity is the classifier's ability not to be wrong when it classifies a case to be negative (Number of True Negatives found by the classifier in relation to the total number of negative case in the population, i. e. healthy subjects). Letting the threshold limit grow from small values to its highest value, we can generate a Receiver Operating Characteristic (ROC) curve [Br2006], see Figure 6.1 for illustration. The ROC curve is essentially a plot of the False Positive Rate (FPR, i. e. 1 - Specificity) on the x-axis, and the True Positive Rate (TPR, Sensitivity) on the y-axis.

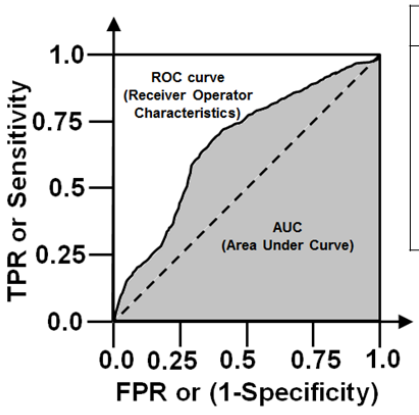

	Golden standard	
Tested method	True positive (TP)	False positive (FP)
	False negative (FN)	True negative (TN)

$$Sensitivity = \frac{TP}{(TP + FN)}$$

$$Specificity = \frac{TN}{(TN + FP)}$$

Figure 6.1: Receiver Operating Characteristics (ROC) curve. ROC curve gives the value of sensitivity for a given False Positive Rate. The dashed line depicts a random classifier. Area Under Curve (AUC) can be calculated with the trapezoid rule.

The ROC curve always grows monotonically. When the threshold gets higher numbers, more subjects are classified as disease cases (positives) and the Specificity is gradually lost (until all cases are determined as disease cases with Specificity 0), while at the same time Sensitivity increases (until all cases are classified as disease cases, including all true disease cases, thus making Sensitivity 1). To measure the diagnostic accuracy, the Area Under Curve (AUC) may be calculated for the ROC curve [Me2006]. It gets values in [0.0..1.0], where the AUC value 1.0 means that the classification with

the evaluation set did not show any errors (and 0.0 means perfect negative correlation that can be inverted to get AUC of 1.0), while the value 0.5 indicates that the usefulness of the classifier is equal to that of using a completely random classifier, i. e. flipping a coin. AUC can be used for testing the clinical relevance of a variable.

The AUC may be computed in a number of different ways [MaCr2005], including the ML-estimation (Maximum Likelihood) method requiring several iterations [DoAl1969]. When there is a large number of responses (i. e. Golden standard classifications), estimating AUC by the trapezoid rule [PoHs1969] gives a good estimate of the performance. Its calculation is fast and easy to understand, which makes it feasible to use when bootstrap instances of the AUC area are calculated. AUC expresses the general ability of the classifier to classify data into two groups. In practise, setting the threshold for positive-negative decisions depends on the needs of the particular application; costs of false decisions should be considered carefully here.

Another statistical measure used is *Spearman's rank correlation* coefficient (ρ). The statistics can be used for comparison of two sets of observations if the compared variables are not approximately normally distributed, which may often be the case for physiological quantities. The Spearman's ρ is defined between two sets of ranked (i. e. ordered) variables as:

$$\rho = 1 - \frac{6 * \sum d_i^2}{n * (n^2 - 1)}, \tag{6.6}$$

where d is the difference between rank numbers of the variable values. The value of ρ varies in $[-1..1]$, where -1 denotes negative and 1 positive monotonic association between the two sets of variables.

Digital images contain *quantization errors* because the real world phenomena that are represented by the images have been rounded and truncated in the image acquisition processes and stored into digital form. This may affect that two or more different observations have identical numbers in Eq. 6.6 (i. e. numbers are tied in the ranking). The identical numbers affect that the ρ may show too high association, because the true real data values are likely to have rankings that are different between the compared data sets. In such cases all of their values can be assigned to their average rank before calculation of the d.

6.2 Confidence Intervals of Statistical Descriptors

Medical imaging data are in most of cases very noisy and therefore individual observation includes uncertainty in relation to its assumed true value. In addition, the statistical descriptors contain uncertainties, which can be

expressed by the means of *Confidence Intervals* (CI). The CI is associated with a value range and a confidence level. The value range is around the value of the descriptor. The confidence level indicates the frequency for the true value to fall within the value range (e. g. 95% CI meaning 95% of time) when the process of obtaining sample data and calculation of the CI is repeated. The length of the CI can be used to represent the precision for the value, and it decreases when sample size increases. An analogue to the CI is the Bayesian concept of *credible interval*, where the interval is associated with a probability for the descriptor value to be inside the interval.

For Spearman's rank correlation (6.6), the CI value can be calculated analytically with Fisher's transformation [Fi1921]. It has been observed in [Ru2008] that *bootstrapping* (explained below) provides equally good or better CIs than analytical methods when the sample size is large enough (e. g. $N \geq 50$). With the assumption that sampling errors of the Fisher-transformed ρ (6.6) are normally distributed with variance $\sigma(z_\rho)$, the confidence interval of Spearman's rank correlation coefficient ρ is [Ru2008]:

$$z_\rho = \tfrac{1}{2} * \ln(\tfrac{1+\rho}{1-\rho}) = \operatorname{arctanh}(\rho) \tag{6.7}$$

$$CI(\rho) = \tanh(z_\rho \pm (\sigma(z_\rho) * t_{(1-CL)/2,n-2})) \tag{6.8}$$

where z_ρ is the transformed estimate of ρ, t is t-distribution value with confidence level CL (e. g. 0.025 for CL=0.05), and $n-2$ is degrees of freedom. Adjustments for estimate of the variance $\sigma(z_\rho)$ have been evaluated in [Ru2008]. It was observed in [Ru2008] that the estimate $(1+z_\rho^2/2)/(n-3)$ earlier presented in [BoWr2000] performed well among evaluated analytical methods.

For other parameters such as ICC or AUC, constructing an analytical CI may lead to difficulties. For ICC, analytical methods have shown poor performance [Uk2002], and well performing analytical methods are lacking. For AUC, there is the widely used Wald method which uses the CI of the difference between two AUCs [De1988]. However, this method may lead to questionable performance when the sample size is not large [Ob1998, De2012, Zo2013, Ko2014].

The value of CI can be calculated experimentally by resampling instances of the sample set, i. e. by *bootstrapping*. In the bootstrapping method, random subsets (called *bootstrap instances*) of the original samples are created and the subsets are treated as if they were the original sample in the calculation of the statistical descriptor. In *percentile bootstrapping*, the bootstrap distribution of statistics is calculated from the bootstrap instances. Then, percentiles (i. e. 2.5% and 97.5% percentiles) are used to approximate the CI. This method is easy to use, while it is to be noted

that it is based on the assumption that the bootstrap distribution is a good approximation to the true distribution of the statistics. The sample statistic may be compared to the mean (or median) of the bootstrap distribution to roughly evaluate the approximation. In the related *jackknife* method [Tu1958], the sampling is done by leaving out one or more items from the original sample set.

The replicates in bootstrapping can be created *with replacement* as originally proposed in [Ef1979] or *without replacement* (also called plainly 'subsampling') [PoRo1994]. In the former, a replicate of the same size as the original sample is created by taking random items from it using uniform distribution for generating the item indices. This allows the occurrence of duplicates, whereas in sampling without replacement, each object of the original sample may occur at most once. Because of replacement, the replicates in sampling with replacement are from a distribution that differs from the distribution of the original sample. In subsampling without replacement, the subsample size is smaller than the original sample size, but the samples are from the distribution of the original sample.

The subsampling technique is more generally usable than bootstrapping with replacement (i. e. when items are dependent, as in time series). When the sample size is small, bootstrapping with replacement is advisable. This is because the number of different replications is limited by the size of the original sample. This limitation may bring inaccuracies to the bootstrapped value for small sample sizes. When bootstrapping is applied to a descriptor that uses more than one group, i. e. AUC of a binary classifier or ICC, *stratification* may be applied for improving the accuracy of the statistics. Stratification of the sample set means that the replicates are created separately for each group (e. g. healthy, non-healthy), thus keeping the ratio of the group sizes the same as in the original sample. This in turn allows estimation of the bootstrapped descriptor value with a smaller number of replicates, because unrealistic replicates have been excluded. For example in the case of AUC, we are only interested in the classification of the samples into two groups, and therefore replicate samples that contain items from one group only do not contribute to the estimate.

For a bootstrapping procedure to work, it has to be assumed that the bootstrapped distribution approaches asymptotically the distribution of the whole population. For this assumption to hold, the original sample is required to represent the population properly. For example in a situation where the population does not consist of independent, identically distributed values, the bootstrap sampling fails because random sampling does not preserve the characteristics of the whole population.

In situations where bootstrapping fails, subsampling may be applied. It requires only that the convergence rate of the estimator for the statistic is known, the limiting distribution is continuous, and that its replicate size

tends to infinity with the sample size so that the ratio of these sizes converges to zero [Be1999]. For this reason bootstrapping can be used with various statistical descriptors where analytical solutions are lacking. This property is particularly useful for descriptors for which it is difficult to define CI in an analytic form, such as ICC.

It is common that a number of different variations of classifiers have been constructed on the basis of the same data set. The AUC values of the classifiers can then be statistically tested (compared) with the bootstrapping method as originally described by Hanley and McNeil [HaMc1983] and later modified in [Ro2011]. Consider two variants 1 and 2 of a classifier. Let θ_{1r} and θ_{2r} be the *bootstrapped instances* of two AUC values θ_1 and θ_2 that are compared. Then, a distibution can be generated for the bootstrapped differences $D = D_1, ..., D_N$ (where N is the number of bootstrap replicates) between the two AUCs θ_1 and θ_2:

$$Z = \frac{\theta_{1r} - \theta_{2r}}{SD(D)} \tag{6.9}$$

In Eq. 6.9, Z is approximately normally distributed and then one- or two-tailed p-values of t-test may be calculated for the significance of Z.

6.3 Distortions in the Intensity Distribution of the Data

The intensities of an image may be distorted. Sometimes the distortion has negligible contribution to the image quality, when compared to other effects (e. g. in the presence of small movements in an image with large PVE). Some of these effects are mentioned here for the sake of completeness. In scanning situations where the target object moves, motion artefacts occur in the image. For PET, the time required to acquire a single 3D time frame (with adequate SNR) is relatively long (e. g from few seconds to tens of minutes), which may add motion blur to the acquired data.

For MRI, motion artefacts are different within and between slices. This is due to data that are acquired in Fourier Space before being transformed to spatial images. Depending on the MRI scanning sequence, the movement is distributed differently, i. e. the image slices may be obtained in transaxial, coronal or sagittal direction, or multiple slices are taken simultaneously (as in multiband echo planar imaging).

The images are blurred by rigid and non-rigid motion of the objects. Rigid motion is relatively easy to correct by applying rigid image co-registration procedures between time frames, but non-rigid motion is harder to address if the quality of the acquired data is not sufficient for detecting anatomical (structures) information.

In addition, PET data are also blurred by PVE, where intensity is blurred by Point Spread Function (PSF) to neighbouring regions. The PVE blurs intensity for a point shaped object to the whole voxel volume, and correspondingly, increases the observed intensity for neighbouring regions. PVE includes a voxel effect where the signal reflects the average value within the voxel.

6.4 Phantom Objects and Computer Simulations for Method Evaluations (P1)

While the true signal intensity and imaging errors are both not known in a scanning situation, the imaging errors imaging can be estimated by using data from physical and digital phantoms. Phantom image data are artificially created either by placing an artefact into the scanner FOV (Field of View), or by adding noise and distortions to a digital, artificially produced image. In this manner, the true intensity values are known, and thus deviations from it can be measured.

In order to use a physical phantom in PET, (Fig. 6.2), the true localization and activity concentration of the inserted source must be known. The latter can be calculated from the half-life of the inserted tracer and the time elapsed from external measurement to the acquisition event. For the localization, an anatomical reference image needs to be obtained from the accompanied CT or MRI device, or else the quantification on the PET image must take into account the PVE by taking samples from locations which are unaffected by the PVE (i. e. they are far from the edges of homogenous region).

For a digital PET phantom, the true intensity and its localization are simple to generate, since the image is digitally created. Various digital phantom images with different levels of detail including motion simulation are available for free and commercially [Xu2014].

When suitable digital data are available, the challenge is to simulate the noise and other artefacts in a realistic manner. When small computational cost is desirable, PVE can be simulated by applying Gaussian smoothing to the phantom data (denoted here by $I_{Phantom}$). The phantom contains a predetermined activity distribution that is compared to the measurements after simulation. The $I_{Phantom}$ is smoothed with the convolution operation "$\otimes$" to create a smoothed image $I_{PSFSimulated}$.

For including noise in the simulation, Poisson noise $Poisson()$ can be added to the image $I_{PSFSimulated}$ in Radon domain $\Re()$. PET image $I_{PSFandNoiseSimulated}$ is then reconstructed as follows:

$$\begin{aligned} I_{PSFSimulated} &= I_{Phantom} \otimes I_{PSF} \\ I_{PSFandNoiseSimulated} &= \Re^{-1}(Poisson(C_{noise} * \Re(I_{PSFSimulated}))) * \frac{1}{C_{noise}} \end{aligned} \tag{6.10}$$

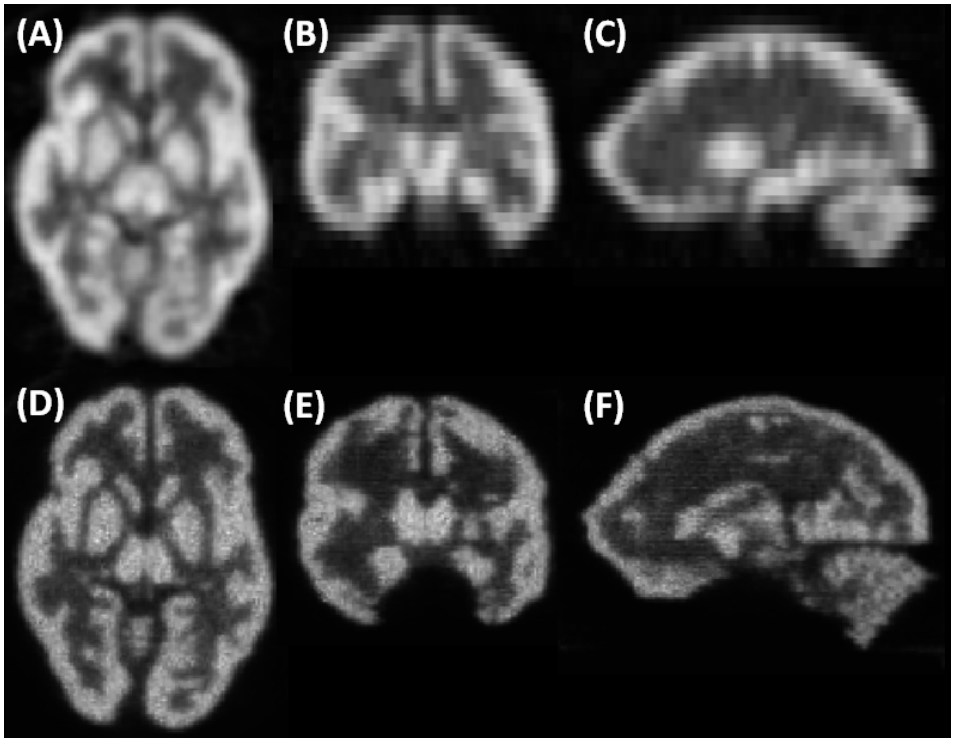

Figure 6.2: PET images of the so-called Hoffman brain phantom. First row: GE Advance scanner. Second row: High resolution Siemens (HRRT) scanner. Images are in transaxial (A,D), coronal (B,E) and sagittal (C,F) orientations.

A more exhaustive but also computationally more costly approach is the Monte Carlo simulation [Ro2006, Gi2016]. Widely used software packages for that purpose are PET-SORTEO [Re2004], and GATE [Ja2004]. Both of these simulate the PET acquisition process in detail including simulation of the gamma ray trajectories in 3D space. Challenges in them are the excess amount of computations and the complexity of the system. These limit the use of simulation when numerous phantoms are needed. In addition,

the simulations become specific to the particular PET system, thus making results less easily generalizable. Nevertheless, Monte Carlo simulators are used in various applications in PET, such as in calculation of the system matrix used in the PET image reconstruction [Bu2016].

6.5 Effects that Affect the Quality of PET Images and Correcting them (P1)

In addition to the error factors mentioned above (random events, attenuation, scatter), there are other sources of errors which hamper the PET image quality. Before annihilation, the positron travels a distance depending on the radioactive nuclide. The length of the motion is in average from less than one millimeter to several millimeters in a random direction from of the decaying point. In annihilation, the emitted gamma photons are not oriented in exactly opposite directions, which leads to a minor additional error in the localization data. The signal itself consists of photons, and the type of related noise is Poisson [Sa2009]. Noise can be reduced to some extent by injecting more radioactive tracers into the subject, but this may be costly, and it is not desirable due to the extra radioactivity exposure, particularly in the case of humans.

A notable factor affecting the image quality is the *Partial Volume Effect* (PVE) where images are blurred due to limited resolution of PET devices. PVE can be modelled as a convolution between the true signal I_{True} and the *Point Spread Function* (PSF). In addition, the observed image $I_{Observed}$ includes additive noise:

$$I_{Observed} = I_{True} \otimes I_{PSF} + noise \tag{6.11}$$

Because of the noise, the solution of I_{True} (2.1) becomes an ill-posed problem which is hard to solve analytically. The problem can be partially solved with the High Resolution Research Tomograph brain PET scanner (HRRT, Siemens Healthcare Inc. Knoxville, U.S. [Jo2007]). Due to advanced hardware components and smaller FOV of HRRT than conventional PET devices, HRRT has, a better physical resolution of around 3 mm in contrast to 5-6 mm, of conventional scanners. The strength of PET is in its quantitative accuracy on molecular level, and the relatively low spatial resolution can partially be compensated by accompanying CT of MRI imaging. Unfortunately, the PVE hampers quantification of the activity intensities, and motion artefacts are often unavoidable in PET imaging due to the low temporal resolution [Bo2010] in situations where high temporal sampling rate cannot be achieved while maintaining adequate SNR of samples. Therefore, the need for PVE correction for better absolute quantification is evident.

Various PVE correction methods have been suggested for PET and SPECT. Spatial resolution blur can be corrected by using supplementary anatomical information from CT or MRI [Me1990, Mü1992, Al2004, Co2013], or by relying only on the PET image data [Bo2009, Te2009]. Another technique is to correct the PVE already on the sinogram level and in this way avoid the distortion caused by the PET reconstruction process [Pa2006].

The PET modality has a rather low temporal resolution due to the relatively low signal count rate in order to obtain enough statistics for a reasonable SNR. It is therefore unavoidable that motion artefacts occur, particularly when the target organ under study is constantly moving, such as lungs or heart. The motion can be corrected before image reconstruction with supplementary information about motion acquired with monitoring devices for head, chest and cardiac movements [Ra2007]. The motion can also be measured with other modalities like CT and MRI. When the motion has been measured along with the PET data, it can be corrected by reconstructing the data in phases or gates within cardiac or respiratory cycles [Ne2003]. The idea here is that each gate contains multiple observations of the signal within the same phase of the cycle in order to increase SNR of the data. Another method for correcting motion artefact is to use inversion technique for motion blur, given that the motion is properly measured on the voxel level [Na2006].

6.6 Correcting for Partial Volume Effect (P1)

The correction for PVE (called shortly PVC) is an inverse problem for the generation of the source data that is inherently *ill-posed*, meaning that no unique solution exists, and small change to the image with PVE to be corrected produces large changes to solution. Therefore, various approaches have been proposed for correcting PVE. The *Geometric Transfer Matrix* (GTM) method by Rousset et al. [Ro2000] assumes that the image can be divided into a set of regions (indexed from 1 to n).

The observed intensities are expressed as a system of linear equations which are solved by inverting the GTM [Th2001]. These can be expressed as:

$$\begin{bmatrix} I_{Observed_1} \\ I_{Observed_2} \\ \vdots \\ I_{Observed_n} \end{bmatrix} = \begin{bmatrix} w_{11} & w_{12} & \cdots & w_{1n} \\ w_{21} & w_{22} & \cdots & w_{2n} \\ \vdots & \vdots & \ddots & \vdots \\ w_{n1} & w_{n2} & \cdots & w_{nn} \end{bmatrix} \times \begin{bmatrix} I_{Corrected_1} \\ I_{Corrected_2} \\ \vdots \\ I_{Corrected_n} \end{bmatrix} \tag{6.12}$$

$$\begin{bmatrix} I_{Corrected_1} \\ I_{Corrected_2} \\ \vdots \\ I_{Corrected_n} \end{bmatrix} = \begin{bmatrix} w_{11} & w_{12} & \cdots & w_{1n} \\ w_{21} & w_{22} & \cdots & w_{2n} \\ \vdots & \vdots & \ddots & \vdots \\ w_{n1} & w_{n2} & \cdots & w_{nn} \end{bmatrix}^{-1} \times \begin{bmatrix} I_{Observed_1} \\ I_{Observed_2} \\ \vdots \\ I_{Observed_n} \end{bmatrix}$$

where the weights w compose the GTM matrix, and represent the transfer of intensity values between the regions. The main limitation of this method is the assumed homogeneity of the intensities inside each region $[1..n]$; division of a PET image into such segments (with homogenous activity distributions) can be challenging. Errors from segmentation may be avoided with the deconvolution approach that does not use segmentation (see below) [ToRe2008]. Given that the assumption about homogeneity holds, this method produces accurate estimates of the true mean intensities inside the regions.

The task of PVC in voxelwise manner can be divided into two parts; correcting the effect of spill-out activity from a ROI, and correcting the opposite spill-in effect. Considering the spill-out effect alone, the corrected activity is obtained by dividing the observed activity with the simulated spilled out activity distribution [Me1990]:

$$I_{Corrected} = \frac{I_{Observed}}{X_{ROI} \otimes I_{PSF}}, \tag{6.13}$$

where X_{ROI} is a binary mask that defines the voxels belonging to the ROI. Correspondingly, the spill-in activity from a neighbouring region can be removed from the observed activity giving [Mü1992]:

$$I_{Corrected} = I_{Observed} - (C_{Neighbour} * (X_{ROI} \otimes I_{PSF})), \tag{6.14}$$

where $C_{Neighbour}$ is the estimated true intensity of the neighbouring region. The intensity $C_{Neighbour}$ can be estimated by taking average of the region. Both of the above methods (6.13) and (6.14) require accurate segmentation of the underlying anatomy in X_{ROI}. Accurate segmentation may be hard to carry out, particularly if the target object moves or complementary images for anatomy are not available.

For brain imaging, an estimation method was suggested to estimate WM region intensity [Al20014], because voxels that are not contaminated by spill-in from GM may not exist in the image. The estimation for WM was defined as the intercept of linear fitting line of PET intensity values in brain image voxels against fraction of GM intensity in voxel after smoothing. The linear regression line is fitted to scatter plot $(GM_{fraction}, Y)$ of PET image voxels, where:

$$Y = PETintensity \tag{6.15}$$

$$GM_{fraction} = \frac{C_{GM}}{(C_{GM} + C_{WM})} \tag{6.16}$$

$$C_{WM} = X_{WMROI} \otimes I_{PSF} \tag{6.17}$$

$$C_{GM} = X_{GMROI} \otimes I_{PSF} \tag{6.18}$$

X_{GMROI} and X_{WMROI} refer to binary segmentations of Gray Matter and White Matter, and C_{GM} and C_{WM} are the corresponding convoluted images as in (6.13) and (6.14). The intercept at $GM_{fraction} = 0$ is then the estimation of true WM intensity.

6.7 Data-driven Segmentation for Premature Infant Brain MR Images (P2)

In MR images, PVE is due to the limited spatial resolution of the technique (i. e. resolution is set low for sake of reasonable acquisition time), even though it is higher than in PET. MR images are reconstructed from noisy signals in the Fourier space. The main source of noise is thermal noise due to thermal vibrations of ions and electrons and movements of the objects during data acquisition. The noise is of Gaussian type in real and imaginary channels after inverse Fourier transform in the image reconstruction. It then becomes Rician after calculating magnitude of the signal. Therefore the noise is generally Rician distributed in the MR images, even though at higher SNR levels the distribution can be approximated with Gaussian distribution [GuPa1995]. Often a logarithm is taken from the MR signal consisting of decay curve. This operation cahnges also the noise distribution [Sa2011].

MRI has relatively high temporal resolution for acquisition of a single data item, e. g. a slice of k-space. Because of this, the individual data items

contain less motion. If motion occurs during the acquisition, the data are collected from a wrong spatial position. As a result of this, the reconstructed image in the spatial domain contains so-called ghosting artefacts due to missing coefficients in the Fourier domain. Considering post-processing methods, motion artefacts can be corrected with the help of external devices [Za2006] or so-called navigator frames [Ke2008]. It may also be possible to detect motion from the image data themselves, under the assumption that motion in the image is small so that there is only minor loss of data [Lo2015]. With small children, the motion is largely an unavoidable problem that can partially be addressed by repeated measurements (see e. g. [Fu2003]). However, depending on the study question, it can be possible to extract meaningful information even from the corrupted MRI data [P2].

The data-driven segmentation technique in [P2] begins with inhomogeneity correction for removing large-scale variation in the image in T1 and T2 weighted input data. Then, the watershed algorithm is applied to an averaged gradient calculated from the T1 and T2. Finally, the Gaussian Mixture Model (GMM) including special handling of myelination segments is applied to the image.

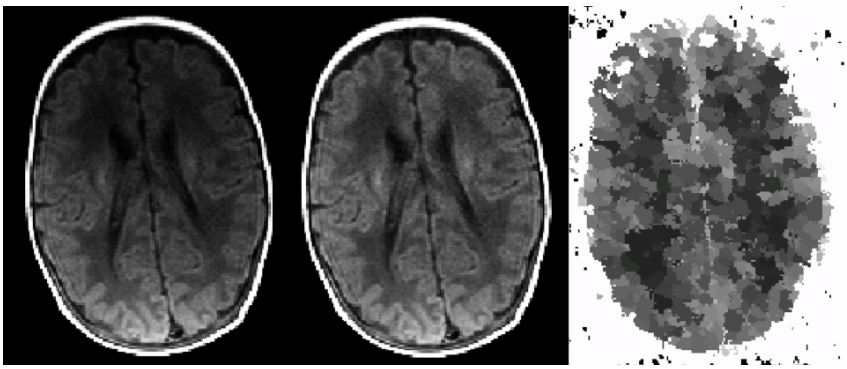

Figure 6.3: Examples of transaxial slices in steps of a data-driven segmentation technique using the algorithm of [P2]. From left to right: original T1 image, N3 inhomogeneity corrected image and watershed labelled image.

6.8 Comparison of DWI Models with Simulations and Real Data (P3 to P6)

The DWI signal is reconstructed from complex data by the means of inverse Fourier Transform. The performance of different DWI models can be evaluated by simulations where different levels of oise are added to the input signal. For this let S(b) be a DWI signal without noise. A noisy

signal is created with two independent Gaussian distributions $n_{real}(b)$ and $n_{imaginary}(b) \sim \mathcal{N}(0, \sigma^2(b))$ as:

$$S(b)_{simulated} = \sqrt{(S(b) + n_{real}(b))^2 + (n_{imaginary}(b))^2} \tag{6.19}$$

After added noise, the simulated signal is fitted and acquired model parameters in Eqs. (3.1), (3.2), (3.3), (3.4) are compared to the values used when creating original signal without noise.

Computer simulations with different levels of noise were used in [P3-P6] to evaluate a set of fitting procedures, followed by real data evaluations to test the usability of models in clinical context. In the simulations the noise levels were below and above the noise level estimated from the real DWI data. The noise in a real DWI signal is basically Rician distributed (and Rayleigh at lower SNR levels, such as background). Both simulated and real DWI signal were fitted with $RMSE$ (Eq.3.9) assuming uniform noise distributions among b-values. This approach is an approximation of a real situation as noise in the higher b-values is larger than in lower b-values. However, the same fitting procedures were applied to simulated and real data, which makes possible biases from Rician noise to be similar to both data. In practise, normality of the residuals can be assumed when SNR of the signal is high. one can then use a measure that assumes normality of residuels. In [P4] the evaluation of imaging data models was based on $\Delta AICc$ and ICC. Out of these the two last ones relate closely to clinical usability of the techniques.

For real data in [P5], 12 b-values were used in the original scan. From these 12, 210 subsets were created with six b-values each. The subsets were then used in evaluations. For observing the distribution of performance measures from all subsets, they were ordered by the goodness measure such and $RMSE$ and $ICC(3,1)$, and then plotted against those measures (having order at x axis and goodness measure at y axis, see Fig. 7.4). The shape of the curve shows then the performance of the DWI model parameters in relation to the placement of the b-value. For a flat curve, the placement of the b-values has little relevance, while a steeply descending curve means that the placement is crucial and setting of the b-value should be considered more carefully.

In model fittings, the multiple-initialization technique was used. Global optimization procedures were left for future studies, as for sake of model comparison it was considered crucial to avoid local minima. The initializations were spaced evenly so that balance was maintained between reasonable computation speed and avoiding local minima in fitting of the noisy signal.

Chapter 7

Results

The current thesis contains publications (P1) to (P6), which address overlapping areas of medical imaging. The topics are summarized in the table below:

Addressed topic	P1	P2	P3	P4	P5	P6
Repeatability of measurements	X		X	X	X	
Diagnostic accuracy				X	X	X
Image segmentation		X				
Partial Volume Effect	X					

7.1 Comparison of Partial Volume Effect Correction Techniques for Brain PET (P1)

In publication [P1] four PVE correction techniques were compared [Al2004, Ro2000, Mü1992, Me1990] in PET brain imaging when using the [^{18}F]FDG tracer with phantom and the [^{11}C]-raclopride tracer for repeatability. In the phantom studies, the correction techniques were compared for quantification accuracy. In the repeatability tests with real PET brain data, each patient was scanned twice. It was shown that selection of the most suitable PVC technique depends on the study question. Namely, a more complex method that tends to produce accurate results in quantitative measures, may be outperformed by other methods when considering the reliability of the results in real data.

In [P1], Hoffman Brain Phantom was scanned with three different scanners differing particularly in their PSF, which gives some generality to the performance evaluation. The phantom consisted of plastic plates that had a human brain -like container carved into them. The container was filled with [^{18}F]FDG liquid, and then scanned with three PET scanners, GE Advance (GE Healthcare, Millwaukee U.S.), GE DSTE (GE Healthcare, Millwaukee U.S.) and Siemens HRRT (Siemens Healthcare, Knoxville, Tennessee, USA),

of which the last one has particularly high (2.5-3.0 mm) and the two former lower (5-6 mm), more conventional resolution. The voxel sizes of the reconstructed images for scanners were, correspondingly: 1.17x1.17x1.17, 1.82x1.82x3.27 and 1.22x1.22x1.22 mm. The phantom experiments showed that the PVC method with sophisticated estimation of the mean brain white matter activity [Al2004] produced the best overall results when evaluted in all the three scanners. The method has the favorable capability of performing the PVE correction in a voxel-wise manner in comparison to the region-wise correction in [Ro1998].

Test-retest setting of patient data was used to evaluate the performance of the correction methods for the *in vivo* situation. The data consisted of eight healthy volunteers. Each of them was scanned twice with [^{11}C]-raclopride, which is a dopamine antagonist. The analysis was performed at ROI level in four subcortical regions that accumulate the tracer. The SD was observed to rise after correction which can be considered to be due to noise amplification of PVC. The $ICC(3,1)$ values revealed that noise amplification in PVC propagates to affect also the ROI level analysis (see SD values of the ROI mean intensities over subjects in Table 7.1), and the increase of noise is therefore an issue to consider when making corrections, even if only mean ROI values are considered after PVC.

Table 7.1: Effect of the positron emission tomography PVC methods on binding potential estimated by a reference tissue model for two brain regions.[1]

Method	Putamen Mean±SD	Putamen $ICC(3,1)$
No correction	1.31±1.22	0.91
[Al2004]	2.27±1.81	0.94
[Mü1992]	1.86±1.70	0.88
[Ro2000]	1.28±1.60	0.92
[Me1990]	1.33±1.24	0.92
	Lateral thalamus Mean±SD	Lateral thalamus $ICC(3,1)$
No correction	2.10±1.69	0.83
[Al2004]	2.71±2.50	0.98
[Mü1992]	2.40±2.26	0.93
[Ro2000]	2.24±2.30	0.94
[Me1990]	2.19±1.71	0.87

[1]Adapted from "Evaluation of partial volume effect correction methods for brain positron emission tomography: Quantification and reproducibility", by Merisaari H., Teräs M., Hirvonen J., Nevalainen O.S., Hietala J., 2007. Journal of Medical Physics, 32(3), pp. 108-117. Copyright 2006-2016 by Journal of Medical Physics.

7.2 Segmentation of Anatomical MR Images Having Low Signal-To-Noise Ratio (P2)

The segmentation method in [P2] represents one of few segmentation techniques for neonatal MR images that do not use spatial prior. In the technique, the image data are first segmented with the watershed transform. The result is then clustered according to the intensity values in order to create a rough segmentation of the watershed regions. The rough segmentation is used as *a priori* information in the final segmentation by the Expectation Maximization -algorithm that operates on voxel intensities.

The segmentation method was validated against manual volume measurements of the combined brain tissue (brain white matter (WM) and gray matter (GM)) of 11 newborn subjects some of whom had large anomalies in brain shape, see [P2], Fig. 7.1.

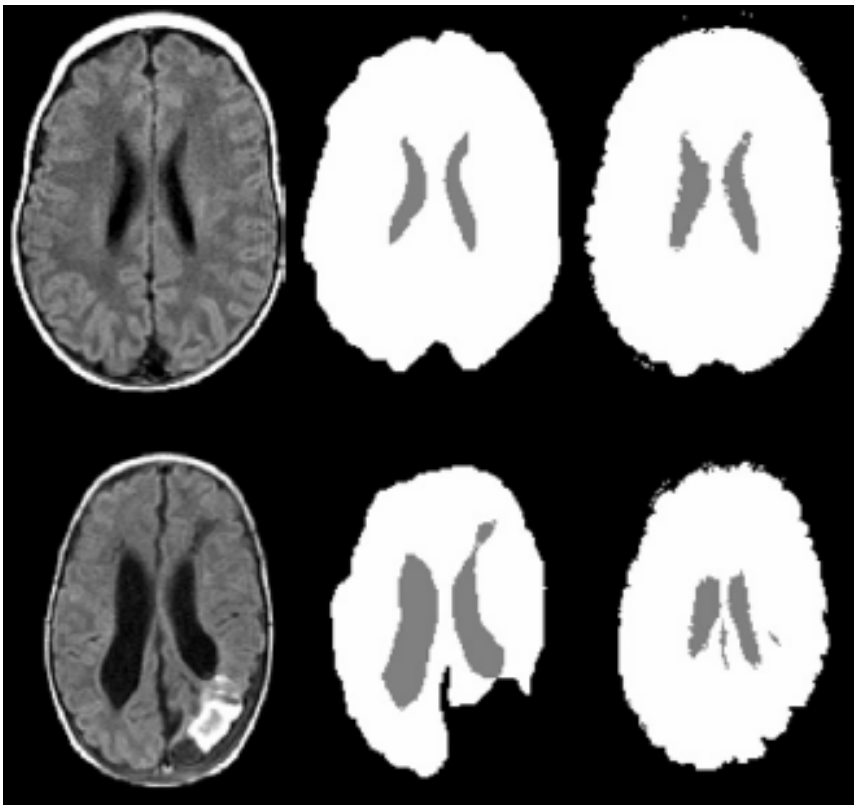

Figure 7.1: Segmentation of the CSF and GM+WM regions of MR images from premature infants without and with anomaly.[2]

[2]Adapted with permission from "Gaussian mixture model-based segmentation of MR

Correlation of the volume measures between the algorithm using both T1- and T2-weighted images and manual segmentation was 0.94 for GM+WM region and 0.95 for CSF. In addition, cases for voxelwise comparison between the proposed and manual segmentation are presented in Table 7.2. The method uses both T1 and T2 weighted images for the segmentation, and it has slightly inferior performance when run with T2 images, only.

Table 7.2: Confusion matrices of the data-driven segmentation method (WSEG) against expert segmentation for three premature MR images. The agreement of segmentation is shown on the diagonal in each matrix. GM+WM: Union of Gray and White Matter. CSF: Cerebrospinal Fluid.[3]

	GM+WM	CSF	Non-brain
Subject 5			
GM+WM	92.3%	1.5%	6.1%
CSF	24.3%	75.7%	0.0%
Non-brain	0.4%	0.0%	99.6%
Subject 8			
GM+WM	81.5%	2.2%	16.3%
CSF	17.2%	82.8%	0.0%
Non-brain	0.3%	0.0%	99.7%
Subject 9			
GM+WM	86.6%	5.7%	7.7%
CSF	18.6%	72.8%	8.6%
Non-brain	0.9%	0.0%	99.1%

7.3 The Effect of Sample Points for DWI Modelling in Terms of Repeatability (P3 to P6)

Publications [P3-P6] address the repeatability of DWI measurements in the context of prostate imaging. Good repeatability of the DWI technique is essential for reliable diagnosis, such as detection and characterization of *Prostate Cancer* (PCa).

[P3]: *Optimization of b-value distribution for biexponential diffusion-weighted MR imaging of normal prostate.* We simulated the DWI decay

images taken from premature infant brains", by Merisaari H., Parkkola R., Alhoniemi E., Teräs M., Lehtonen L., Haataja L., Lapinleimu H., Nevalainen O.S., 2009. Journal of Neuroscience Methods, 182(1), pp. 110-122. Copyright 2009 Elsevier B. V.

[3]Adapted with permission from "Gaussian mixture model-based segmentation of MR images taken from premature infant brains", by Merisaari H., Parkkola R., Alhoniemi E., Teräs M., Lehtonen L., Haataja L., Lapinleimu H., Nevalainen O.S., 2009. Journal of Neuroscience Methods, 182(1), pp. 110-122. Copyright 2009 Elsevier B. V.

curves on various Rician noise levels, and found that placing the b-values in three clusters minimizes the amount of errors in the parameters f_{biexp}, $D_{f_{fast}}$ and D_{slow} (fraction term, fast diffusion, and slow diffusion) of the biexponential model. This result is consistent with the results from real data evaluations of healthy prostate tissue in f_{biexp} and D_{slow}, see Fig. 7.2.

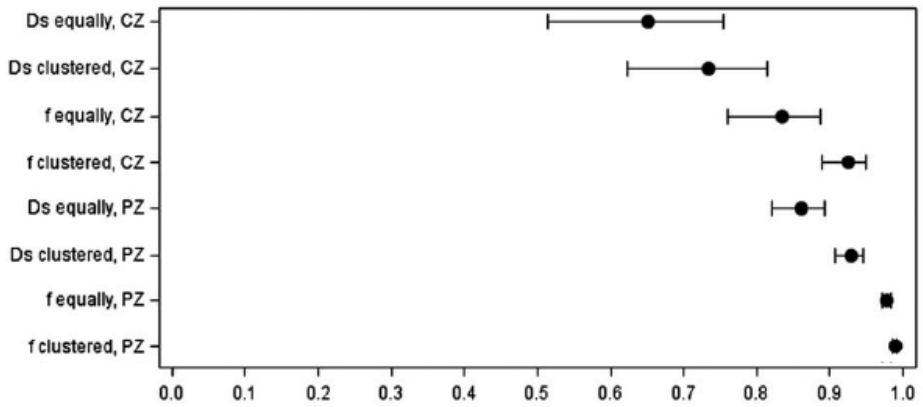

Figure 7.2: ICC calculated using Shrout and Fleiss analysis for f_{biexp} and D_{slow} values derived from the clustered and equally distributed b-values of Periferal Zone (PZ) and Central Zone (CZ). ICC with 95% confidence are shown.[4]

The 'clustered' placing of b-values produced higher $ICC(3,1)$ values than conventional uniform positioning of b-values ('uniform' approach). Particularly, the 'clustered' approach improved $ICC(3,1)$ of the f_{biexp} parameter in the central zone of the prostate. The f_{biexp} parameter was the only parameter with good overall reliability in terms of $ICC(3,1)$, while the D_{slow} parameter had the best reliability in the periferal zone of the prostate. In this zone, the 'clustered' approach did not improve f_{biexp}. On the other hand, the relialibity of the f_{biexp} parameter was excellent already when using the conventional method of uniformly distributed b-values. The 'clustered' setting of b-values produced parameter map images of $D_{f_{fast}}$ that had more larger-scale variation caused by susceptibility artefacts, than with the 'uniform' approach. That was speculated to be the reason for a lower $ICC(3,1)$ value with the $D_{f_{fast}}$ parameter which is seemingly most sensitive to variations in data. For minimizing the DWI acquisition time, the effect

[4]Adapted with permission for academic use from "Optimization of b-value distribution for biexponential diffusion-weighted MR imaging of normal prostate" by Jambor I., Merisaari H., Aronen H.J., Järvinen J., Saunavaara J., Kauko T., Borra R., Pesola M., 2014. Journal of Magnetic Resonance Imaging, 39(5), pp. 1213-1222. Copyright 2013 Wiley Periodicals, Ins.

of the number of b-values on the error of the parameter estimates was investigated, see Fig. 7.3. It was found that the use of 5 or 6 b-values is of benefit in comparison to fewer b-values, while adding more than 10 b-values to the scanning sequence led to only a negligible decrease in the error of the parameter values.

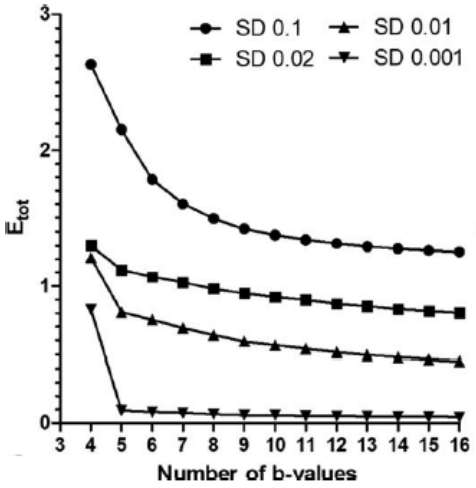

Figure 7.3: Dependence of the mean total error (E_{tot}) on the number of b-values used in the fitting procedures when the standard deviation of the noise was 0.1, 0.02, 0.01, and 0.001. The parameter set by [Mu2006b] was used in simulations.[5]

[P4]: *Evaluation of different mathematical models for diffusion-weighted imaging of normal prostate and prostate cancer using high b-values: A repeatability study.* In continuation to [P3], in [P4] the biexponential diffusion model (Eq. 3.4) was compared with three other DWI models (monoexponential (Eq. 3.1), kurtosis (Eq. 3.2) and stretched (Eq. 3.3) exponential models). To do this, two repetitions of DWI images from 8 healthy volunteers and 16 PCa patients were analysed to test the reliability of the model parameters to separate between healthy and PCa cases. All available b-values were used for healthy (16 b-values) and for PCa (12 b-values) subjects. Table 7.3 compares the four DWI models in terms of $AICc$ (Eq. 3.13) and percentage of cases in which a simpler model is rejected with the significance level 0.01 with F-ratio. For PCa patients, in only slightly over half of the cases the

[5]Adapted with permission for academic use from "Optimization of b-value distribution for biexponential diffusion-weighted MR imaging of normal prostate" by Jambor I., Merisaari H., Aronen H.J., Järvinen J., Saunavaara J., Kauko T., Borra R., Pesola M., 2014. Journal of Magnetic Resonance Imaging, 39(5), pp. 1213-1222. Copyright 2013 Wiley Periodicals, Ins.

biexponential model gave a better fit than the kurtosis model.

From tests with humans and from simulations with different noise levels, it is evident that the biexponential model overfits the data, and therefore better fits (Table 7.3) are actually due to noise in the parameters. It turned out that the monoexponential model was the most robust model against noise at high noise levels. Still, the $AICc$ values of the four models approach each other when the noise level increases, thus making their $\Delta AICc$ difference to disappear. The noise level of the *in vivo* data is low; e. g. in the human data the SNR was estimated to be between 0.01 and 0.02 with a conventional 3T MR scanner.

Table 7.3: Selection of preferred DWI model for PCa diagnostic. 'PCa' stand for % of cases with cancer and 'Normal' for % of cases of normal tissue samples.[6]

	Region	
AIC_c	PCa	Normal
Stretched vs monoexponential	100%	100%
Kurtosis vs monoexponential	100%	100%
Biexponential vs monoexponential	100%	100%
Kurtosis vs stretched	43.8%	60.9%
Biexponential vs stretched	57.8%	81.2%
Biexponential vs kurtosis	85.9%	81.2%
	Region	
F-ratio	PCa	Normal
Stretched vs monoexponential	98.4%	100%
Kurtosis vs monoexponential	98.4%	100%
Biexponential vs monoexponential	98.4%	100%
Biexponential vs stretched	48.4%	65.6%
Biexponential vs kurtosis	56.3%	53.1%

[P5]: *Optimization of the b-value distribution for four mathematical DWI models.* We studied the placement of b-values for the four DWI models used in [P4]. The placement of b-values was studied in terms of GoF and $ICC(3,1)$ for b-values in the range of $[0..2000 s/mm^2]$ by using Monte Carlo simulations and real data of ten PCa patients. It was found that the reliability of the DWI measurements can be improved in most of these models,

[6] Adapted with permission for academic use from "Evaluation of different mathematical models for diffusion-weighted imaging of normal prostate and prostate cancer using high b-values: A repeatability study", by Jambor I., Merisaari H., Taimen P., Boström P., Minn H., Pesola M., Aronen H.J. 2015. Magnetic Resonance in Medicine, 73(5), pp. 1988-1998. Copyright 2014 Wiley Periodicals, Inc.

by using a proper number of b-values: 4-5 for the monoexponential, 6-7 for stretched and kurtosis models and 8-10 for the biexponential model. Further, our results suggest that using six b-values results in high repeatability of measurements (ICC(3,1) > 0.8) independent of their placement, see [P5], Fig. 7.4 (D). The placement of b-values affects the goodness of the fit more when measured with the $RMSE$ (Eq. 3.9) (Fig. 7.4 (A)).

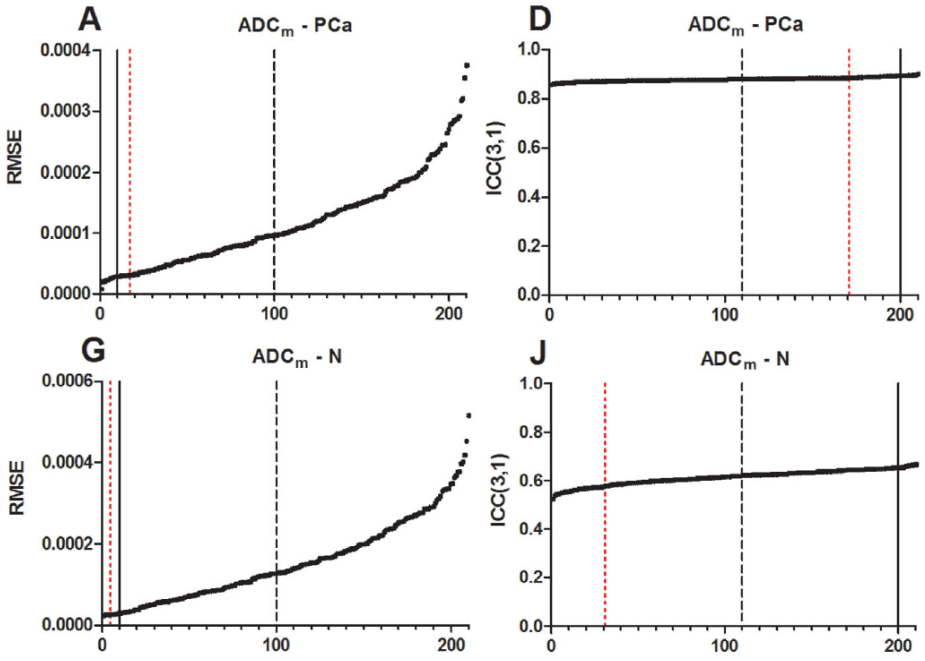

Figure 7.4: The root mean square error ($RMSE$) (A, G) and intraclass correlation coefficient. ($ICC(3,1)$) values (D, J) for the $ADCm$ parameter of the monoexponential model calculated using different sets of six b-values. Results for PCa patients (A) and normal cases (G) are shown. The best 10 b-value distributions based on the $RMSE$ (A, G) and ICC values (D, J) are separated by the solid line. The dashed line is used to mark the best 100 b-value distributions. The dotted line marks b-value distributions, consisting of six equally distributed b-values (0, 100, 700, 1500, 1700, 2000 s/mm^2, in addition to the initial two b-values that were kept fixed in all b-value distributions).[7]

[7]Adapted with permission for academic use from "Optimization of b-value distribution for four mathematical models of prostate cancer diffusion-weighted imaging using b values up to 2000sec/mm^2: Simulation and repeatability study", by Merisaari H., Jambor I., 2014. Magnetic Resonance in Medicine, 73(5), pp. 1954-1969. Copyright 2014 Wiley Periodicals, Inc.

As shown in [P4], in comparison to the monoxponential model, the kurtosis model explains the decay curve better (considering $RMSE$) with one added parameter K. With the kurtosis model, the parameter representing simple diffusion (ADC_k) behaves similarly to the ADC_m in the monoexponential model. For the K parameter, optimal placement of b-values results in better repeatability (i. e. $ICC(3,1)$), particularly in healthy controls.

[P6]: *Correlating mathematical models with Gleason score and repeatability.* By using the same DWI models as in [P3-P5], we compared the model parameters to the Gleason scores (Gs) [Ep2005] which are currently used to make a prognosis of PCa. Gleason scores (Gs) were assigned to each prostate according to the consensus of two experienced pathologists. The Gleason scores were divided into less aggressive (Gs '3+3') and more agressive cases (Gs > '3+3'), and used as a ground truth for the classification of the subjects into these two groups. The AUC of the agressiveness levels was used as an overall measure of the classification accuracy of the DWI model parameters. As another measure for relation to Gs, we applied nonparametric Spearman's rank correlation (Eq. 6.6). For repeatability of the model parameters, the study involved a patient population of 55 patients which had two repeated DWI acquisitions. Repeatability was measured with the Coefficient of Repeatability divided by the median $CR/Median$ (Eq. 6.5), and with $ICC(3,1)$.

The findings from [P3] and [P4] were verified for repeatability. There was four repeatable DWI model parameters ($ADCm$, $ADCk$, K, $ADCs$, see Table 7.4) that had also the highest associations with the Gleason score, as shown in Fig. 7.5.

The same parameters had the best AUC values for making a classification between the tumour agressivity classes '3+3' and > '3+3', see Fig. 7.6 (b) in [P6]. However, the confidence intervals of the AUC values wide and overlapping. It was shown (Fig. 7.6 (a)) that D_{slow} for slow diffusion could be used in classifying between normal and cancer tissues.

Table 7.4: Repeatability of fitted parameters. PZ: Periferal Zone ROI. CG: Central Gland ROI.[8]

		Region		
	Parameter	all PCa	PZ PCa	CG PCa
$CR/Median$ (%)	ADC_m	20.6	21.8	15.1
	ADC_k	23.1	25.1	16.5
	K	16.4	15.6	19.8
	ADC_s	23.8	25.2	18.1
	α	12.7	12.8	10.2
	f_{biexp}	87.4	90.1	85.8
	$D_{f_{fast}}$	143.2	156.7	98.0
	D_{slow}	82.4	86.8	70.9

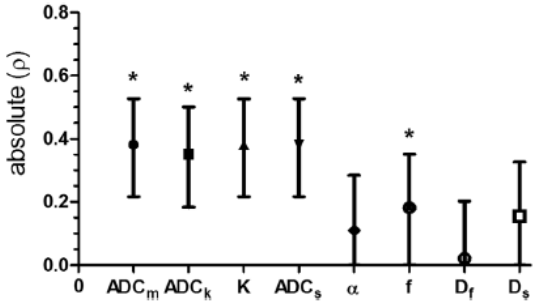

Figure 7.5: Spearman correlation ρ of DWI model parameters against Gleason score values of different aggressiveness levels in PCa.[9]

[8] Adapted with permission for academic use from "Mathematical models for diffusion-weighted imaging of prostate cancer using b values up to 2000 sec/mm^2: Correlation with Gleason score and repeatability of region of interest analysis", by Toivonen J., Merisaari H., Pesola M., Taimen P., Boström P.J., Pahikkala T., Aronen H.J., Jambor I., 2015. Magnetic Resonance in Medicine, 74(4), pp. 1116-1124. Copyright 2014 Wiley Periodicals, Inc.

[9] Adapted with permission for academic use from "Mathematical models for diffusion-weighted imaging of prostate cancer using b values up to 2000 sec/mm^2: Correlation with Gleason score and repeatability of region of interest analysis", by Toivonen J., Merisaari H., Pesola M., Taimen P., Boström P.J., Pahikkala T., Aronen H.J., Jambor I., 2015. Magnetic Resonance in Medicine, 74(4), pp. 1116-1124. Copyright 2014 Wiley Periodicals, Inc.

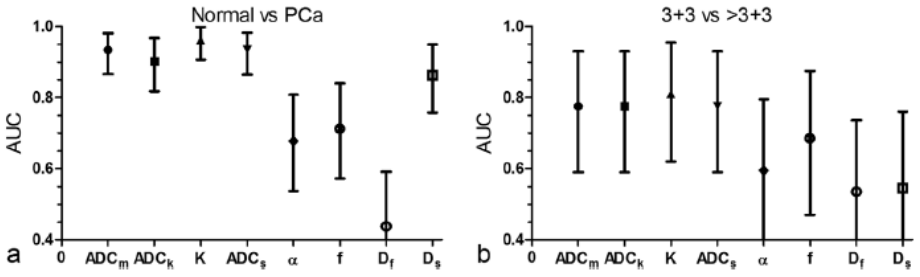

Figure 7.6: Classification capability of parameters of four DWI models. Classification between normal (Normal) and cancer tissue (PCa) is on the left (A), and between less aggressive tumours ('3+3') and more aggressive (> '3+3') is on the right.[10]

[10]Adapted with permission for academic use from "Mathematical models for diffusion-weighted imaging of prostate cancer using b values up to 2000 sec/mm^2: Correlation with Gleason score and repeatability of region of interest analysis", by Toivonen J., Merisaari H., Pesola M., Taimen P., Boström P.J., Pahikkala T., Aronen H.J., Jambor I., 2015. Magnetic Resonance in Medicine, 74(4), pp. 1116-1124. Copyright 2014 Wiley Periodicals, Inc.

Chapter 8

Discussion

Molecular imaging techniques are widely used for studying functions of human body *in vivo* in a non-invasive manner. In this thesis, we have addressed problems related to postprosessing the imaging data from PET and MRI. This facilitates to acquire information that would be otherwise lost due to noise or other artefacts. The results of the publications [P1]-[P6] are discussed in this chapter. In PET, low spatial resolution must be addressed with PVC, and [P1] compared conventional PVE correction methods for this, as expained in Chapter 8.1. For MRI, [P2] proposed a data-driven segmentation technique as an alternative approach to atlas-based techniques. This is discussed in Chapter 8.2. In DWI, the noise and the desire for shorter acquisition times are of major importance. This topic has been addressed in [P3]-[P6]. Chapter 8.3 discusses various DWI models together with b-value placement which is applied in the DWI data acquisition.

8.1 Comparison of Partial Volume Effect Correction Techniques for Brain PET (P1)

Our results shows that a quantitatively accurate PVC method may be sensitive to inherent noise and artefacts in PET images. A proper PVC method should therefore be chosen depending on the application, considering the distribution of the tracer in the target tissue, and placement and size of the ROI.

Since low spatial resolution is the major cause for PVE, the HRRT scanner produces the least amount of PVE to be corrected, while the other two scanners used in our study (GE Advance and GE DSTE) are more dependent on PVE correction (80% recovery rate without PVC in comparison to 61% and 65% in Table 1 [P1]). It should be also noted that the best performing A-PVC method also amplifies voxel-wise noise in the PET images (see SD values in Table1 [P1]). It outperforms other methods at ROI level,

but works weakly at voxel level. At voxel-wise spatial resolution level, the issue of PVC for quantification purposes still remains to be resolved.

Another aspect of PVC is that for the purpose of group comparison studies (e. g. between patients and controls), quantification in absolute terms may not be of the main concern, as long as the group differences are repeatable between acquisitions with the same scanner. For this, test-retest analysis provides important information about the repeatability of measurements. Whilst the use of [^{18}F]FDG tracer gives an even activity distribution, in [^{11}C]-raclopride BP studies the distribution is more concentrated to specific receptor sites. Therefore, the simplest (and most robust) PVC method [Me1990] emerges as the safest choice, giving a moderate increase in the binding potential of the SRTM model, while still improving $ICC(3,1)$ in all subcortical regions. This is seen in table 7.1 as the proportional increase of SD in ROI level is moderate (in comparison to other methods). It is to be noted that the method should not be picked with one option in mind, only. The recovery rate is the main motivation for the PV correction, and is therefore considered when choosing between doing or not doing the PV correction (i. e. between [Me1990] and 'No correction'). The presented results can easily be applied to other organs (i. e. in abdomen region), with the assumption that smoothing of the signal induced by the motion is small.

Since [P1] was published, more voxelwise methods have been proposed [Bo2008, Sh2009, Ki2008, Th2011, Wa2012, Co2013, Ir2016]. However, the observation about noise amplification in PVC has generally been made in the literature and it has been remarked, that the PVC should be applied with caution. Comparison of PVC techniques helps in making a decision about which technique to use with specific PET data. For PVC, the safest option is often the simplest, but the final decision depends on the exact application in question. When observing the repeatability of the extracted parameter estimates, more sophisticated methods may be more prone to errors as they are more sensitive to variations in the input image data. The same cautiousness should be used with the use os system matrix approach available with the newest present imaging devices.

8.2 Segmentation of Anatomical MR Images Having Low Signal-To-Noise Ratio (P2)

Segmentation of adult brain from T1 weighted MR images is a well established, although the three most commonly used methods (FAST, SPM5, SPM8) have some differences [Va2015]. Development of segmentation methods for newborn brain is a more complicated task, since the brain undergoes myelinization during early development.

As a result of myelination in normal brain maturation, water diffusion

in white matter reduces, which changes the intensity values in Gray and White Matters (see [Ba2000]). In T1 weighted images, the intensity of the White Matter changes from hypointense to hyperintense relative to the Gray matter intensity. In T2 weighted images, the change is from hyperintense to hypointense relative to the Gray Matter. State-of-art methods for adult brain (SPM5, SPM8, and lately SPM12) utilise *a priori* probability maps of brain structures that assist in the segmentation. The probability maps are developed with a combination of manual, semi-automatic and automatic procedures [Ma1995, Ma2001, Ku2011], while the preference here is in the automatic or semi-automatic methods because of their feasibility.

Segmentation of the brain of newborn infants has recently been applied by the means of a template that is adjusted according to the age of the patient [Ku2011]. Templates for small children have also been created [Ha2010, Ro2012]. However, their data is from small populations and they must be matched to the exact age of the subject, that is not a trivial task as there are variations in the development of the brain, and also the shapes vary more. A further problem for general applicability of spatial priors in segmentation is caused by the anomalies in brain structures; a general template is hard to map to this kind of MR images.

The strength of the data-driven approach in [P2] is that it does not make any assumptions about the topology of the analysed brain in contrast to the methods relying on spatial priors. The novel algorithm segments the joint area of GM and WM. The success with the quite challenging dataset, and other published data-driven methods make the data-driven approach an inviting alternative to consider when spatial prior approach is not applicable in neonatal MRI.

8.3 The Effect of Sample Points for DWI Modelling in Terms of Repeatability (P3 to P6)

Publications [P3-P6] address the repeatability of DWI measurements in the context of prostate imaging. Good repeatability of the DWI technique is essential for reliable diagnosis, such as detection and characterization of Prostate Cancer (PCa).

[P3]: *Optimization of b-value distribution for biexponential diffusion-weighted MR imaging of normal prostate.* This publication deals with the optimization of the b-value positioning in biexponential modelling of diffusion. While the evaluation was performed for one MRI scanner only, diffusion as a physical property is independent of the magnetic field strength [Ch2011]. The measured signal depends on multiple factors, not only on selection of b-values (e. g. pulse duration in Eq. (2.5)). Thus, the results in this study are not generally applicable to arbitrary pulse sequences. How-

ever, the results are generalizable to other scanning environments where the same physical property of diffusion is measured. The developed methodology can be applied to optimise protocols for other diffusion weighted MRI acquisition pulse sequences.

The main benefit of applying the 'clustered' approach in b-value placement was more visible in D_{slow} where $ICC(3,1)$ was higher. When comparing different DWI models, the biexponential model did not improve the $ICC(3,1)$. This was even expected because the simpler monoexponential model (ADC parameter) is more robust against noise in the diffusion decay curve. Even with lower reliability of the parameters, the biexponential model is still interesting due to its potential to obtain more clinically relevant information from the decay curve. It is therefore beneficial to study possibilities to improve the performance of the biexponential model even if the repeatability of its individual parameters would not exceed or would be even somewhat lower than that of ADC.

[P4]: *Evaluation of different mathematical models for diffusion-weighted imaging of normal prostate and prostate cancer using high b-values: A repeatability study.* The i.i.d. assumption of the fit residuals may be violated, making model comparison measures ($AICc$, F-ratio) not to work efficiently. In particular, the SNR generally decreases when the b-value is increased in diffusion weighted MRI. Thus, the model comparison was used to answer only to the question of how well the models explain the diffusion decay of the DWI data. To further understand which model is to be preferred, measurements for robustness against noise, and repeatability were also considered.

The biexponential model uses the greatest number of parameters and one can therefore expect that it would give the best fit to the data. However, in PCa patients, only slightly over half of the cases showed better fit with the biexponential model than with the kurtosis model. For this evaluation, the general interest was in the performance in *in vivo* data rather than in fits of individual curves.

The *in vivo* DWI data experiments consisted of 384 ROIs in healthy volunteers and 128 in PCa patients. Relating the simulations to the real image data, the parameters of the kurtosis models were observed to be robust against noise in the SNR range of the *in vivo* data, while all parameters of the biexponential data showed large deviation for the same noise levels (Fig. 3). This suggests that the noise is a smaller problem for the kurtosis model it is for the biexponential model when the SNR is similar to that in the ROI data of [P4]. This observation about the noise robustness of the kurtosis model is also indicated by the relatively high $ICC(3,1)$ values for the ADC_k and K parameters. Based on the above observations the use of the kurtosis model can be recommended; it fits better to the data than the monoexponential model and is robust when noise in the decay curve increases.

[P5]: *Optimization of the b-value distribution for four mathematical mod-*

els. Apart from the articles presented here, the $ICC(3,1)$ is currently a quite rarely used measure of the data quality, maybe due to the requirement for repeated examinations which are demanding to arrange. In [P5], the measurements of $ICC(3,1)$ suggest that studies using fewer than four b-values, (e. g. [Va2011, Ue2013, Ki2010, Ka2011, Ki2012]) could potentially benefit from an increased number of b-values. As in [P3], a generalization to other studies can be expected due to the same measured physiological quantity. However, it is stressed that the diffusion decay curve depends also on other parameters than the b-value. Another observation was that optimizing the placement of b-values (Fig. 1 (B) in [P5]) improves fittings, but quite surprisingly, this gives only a small improvement to the repeatability of the results, particularly with the commonly used monoexponential model. The placement of b-values contributed more to the repeatability in the more complex models where the parameters were in general more noisy. As a promising model that may give additional information to the conventional $ADCm$ parameter, the kurtosis model with parameter K has good robustness against noise, and it may thus give additional information for separating cancer from normal tissue in the prostate.

[P6]: *Correlating mathematical models with Gleason score and repeatability.* Repeatability of measurements is vital for diagnostic relevance. It was observed in [P6] that the most repeatable parameters were ADC_m, ADC_k, ADC_s and K in the kurtosis model. The regions of the CIs of $ICC(3,1)$ of these parameters were located notably higher than the CIs of the other parameters. In addition, they gave a superior classification accuracy. Publication [P6] concentrated on evaluations against the Gs measures from pathology. The analysis goes thus further than common studies where only goodness of fits or groups are compared, because it considers the clinical applicability with AUC as a measure for classification performance. According to observations in [P6], there is no good reason to prefer more complex models to monoexponential in conventional 3T MRI scanner. However, the general expectation is that a newer technology will produce higher SNR for the parameter estimates, allowing more meaningful information to be extracted from the DWI data with more complex DWI models.

To sum up, a general contribution of [P3-P6] is the observation that the placement of b-value distribution has an important role in DWI. This holds true in particularly for more complex DWI models. Another major contribution was to provide evaluations in terms of clinical usability of the DWI fitting parameters. These evaluations are crucial in the data analysis of images in medical context, because the clinical applicability finally determines the value and overall performance of the image analysis.

8.4 Author's Contribution

All the publications of this work are the result of a group effort. Particular collaboration was done with I. Jambor in [P3-P6] in designing and writing the manusripts. For the PV correction evaluation in PET [P1], the author analysed the data, implemented image processing methods, performed statistical analysis of data, and was the first writer of the manuscript. The author developed the data-driven brain MR segmentation technique, and was first writer in the corresponding manuscript [P2]. In DWI modelling articles [P3-P6] the author designed and implemented the modelling and following data analysis procedures, and had an important role in writing the corresponding manuscripts. Publication [P1] has been included in the thesis work of M. Teräs. Publications [P5] and [P6] are planned to be included in thesis works of I. Jambor and J. Toivonen, correspondingly.

Chapter 9

References

[Al2004] Alfano, B., Quarantelli, M., Comerci, M., Brunetti, A. and Salvatore, M., 2004. A new method for voxel-based partial volume effect correction. In Proceedings of the 10th meeting of the Organization for Human Brain Mapping, HBM Poster #TH360.

[Al2007] Alexander, A.L., Lee, J.E., Lazar, M. and Field, A.S., 2007. Diffusion tensor imaging of the brain. Neurotherapeutics, 4(3), pp. 316-329.

[Al2008] Alkhawaldeh, K., Bural, G., Kumar, R. and Alavi, A., 2008. Impact of dual-time-point 18F-FDG PET imaging and partial volume correction in the assessment of solitary pulmonary nodules. European Journal of Nuclear Medicine and Molecular Imaging, 35(2), pp. 246-252.

[Al2010] Alessio, A.M., Stearns, C.W., Tong, S., Ross, S.G., Kohlmyer, S., Ganin, A. and Kinahan, P.E., 2010. Application and evaluation of a measured spatially variant system model for PET image reconstruction. Medical Imaging, IEEE Transactions on, 29(3), pp. 938-949.

[An2008] Andersson, J.L., 2008. Maximum a posteriori estimation of diffusion tensor parameters using a Rician noise model: why, how and but. Neuroimage, 42(4), pp. 1340-1356.

[An2013] Andreou, A., Koh, D.M., Collins, D.J., Blackledge, M., Wallace, T., Leach, M.O. and Orton, M.R., 2013. Measurement reproducibility of perfusion fraction and pseudodiffusion coefficient derived by intravoxel incoherent motion diffusion-weighted MR imaging in normal liver and metastases. European Radiology, 23(2), pp. 428-434.

[Ar2010] Arlot, S. and Celisse, A., 2010. A survey of cross-validation procedures for model selection. Statistics Surveys, 4, pp. 40-79.

[AsFr2005] Ashburner, J. and Friston, K.J., 2005. Unified segmentation. Neuroimage, 26(3), pp. 839-851.

[Ba1988] Barkovich, A.J., Kjos, B.O., Jackson Jr, D.E. and Norman, D., 1988. Normal maturation of the neonatal and infant brain: MR imaging at 1.5 T. Radiology, 166(1), pp. 173-180.

[Ba2000] Barkovich, A.J., 2000. Concepts of myelin and myelination in neuroradiology. American Journal of Neuroradiology, 21(6), pp. 1099-1109.

[Ba2010] Barbee, D.L., Flynn, R.T., Holden, J.E., Nickles, R.J. and Jeraj, R., 2010. A method for partial volume correction of PET-imaged tumor heterogeneity using expectation maximization with a spatially varying point spread function. Physics in Medicine and Biology, 55(1), pp. 221-236.

[Be1998] Bertero, M. and Boccacci, P., 1998. Introduction to inverse problems in imaging. CRC Press.

[Be1999] Bertail, P., Politis, D.N. and Romano, J.P., 1999. On subsampling estimators with unknown rate of convergence. Journal of the American Statistical Association, 94(446), pp. 569-579.

[Be2004] Bennett, K.M., Hyde, J.S., Rand, S.D., Bennett, R., Krouwer, H.G., Rebro, K.J. and Schmainda, K.M., 2004. Intravoxel distribution of DWI decay rates reveals C6 glioma invasion in rat brain. Magnetic Resonance in Medicine, 52(5), pp. 994-1004.

[Bl1999] Bland, J.M. and Altman, D.G., 1999. Measuring agreement in method comparison studies. Statistical Methods in Medical Research, 8(2), pp. 135-160.

[Bo2006] Boussion, N., Hatt, M., Lamare, F., Bizais, Y., Turzo, A., Cheze-Le Rest, C. and Visvikis, D., 2006. A multiresolution image based approach for correction of partial volume effects in emission tomography. Physics in Medicine and Biology, 51(7), pp. 1857-1876.

[Bo2007] Boussion, N., Hatt, M., Reilhac, A. and Visvikis, D., 2007, Fully automated partial volume correction in PET based on a wavelet approach without the use of anatomical information. In Nuclear Science Symposium Conference Record, 4, pp. 2812-2816.

[Bo2008] Boussion, N., Hatt, M., Lamare, F., Le Rest, C.C. and Visvikis, D., 2008. Contrast enhancement in emission tomography by way of synergistic PET/CT image combination. Computer Methods and Programs in Biomedicine, 90(3), pp. 191-201.

[Bo2009] Boussion, N., Le Rest, C.C., Hatt, M. and Visvikis, D., 2009. Incorporation of wavelet-based denoising in iterative deconvolution for partial volume correction in whole-body PET imaging. European Journal of Nuclear Medicine and Molecular Imaging, 36(7), pp. 1064-1075.

[Bo2010] Bourne, R., 2010. Fundamentals of digital imaging in medicine. Springer Science & Business Media, p. 39.

[Bo2014] Boivin, G., Genoud, V. and Zaidi, H., 2014. MRI-guided partial volume correction in brain PET imaging: Comparison of five algorithms. Frontiers in Biomedical Technologies [2345-5829], 1(2), pp. 73-81.

[Bo2014b] Bourne, R.M., Panagiotaki, E., Bongers, A., Sved, P., Watson, G. and Alexander, D.C., 2014. Information theoretic ranking of four models of diffusion attenuation in fresh and fixed prostate tissue ex vivo. Magnetic Resonance in Medicine, 72(5), pp. 1418-1426.

[BoWr2000] Bonett, D.G. and Wright, T.A., 2000. Sample size requirements for estimating Pearson, Kendall and Spearman correlations. Psychometrika, 65(1), pp. 23-28.

[Br2006] Brown, C.D. and Davis, H.T., 2006. Receiver operating characteristics curves and related decision measures: A tutorial. Chemometrics and Intelligent Laboratory Systems, 80(1), pp. 24-38.

[Bu2016] Buvat, I., 2016. Using simulations of the detector performance for enhanced image reconstruction in molecular imaging. Nuclear Instruments and Methods in Physics Research Section A: Accelerators, Spectrometers, Detectors and Associated Equipment, 809, pp. 89-95.

[BuAn2004] Burnham, K.P. and Anderson, D.R., 2004. Multimodel inference understanding AIC and BIC in model selection. Sociological Methods & Research, 33(2), pp. 267-275.

[ByScSc1987] Byrd, R.H., Schnabel, R.B. and Shultz, G.A., 1987. A trust region algorithm for nonlinearly constrained optimization. SIAM Journal on Numerical Analysis, 24(5), pp. 1152-1170.

[Ca2004] Castellano, G., Bonilha, L., Li, L.M. and Cendes, F., 2004. Texture analysis of medical images. Clinical Radiology, 59(12), pp. 1061-1069.

[Ca2011] Cabezas, M., Oliver, A., Lladó, X., Freixenet, J. and Cuadra, M.B., 2011. A review of atlas-based segmentation for magnetic resonance brain images. Computer Methods and Programs in Biomedicine, 104(3), pp. e158-e177.

[Ca2011b] Catto, J.W.F., Robinson, M.C., Albertsen, P.C., Goepel, J.R., Abbod, M.F., Linkens, D.A., Davis, M., Rosario, D.J., Warren, A.Y., Varma, M. and Griffiths, D.F., 2011. Suitability of PSA-detected localised prostate cancers for focal therapy: experience from the ProtecT study. British Journal of Cancer, 105(7), pp. 931-937.

[Ca2012] Cameron, A., Glaister, J., Wong, A. and Haider, M.A., 2012, August. Non-parametric Bayesian estimation of apparent diffusion coefficient from diffusion-weighted magnetic resonance imaging data. In Engineering in Medicine and Biology Society (EMBC), 2012 Annual International Conference of the IEEE. pp. 412-415.

[Ch2011] Chenevert, T.L., Galbán, C.J., Ivancevic, M.K., Rohrer, S.E., Londy, F.J., Kwee, T.C., Meyer, C.R., Johnson, T.D., Rehemtulla, A. and Ross, B.D., 2011. Diffusion coefficient measurement using a temperature-controlled fluid for quality control in multicenter studies. Journal of Magnetic Resonance Imaging, 34(4), pp. 983-987.

[Ch2013] Cheng, N.M., Fang, Y.H.D. and Yen, T.C., 2013. The promise and limits of PET texture analysis. Annals of Nuclear Medicine, 27(9), pp. 867-869.

[Ch2015] Cho, G.Y., Moy, L., Zhang, J.L., Baete, S., Lattanzi, R., Moccaldi, M., Babb, J.S., Kim, S., Sodickson, D.K. and Sigmund, E.E., 2015. Comparison of fitting methods and b-value sampling strategies for intravoxel incoherent motion in breast cancer. Magnetic Resonance in Medicine, 74(4), pp. 1077-1085.

[Cl2010] Cloquet, C., Sureau, F.C., Defrise, M., Van Simaeys, G., Trotta, N. and Goldman, S., 2010. Non-Gaussian space-variant resolution modelling for list-mode reconstruction. Physics in Medicine and Biology, 55, pp. 5045-5066.

[Co2000] Courchesne, E., Chisum, H.J., Townsend, J., Cowles, A., Covington, J., Egaas, B., Harwood, M., Hinds, S. and Press, G.A., 2000. Normal brain development and aging: quantitative analysis at in vivo MR imaging in healthy volunteers 1. Radiology, 216(3), pp. 672-682.

[Co2013] Coello, C., Willoch, F., Selnes, P., Gjerstad, L., Fladby, T. and Skretting, A., 2013. Correction of partial volume effect in 18 F-FDG PET brain studies using coregistered MR volumes: Voxel based analysis of tracer uptake in the white matter. Neuroimage, 72, pp. 183-192.

[Co2015] Cohen, A.D., Schieke, M.C., Hohenwalter, M.D. and Schmainda, K.M., 2015. The effect of low b-values on the intravoxel incoherent motion derived pseudodiffusion parameter in liver. Magnetic Resonance in Medicine, 73(1), pp. 306-311.

[De1988] DeLong, E.R., DeLong, D.M. and Clarke-Pearson, D.L., 1988. Comparing the areas under two or more correlated receiver operating characteristic curves: a nonparametric approach. Biometrics, pp. 837-845.

[De2007] Deans, S.R., 2007. The Radon transform and some of its applications, Dover Publications, Inc., Mineola, New York.

[De2014] Dell'Acqua, P., Donatelli, M. and Estatico, C., 2014. Preconditioners for image restoration by reblurring techniques. Journal of Computational and Applied Mathematics, 272, pp. 313-333.

[De2015] Devi, C.N., Chandrasekharan, A., Sundararaman, V.K. and Alex, Z.C., 2015. Neonatal brain MRI segmentation: A review. Computers in Biology and Medicine, 64, pp. 163-178.

[Dh2003] Dhawan A.P., 2003. 'Medical Imaging and Image Formation', in: Medical Image Analysis, John Wiley & Sons, Hoboken, New Jersey. pp. 154-155.

[Di2007] Dietrich, O., Raya, J.G., Reeder, S.B., Reiser, M.F. and Schoenberg, S.O., 2007. Measurement of signal-to-noise ratios in MR images: Influence of multichannel coils, parallel imaging, and reconstruction filters. Journal of Magnetic Resonance Imaging, 26(2), pp. 375-385.

[Di2014] Dikaios, N., Punwani, S., Hamy, V., Purpura, P., Rice, S., Forster, M., Mendes, R., Taylor, S. and Atkinson, D., 2014. Noise estimation from averaged diffusion weighted images: Can unbiased quantitative decay parameters assist cancer evaluation?. Magnetic Resonance in Medicine, 71(6), pp. 2105-2117.

[Dj2001] Djavan, B.O.B., Ravery, V., Zlotta, A., Dobronski, P., Dobrovits, M., Fakhari, M., Seitz, C., Susani, M., Borkowski, A., Boccon-Gibod, L. and Schulman, C.C., 2001. Prospective evaluation of prostate cancer detected on biopsies 1, 2, 3 and 4: when should we stop?. The Journal of Urology, 166(5), pp. 1679-1683.

[DoAl1969] Dorfman, D.D. and Alf, E., 1969. Maximum-likelihood estimation of parameters of signal-detection theory and determination of confidence intervals-rating-method data. Journal of Mathematical Psychology, 6(3), pp. 487-496.

[Dy2014] Dyvorne, H., Jajamovich, G., Kakite, S., Kuehn, B. and Taouli, B., 2014. Intravoxel incoherent motion diffusion imaging of the liver: optimal b-value subsampling and impact on parameter precision and reproducibility. European Journal of Radiology, 83(12), pp. 2109-2113.

[Dö2011] Döpfert, J., Lemke, A., Weidner, A. and Schad, L.R., 2011. Investigation of prostate cancer using diffusion-weighted intravoxel incoherent motion imaging. Magnetic Resonance Imaging, 29(8), pp. 1053-1058.

[Ef1979] Efron, B., 1979. Bootstrap methods: another look at the jackknife. The Annals of Statistics, pp. 1-26.

[Ep2005] Epstein, J.I., Allsbrook Jr, W.C., Amin, M.B., Egevad, L.L. and ISUP Grading Committee, 2005. The 2005 International Society of Urological Pathology (ISUP) consensus conference on Gleason grading of prostatic carcinoma. The American Journal of Surgical Pathology, 29(9), pp. 1228-1242.

[Er2012] Erlandsson, K., Buvat, I., Pretorius, P.H., Thomas, B.A. and Hutton, B.F., 2012. A review of partial volume correction techniques for emission tomography and their applications in neurology, cardiology and oncology. Physics in Medicine and Biology, 57(21), pp. R119-R159.

[Eu2009] Eudralex, 2009, EU GMP Volume 4, Good manufacturing practice (GMP), viewed 2nd July 2015, http://ec.europa.eu.

[Fi1921] Fisher R.A., 1921. On the 'Probable Error' of a Coefficient of Correlation Deduced from a Small Sample, Metron, 1, pp. 3-32.

[FlGo2009] Floudas, C.A. and Gounaris, C.E., 2009. A review of recent advances in global optimization. Journal of Global Optimization, 45(1), pp. 3-38.

[Fu2003] Fujii, Y. and Nakada, T., 2003. Cortical reorganization in patients with subcortical hemiparesis: neural mechanisms of functional recovery and prognostic implication. Journal of Neurosurgery, 98(1), pp. 64-73.

[Ge2001] Gerig, G., Styner, M., Jones, D., Weinberger, D. and Lieberman, J., 2001. Shape analysis of brain ventricles using SPHARM. In IEEE Workshop on Mathematical Methods in Biomedical Image Analysis, pp. 171-178.

[Gi2011] Giles, S.L., Morgan, V.A., Riches, S.F., Thomas, K., Parker, C. and deSouza, N.M., 2011. Apparent diffusion coefficient as a predictive biomarker of prostate cancer progression: value of fast and slow diffusion components. American Journal of Roentgenology, 196(3), pp. 586-591.

[Gi2016] Gillam, J.E. and Rafecas, M., 2016. Monte-Carlo simulations and image reconstruction for novel imaging scenarios in emission tomography. Nuclear Instruments and Methods in Physics Research Section A: Accelerators, Spectrometers, Detectors and Associated Equipment, 809, pp. 76-88.

[GiMuWr1981] Gill, P.R., Murray, W. and Wright, M.H., 1981. The levenberg-marquardt method. Practical Optimization, pp. 136-137.

[Gl2007] Glatting, G., Kletting, P., Reske, S.N., Hohl, K. and Ring, C., 2007. Choosing the optimal fit function: comparison of the Akaike information criterion and the F-test. Medical Physics, 34(11), pp. 4285-4292.

[Go1986] Goodenough, D.J., Weaver, K.E., Costaridou, H., Eerdmans, H. and Huysmans, P., 1986. A new software correction approach to volume averaging artifacts in CT. Computerized Radiology, 10(2), pp. 87-98.

[Gr2005] Graham, R.N.J., Perriss, R.W. and Scarsbrook, A.F., 2005. DICOM demystified: a review of digital file formats and their use in radiological practice. Clinical Radiology, 60(11), pp. 1133-1140.

[Gr2013] Graf, M., Simon, D., Lemke, A., Grünberg, K. and Mang, S., 2013. Toward a non-invasive screening tool for differentiation of pancreatic lesions based on intra-voxel incoherent motion derived parameters. Zeitschrift für Medizinische Physik, 23(1), pp. 46-55.

[Gu2011] Gui, L., Lisowski, R., Faundez, T., Hüppi, P.S., Lazeyras, F. and Kocher, M., 2011, March. Automatic segmentation of newborn brain MRI using mathematical morphology. In Biomedical Imaging: From Nano to Macro, 2011 IEEE International Symposium on, pp. 2026-2030.

[GuLi2012] Gunturk, B.K. and Li, X. (eds.), 2012. Image restoration: Fundamentals and advances, CRC Press, Boca Raton, Florida.

[GuPa1995] Gudbjartsson, H. and Patz, S., 1995. The Rician distribution of noisy MRI data. Magnetic Resonance in Medicine, 34(6), pp. 910-914.

[Ha1991] Hayakawa, K., Konishi, Y., Kuriyama, M., Konishi, K. and Matsuda, T., 1991. Normal brain maturation in MRI. European Journal of Radiology, 12(3), pp. 208-215.

[Ha2006] Hagmann, P., Jonasson, L., Maeder, P., Thiran, J.P., Wedeen, V.J. and Meuli, R., 2006. Understanding Diffusion MR Imaging Techniques: From Scalar Diffusion-weighted Imaging to Diffusion Tensor Imaging and Beyond 1. Radiographics, 26(suppl_1), pp. S205-S223.

[Ha2007] Haas, G.P., Delongchamps, N.B., Jones, R.F., Chandan, V., Serio, A.M., Vickers, A.J., Jumbelic, M., Threatte, G., Korets, R., Lilja, H. and de la Roza, G., 2007. Needle biopsies on autopsy prostates: sensitivity of cancer detection based on true prevalence. Journal of the National Cancer Institute, 99(19), pp. 1484-1489.

[Ha2010] Habas, P.A., Kim, K., Corbett-Detig, J.M., Rousseau, F., Glenn, O.A., Barkovich, A.J. and Studholme, C., 2010. A spatiotemporal atlas of MR intensity, tissue probability and shape of the fetal brain with application to segmentation. Neuroimage, 53(2), pp. 460-470.

[Ha2011] Hambrock, T., Somford, D.M., Huisman, H.J., van Oort, I.M., Witjes, J.A., Hulsbergen-van de Kaa, C.A., Scheenen, T. and Barentsz, J.O., 2011. Relationship between apparent diffusion coefficients at 3.0-T MR imaging and Gleason grade in peripheral zone prostate cancer. Radiology, 259(2), pp. 453-461.

[HaMc1983] Hanley, J.A. and McNeil, B.J., 1983. A method of comparing the areas under receiver operating characteristic curves derived from the same cases. Radiology, 148(3), pp. 839-843.

[He2013] Heusch, P., Wittsack, H.J., Pentang, G. Buchbender, C., Miese, F., Schek, J., Kröpil, P., Antoch, G., Lanzman, R.S., 2013. Biexponential analysis of diffusion-weighted imaging: comparison of three different calculation methods in transplanted kidneys. Acta Radiologica, 54(10), pp. 1210-1217.

[Ho1982] Hoffman, E.J., Huang, S.C., Plummer, D. and Phelps, M.E., 1982. quantification in positron emission computed tomography: 6. effect of nonuniform resolution. Journal of Computer Assisted Tomography, 6(5), pp. 987-999.

[Ho2010] Hoetjes, N.J., van Velden, F.H., Hoekstra, O.S., Hoekstra, C.J., Krak, N.C., Lammertsma, A.A. and Boellaard, R., 2010. Partial volume correction strategies for quantitative FDG PET in oncology. European Journal of Nuclear Medicine and Molecular Imaging, 37(9), pp. 1679-1687.

[HuLa1994] Hudson, H.M. and Larkin, R.S., 1994. Accelerated image reconstruction using ordered subsets of projection data. Medical Imaging, IEEE Transactions on, 13(4), pp. 601-609.

[HuTs1989] Hurvich, C.M. and Tsai, C.L., 1989. Regression and time series model selection in small samples. Biometrika, 76(2), pp. 297-307.

[Hu2007] Hu, Z., Wang, W., Gualtieri, E.E., Hsieh, Y.L., Karp, J.S., Matej, S., Parma, M.J., Tung, C.H., Walsh, E.S., Werner, M. and Gagnon, D., 2007, October. An LOR-based fully-3D PET image reconstruction using a blob-basis function. In Nuclear Science Symposium Conference Record NSS'07 IEEE, 6, pp. 4415-4418.

[Hü1998] Hüppi, P.S., Warfield, S., Kikinis, R., Barnes, P.D., Zientara, G.P., Jolesz, F.A., Tsuji, M.K. and Volpe, J.J., 1998. Quantitative magnetic resonance imaging of brain development in premature and mature newborns. Annals of Neurology, 43(2), pp. 224-235.

[Ii1991] Iida, H., Rhodes, C.G., de Silva, R., Yamamoto, Y., Araujo, L.I., Maseri, A. and Jones, T., 1991. Myocardial tissue fraction–correction for partial volume effects and measure of tissue viability. Journal of nuclear medicine: official publication, Society of Nuclear Medicine, 32(11), pp. 2169-2175.

[In1999] Inder, T.E., Huppi, P.S., Warfield, S., Kikinis, R., Zientara, G.P., Barnes, P.D., Jolesz, F. and Volpe, J.J., 1999. Periventricular white matter injury in the premature infant is followed by reduced cerebral cortical gray matter volume at term. Annals of Neurology, 46(5), pp. 755-760.

[Ir2016] Iriarte, A., Marabini, R., Matej, S., Sorzano, C.O.S. and Lewitt, R.M., 2016. System models for PET statistical iterative reconstruction: A review. Computerized Medical Imaging and Graphics, 48, pp. 30-48.

[Ja1970] Jansson, P.A., Hunt, R.H. and Plyler, E.K., 1970. Resolution enhancement of spectra. Journal of the Optical Society of America, 60(5), pp. 596-599.

[Ja2004] Jan, S., Santin, G., Strul, D., Staelens, S., Assie, K., Autret, D., Avner, S., Barbier, R., Bardies, M., Bloomfield, P.M. and Brasse, D., 2004. GATE: a simulation toolkit for PET and SPECT. Physics in Medicine and Biology, 49(19), pp. 4543-4561.

[Je2005] Jensen, J.H., Helpern, J.A., Ramani, A., Lu, H. and Kaczynski, K., 2005. Diffusional kurtosis imaging: The quantification of non-gaussian water diffusion by means of magnetic resonance imaging. Magnetic Resonance in Medicine, 53(6), pp. 1432-1440.

[Jo2007] de Jong, H.W., van Velden, F.H., Kloet, R.W., Buijs, F.L., Boellaard, R. and Lammertsma, A.A., 2007. Performance evaluation of the ECAT HRRT: an LSO-LYSO double layer high resolution, high sensitivity scanner. Physics in Medicine and Biology, 52(5), pp. 1505-1526.

[Ka2011] Katahira, K., Takahara, T., Kwee, T.C., Oda, S., Suzuki, Y., Morishita, S., Kitani, K., Hamada, Y., Kitaoka, M. and Yamashita, Y., 2011. Ultra-high-b-value diffusion-weighted MR imaging for the detection of prostate cancer: evaluation in 201 cases with histopathological correlation. European Radiology, 21(1), pp. 188-196.

[Ke2008] Kellman, P., Chefd'hotel, C., Lorenz, C.H., Mancini, C., Arai, A.E. and McVeigh, E.R., 2008. Fully automatic, retrospective enhancement of real-time acquired cardiac cine MR images using image-based navigators and respiratory motion-corrected averaging. Magnetic Resonance in Medicine, 59(4), pp. 771-778

[Ki2007] Kiselev, V.G. and Il'yasov, K.A., 2007. Is the "biexponential diffusion" biexponential?. Magnetic Resonance in Medicine, 57(3), pp. 464-469.

[Ki2008] Kirov, A.S., Piao, J.Z. and Schmidtlein, C.R., 2008. Partial volume effect correction in PET using regularized iterative deconvolution with variance control based on local topology. Physics in Medicine and Biology, 53(10), pp. 2577-2591.

[Ki2010] Kim, C.K., Park, B.K. and Kim, B., 2010. High-b-value diffusion-weighted imaging at 3 T to detect prostate cancer: comparisons between b values of 1,000 and 2,000sec/mm^2. American Journal of Roentgenology, 194(1), pp. W33-W37.

[Ki2012] Kitajima, K., Takahashi, S., Ueno, Y., Yoshikawa, T., Ohno, Y., Obara, M., Miyake, H., Fujisawa, M. and Sugimura, K., 2012. Clinical utility of apparent diffusion coefficient values obtained using high b-value when diagnosing prostate cancer using 3 tesla MRI: Comparison between ultra-high b-value (2000sec/mm^2) and standard high b-value (1000sec/mm^2). Journal of Magnetic Resonance Imaging, 36(1), pp. 198-205.

[Ki2012b] Kim, S., Decarlo, L., Cho, G.Y., Jensen, J.H., Sodickson, D.K., Moy, L., Formenti, S., Schneider, R.J., Goldberg, J.D. and Sigmund, E.E., 2012. Interstitial fluid pressure correlates with intravoxel incoherent motion imaging metrics in a mouse mammary carcinoma model. NMR in Biomedicine, 25(5), pp. 787-794.

[Ko2009] Koh, D.M., Blackledge, M., Collins, D.J., Padhani, A.R., Wallace, T., Wilton, B., Taylor, N.J., Stirling, J.J., Sinha, R., Walicke, P. and Leach, M.O., 2009. Reproducibility and changes in the apparent diffusion coefficients of solid tumours treated with combretastatin A4 phosphate and bevacizumab in a two-centre phase I clinical trial. European Radiology, 19(11), pp. 2728-2738.

[Ko2010] Koh, D.M. and Thoeny, H.C. eds., 2010. Diffusion-Weighted MR imaging: applications in the body. Springer Science & Business Media.

[Ko2014] Kottas, M., Kuss, O. and Zapf, A., 2014. A modified Wald interval for the area under the ROC curve (AUC) in diagnostic case-control studies. BMC Medical Research Methodology, 14(1), p. 26.

[Kr2012] Kristoffersen, A., 2012. Estimating non-gaussian diffusion model parameters in the presence of physiological noise and rician signal bias. Journal of Magnetic Resonance Imaging, 35(1), pp. 181-189.

[Ku2011] Kuklisova-Murgasova, M., Aljabar, P., Srinivasan, L., Counsell, S.J., Doria, V., Serag, A., Gousias, I.S., Boardman, J.P., Rutherford, M.A., Edwards, A.D. and Hajnal, J.V., 2011. A dynamic 4D probabilistic atlas of the developing brain. NeuroImage, 54(4), pp. 2750-2763.

[Ku2014] Kurugol, S., Freiman, M., Afacan, O., Perez-Rossello, J.M., Callahan, M.J. and Warfield, S.K., 2014. Spatially-constrained probability distribution model of incoherent motion (SPIM) in diffusion weighted MRI signals of crohn's disease. In Abdominal Imaging. Computational and Clinical Applications (pp. 117-127). Springer International Publishing.

[La1951] Landweber, L., 1951. An iteration formula for Fredholm integral equations of the first kind. American Journal of Mathematics, pp. 615-624.

[La2009] Lange, D., Zappavigna, C., Hamidizadeh, R., Goldenberg, S.L., Paterson, R.F. and Chew, B.H., 2009. Bacterial sepsis after prostate biopsy - a new perspective. Urology, 74(6), pp. 1200-1205.

[La2010] Langer, D.L., van der Kwast, T.H., Evans, A.J., Plotkin, A., Trachtenberg, J., Wilson, B.C. and Haider, M.A., 2010. Prostate tissue composition and MR measurements: investigating the relationships between ADC, T2, K trans, ve, and corresponding histologic features 1. Radiology, 255(2), pp. 485-494.

[LaHu1997] Lammertsma, A.A. and Hume, S.P., 1996. Simplified reference tissue model for PET receptor studies. Neuroimage, 4(3), pp. 153-158.

[Le1986] Le Bihan, D., Breton, E., Lallemand, D., Grenier, P., Cabanis, E. and Laval-Jeantet, M., 1986. MR imaging of intravoxel incoherent motions: application to diffusion and perfusion in neurologic disorders. Radiology, 161(2), pp. 401-407.

[Le1988] Le Bihan, D., Breton, E., Lallemand, D., Aubin, M.L., Vignaud, J. and Laval-Jeantet, M., 1988. Separation of diffusion and perfusion in intravoxel incoherent motion MR imaging. Radiology, 168(2), pp. 497-505.

[Le2006] Lee, I., Pappas, G.J., Cleaveland, R., Hatcliff, J., Krogh, B.H., Lee, P., Rubin, H. and Sha, L., 2006. High-confidence medical device software and systems. Computer, 39(4), pp. 33-38.

[Le2009] Lemaitre, L., Puech, P., Poncelet, E., Bouyé, S., Leroy, X., Biserte, J. and Villers, A., 2009. Dynamic contrast-enhanced MRI of anterior prostate cancer: morphometric assessment and correlation with radical prostatectomy findings. European Radiology, 19(2), pp. 470-480.

[Le2009b] Lemke, A., Laun, F.B., Klau, M., Re, T.J., Simon, D., Delorme, S., Schad, L.R. and Stieltjes, B., 2009. Differentiation of pancreas carcinoma from healthy pancreatic tissue using multiple b-values: comparison of apparent diffusion coefficient and intravoxel incoherent motion derived parameters. Investigative Radiology, 44(12), pp. 769-775.

[Le2011] Lemke, A., Stieltjes, B., Schad, L.R. and Laun, F.B., 2011. Toward an optimal distribution of b values for intravoxel incoherent motion imaging. Magnetic Resonance Imaging, 29(6), pp. 766-776.

[Le2014] Lee, H.J., Rha, S.Y., Chung, Y.E., Shim, H.S., Kim, Y.J., Hur, J., Hong, Y.J. and Choi, B.W., 2014. Tumor perfusion-related parameter of diffusion-weighted magnetic resonance imaging: Correlation with histological microvessel density. Magnetic Resonance in Medicine, 71(4), pp. 1554-1558.

[Lo2014] Lougovski, A., Hofheinz, F., Maus, J., Schramm, G., Will, E. and van den Hoff, J., 2014. A volume of intersection approach for on-the-fly system matrix calculation in 3D PET image reconstruction. Physics in Medicine and Biology, 59(3), pp. 561-577.

[Lo2015] Looney, S.W. and Hagan, J.L., 2015. Analysis of Biomarker Data: A Practical Guide, John Wiley & Sons, Hoboken, New Jersey.

[Lo2015] Loktyushin, A., Nickisch, H., Pohmann, R. and Schölkopf, B., 2015. Blind multirigid retrospective motion correction of MR images. Magnetic Resonance in Medicine, 73(4), pp. 1457-1468.

[Lu1974] Lucy, L.B., 1974. An iterative technique for the rectification of observed distributions. The Astronomical Journal, 79, pp. 745-754.

[Lu2008] Luciani, A., Vignaud, A., Cavet, M., Tran Van Nhieu, J., Mallat, A., Ruel, L., Laurent, A., Deux, J.F., Brugieres, P. and Rahmouni, A., 2008. Liver cirrhosis: intravoxel incoherent motion MR imaging - Pilot study 1. Radiology, 249(3), pp. 891-899.

[Ma1995] Mazziotta, J.C., Toga, A.W., Evans, A., Fox, P. and Lancaster, J., 1995. A probabilistic atlas of the human brain: theory and rationale for its development the international consortium for brain mapping (ICBM). Neuroimage, 2(2PA), pp. 89-101.

[Ma1996] Matej, S. and Browne, J.A., 1996. Performance of a fast maximum likelihood algorithm for fully 3D PET reconstruction. In Three-Dimensional Image Reconstruction in Radiology and Nuclear Medicine (pp. 297-315). Springer Netherlands.

[Ma2001] Mazziotta, J., Toga, A., Evans, A., Fox, P., Lancaster, J., Zilles, K., Woods, R., Paus, T., Simpson, G., Pike, B. and Holmes, C., 2001. A probabilistic atlas and reference system for the human brain: International Consortium for Brain Mapping (ICBM). Philosophical Transactions of the Royal Society B: Biological Sciences, 356(1412), pp. 1293-1322.

[Ma2012] Mazaheri, Y., Vargas, H.A., Akin, O., Goldman, D.A. and Hricak, H., 2012. Reducing the influence of b-value selection on diffusion-weighted imaging of the prostate: Evaluation of a revised monoexponential model within a clinical setting. Journal of Magnetic Resonance Imaging, 35(3), pp. 660-668.

[Ma2012b] Mazaheri, Y., Afaq, A., Rowe, D.B., Lu, Y., Shukla-Dave, A. and Grover, J., 2012. Diffusion-weighted magnetic resonance imaging of the prostate: improved robustness with stretched exponential modeling. Journal of Computer Assisted Tomography, 36(6), pp. 695-703.

[Ma2013] Maas, M.C., Fütterer, J.J. and Scheenen, T.W., 2013. Quantitative evaluation of computed high B value diffusion-weighted magnetic resonance imaging of the prostate. Investigative Radiology, 48(11), pp. 779-786.

[Ma2013b] Marzi, S., Piludu, F. and Vidiri, A., 2013. Assessment of diffusion parameters by intravoxel incoherent motion MRI in head and neck squamous cell carcinoma. NMR in Biomedicine, 26(12), pp. 1806-1814.

[MaCr2005] Macmillan, N.A. and Creelman, C.D., 2004. Detection theory: A user's guide, 2nd ed., Psychology Press, Mahwah, New Jersey.

[Me1990] Meltzer, C.C., Leal, J.P., Mayberg, H.S., Wagner Jr, H.N. and Frost, J.J., 1990. Correction of PET data for partial volume effects in human cerebral cortex by MR imaging. Journal of Computer Assisted Tomography, 14(4), pp. 561-570.

[Me1999] Meltzer, C.C., Kinahan, P.E., Greer, P.J., Nichols, T.E., Comtat, C., Cantwell, M.N., Lin, M.P. and Price, J.C., 1999. Comparative evaluation of MR-based partial-volume correction schemes for PET. Journal of Nuclear Medicine, 40(12), pp. 2053-2065.

[Me2006] Metz, C.E., 2006. Receiver operating characteristic analysis: a tool for the quantitative evaluation of observer performance and imaging systems. Journal of the American College of Radiology, 3(6), pp. 413-422.

[Mo1990] Moseley, M.E., Cohen, Y., Mintorovitch, J., Chileuitt, L., Shimizu, H., Kucharczyk, J., Wendland, M.F. and Weinstein, P.R., 1990. Early detection of regional cerebral ischemia in cats: comparison of diffusion-and T2-weighted MRI and spectroscopy. Magnetic Resonance in Medicine, 14(2), pp. 330-346.

[Mo2010] Monaco, J.P., Tomaszewski, J.E., Feldman, M.D., Hagemann, I., Moradi, M., Mousavi, P., Boag, A., Davidson, C., Abolmaesumi, P. and Madabhushi, A., 2010. High-throughput detection of prostate cancer in histological sections using probabilistic pairwise Markov models. Medical Image Analysis, 14(4), pp. 617-629.

[Mu2006] Muzic Jr, R.F. and Christian, B.T., 2006. Evaluation of objective functions for estimation of kinetic parameters. Medical Physics, 33(2), pp. 342-353.

[Mu2006b] Mulkern, R.V., Barnes, A.S., Haker, S.J., Hung, Y.P., Rybicki, F.J., Maier, S.E. and Tempany, C.M., 2006. Biexponential characterization of prostate tissue water diffusion decay curves over an extended b-factor range. Magnetic Resonance Imaging, 24(5), pp. 563-568.

[Mü1992] Müller-Gartner, H.W., Links, J.M., Prince, J.L., Bryan, R.N., McVeigh, E., Leal, J.P., Davatzikos, C. and Frost, J.J., 1992. Measurement of radiotracer concentration in brain gray matter using positron emission tomography: MRI-based correction for partial volume effects. Journal of Cerebral Blood Flow and Metabolism, 12(4), pp. 571-583.

[Na2006] El Naqa, I., Low, D.A., Bradley, J.D., Vicic, M. and Deasy, J.O., 2006. Deblurring of breathing motion artifacts in thoracic PET images by deconvolution methods. Medical Physics, 33(10), pp. 3587-3600.

[Na2011] National Electrical Manufacturers Association (NEMA): Digital Imaging and Communications in Medicine (DICOM) - Part 2: Conformance, 2011. Rosslyn, VA.

[Ne2003] Nehmeh, S.A., Erdi, Y.E., Rosenzweig, K.E., Schoder, H., Larson, S.M., Squire, O.D. and Humm, J.L., 2003. Reduction of respiratory motion artifacts in PET imaging of lung cancer by respiratory correlated dynamic PET: methodology and comparison with respiratory gated PET. Journal of Nuclear Medicine, 44(10), pp. 1644-1648.

[NeMe1965] Nelder, J.A. and Mead, R., 1965. A simplex method for function minimization. The Computer Journal, 7(4), pp. 308-313.

[Ob1998] Obuchowski, N.A. and Lieber, M.L., 1998. Confidence intervals for the receiver operating characteristic area in studies with small samples. Academic Radiology, 5(8), pp. 561-571.

[OlGo1996] Ollinger, J.M. and Goggin, A.S., 1996, November. Maximum likelihood reconstruction in fully 3D PET via the SAGE algorithm. In Nuclear Science Symposium, 1996. Conference Record., pp. 1594-1598.

[Or2014] Orton, M.R., Collins, D.J., Koh, D.M. and Leach, M.O., 2014. Improved intravoxel incoherent motion analysis of diffusion weighted imaging by data driven Bayesian modeling. Magnetic Resonance in Medicine, 71(1), pp. 411-420.

[Pa2006] Panin, V.Y., Kehren, F., Michel, C. and Casey, M., 2006. Fully 3-D PET reconstruction with system matrix derived from point source measurements. Medical Imaging, IEEE Transactions on, 25(7), pp. 907-921.

[Pa2007] Pantin E., Starck J., Murtagh F., 2007. Blind Image Deconvolution: Theory and Applications, in: Campisi, P. and Egiazarian, K. (eds.), Blind image deconvolution: theory and applications, CRC press, Boca Raton, Florida.

[Pa2013] Pang, Y., Turkbey, B., Bernardo, M., Kruecker, J., Kadoury, S., Merino, M.J., Wood, B.J., Pinto, P.A. and Choyke, P.L., 2013. Intravoxel incoherent motion MR imaging for prostate cancer: An evaluation of perfusion fraction and diffusion coefficient derived from different b-value combinations. Magnetic Resonance in Medicine, 69(2), pp. 553-562.

[Pa2015] Panagiotaki, E., Chan, R.W., Dikaios, N., Ahmed, H.U., OŠ-Callaghan, J., Freeman, A., Atkinson, D., Punwani, S., Hawkes, D.J. and Alexander, D.C., 2015. Microstructural characterization of normal and malignant human prostate tissue with vascular, extracellular, and restricted diffusion for cytometry in tumours magnetic resonance imaging. Investigative Radiology, 50(4), pp. 218-227.

[Pe1992] Pekar, J., Moonen, C.T. and van Zijl, P., 1992. On the precision of diffusion/perfusion imaging by gradient sensitization. Magnetic Resonance in Medicine, 23(1), pp. 122-129.

[Pe2014] Petibon, Y., Huang, C., Ouyang, J., Reese, T.G., Li, Q., Syrkina, A., Chen, Y.L. and El Fakhri, G., 2014. Relative role of motion and PSF compensation in whole-body oncologic PET-MR imaging. Medical Physics, 41(4), p. 042503.

[Pi2013] J.D. Pintér, 2013. '1.2.2 "Globalized" Local Optimization Strategies, Combined with Grid Search or Random Search', in: Global optimization in action: continuous and Lipschitz optimization: algorithms, implementations and applications (Vol. 6). Springer Science & Business Media.

[Po2011] Le Pogam, A., Hatt, M., Descourt, P., Boussion, N., Tsoumpas, C., Turkheimer, F.E., Prunier-Aesch, C., Baulieu, J.L., Guilloteau, D. and Visvikis, D., 2011. Evaluation of a 3D local multiresolution algorithm for the correction of partial volume effects in positron emission tomography. Medical Physics, 38(9), pp. 4920-4933.

[PoHs1969] Pollack, I. and Hsieh, R., 1969. Sampling variability of the area under the ROC-curve and of d'_e. Psychological Bulletin, 71(3), pp. 161-173.

[PoRo1994] Politis, D.N. and Romano, J.P., 1994. The stationary bootstrap. Journal of the American Statistical Association, 89(428), pp. 1303-1313.

[Pr1999] Provenzale, J.M., Engelter, S.T., Petrella, J.R., Smith, J.S. and MacFall, J.R., 1999. Use of MR exponential diffusion-weighted images to eradicate T2 "shine-through" effect. AJR. American Journal of Roentgenology, 172(2), pp. 537-539.

[Pr2005] Prastawa, M., Gilmore, J.H., Lin, W. and Gerig, G., 2005. Automatic segmentation of MR images of the developing newborn brain. Medical Image Analysis, 9(5), pp. 457-466.

[Pr2009] Press, S.J., 2009. Subjective and objective Bayesian statistics: principles, models, and applications (Vol. 590). John Wiley & Sons, pp. 34-35.

[Pr2009b] Pretorius, P.H. and King, M.A., 2009. Diminishing the impact of the partial volume effect in cardiac SPECT perfusion imaging. Medical Physics, 36(1), pp. 105-115.

[Qu2004] Quarantelli, M., Berkouk, K., Prinster, A., Landeau, B., Svarer, C., Balkay, L., Alfano, B., Brunetti, A., Baron, J.C. and Salvatore, M., 2004. Integrated software for the analysis of brain PET/SPECT studies with partial-volume-effect correction. Journal of Nuclear Medicine, 45(2), pp. 192-201.

[Qu2012] Quentin, M., Blondin, D., Klasen, J., Lanzman, R.S., Miese, F.R., Arsov, C., Albers, P., Antoch, G. and Wittsack, H.J., 2012. Comparison of different mathematical models of diffusion-weighted prostate MR imaging. Magnetic Resonance Imaging, 30(10), pp. 1468-1474.

[Ra1917] J. Radon, 1917. Über die Bestimmung von Funktionen durch ihre Integralwerte langs gewisser Mannigfaltigkeiten, Berichte der Schsischen Akademie der Wissenschaften, 69, pp. 262-277.

[Ra2007] Rahmim, A., Rousset, O. and Zaidi, H., 2007. Strategies for motion tracking and correction in PET. PET Clinics, 2(2), pp. 251-266.

[Re2003] Reader, A.J., Julyan, P.J., Williams, H., Hastings, D.L. and Zweit, J., 2003. EM algorithm system modeling by image-space techniques for PET reconstruction. Nuclear Science, IEEE Transactions on, 50(5), pp. 1392-1397.

[Re2004] Reilhac, A., Lartizien, C., Costes, N., Sans, S., Comtat, C., Gunn, R.N. and Evans, A.C., 2004. PET-SORTEO: A Monte Carlo-based simulator with high count rate capabilities. Nuclear Science, IEEE Transactions on, 51(1), pp. 46-52.

[Re2005] Reinsberg, S.A., Brewster, J.M., Payne, G.S., Leach, M.O. and deSouza, N.M., 2005. Anisotropic diffusion in prostate cancer: fact or artefact. In Proceedings of the 13th Annual Meeting of ISMRM, p. 269.

[Re2016] Renaud, J.M., Klein, R. and Beanlands, R.S., 2016. Radionuclide Tracers for Myocardial Perfusion Imaging and Blood Flow Quantification. Cardiology Clinics, 34(1), pp. 37-46.

[Ri1972] Richardson, W.H., 1972. Bayesian-based iterative method of image restoration. Journal of the Optical Society of America, 62(1), pp. 55-59.

[Ri2009] Riches, S.F., Hawtin, K., Charles-Edwards, E.M. and De Souza, N.M., 2009. Diffusion-weighted imaging of the prostate and rectal wall: comparison of biexponential and monoexponential modelled diffusion and associated perfusion coefficients. NMR in Biomedicine, 22(3), pp. 318-325.

[Ro1998] Rousset, O.G., Ma, Y. and Evans, A.C., 1998. Correction for partial volume effects in PET: principle and validation. Journal of Nuclear Medicine, 39(5), pp. 904-911.

[Ro2000] Rousset, O.G., Deep, P., Kuwabara, H., Evans, A.C., Gjedde, A.H. and Cumming, P., 2000. Effect of partial volume correction on estimates of the influx and cerebral metabolism of 6-[18F] fluoro-L-dopa studied with PET in normal control and Parkinson's disease subjects. Synapse, 37(2), pp. 81-89.

[Ro2006] Rogers, D.W.O., 2006. Fifty years of Monte Carlo simulations for medical physics. Physics in Medicine and Biology, 51(13), pp. R287-R301.

[Ro2009] Rose, C.J., Mills, S.J., O'Connor, J.P., Buonaccorsi, G.A., Roberts, C., Watson, Y., Cheung, S., Zhao, S., Whitcher, B., Jackson, A. and Parker, G.J., 2009. Quantifying spatial heterogeneity in dynamic contrast-enhanced MRI parameter maps. Magnetic Resonance in Medicine, 62(2), pp. 488-499.

[Ro2011] Robin, X., Turck, N., Hainard, A., Tiberti, N., Lisacek, F., Sanchez, J.C. and Müller, M., 2011. pROC: an open-source package for R and S+ to analyze and compare ROC curves. BMC Bioinformatics, 12(1), p. 77.

[Ro2012] Rorden, C., Bonilha, L., Fridriksson, J., Bender, B. and Karnath, H.O., 2012. Age-specific CT and MRI templates for spatial normalization. Neuroimage, 61(4), pp. 957-965.

[Ro2012] Rosenkrantz, A.B., Sigmund, E.E., Johnson, G., Babb, J.S., Mussi, T.C., Melamed, J., Taneja, S.S., Lee, V.S. and Jensen, J.H., 2012. Prostate cancer: feasibility and preliminary experience of a diffusional kurtosis model for detection and assessment of aggressiveness of peripheral zone cancer. Radiology, 264(1), pp. 126-135.

[Ru2008] Ruscio, J., 2008. Constructing Confidence Intervals for Spearman's Rank Correlation with Ordinal Data: A Simulation Study Comparing Analytic and Bootstrap Methods. Journal of Modern Applied Statistical Methods, 7(2), pp. 416-434.

[Sa2007] Samuraki, M., Matsunari, I., Chen, W.P., Yajima, K., Yanase, D., Fujikawa, A., Takeda, N., Nishimura, S., Matsuda, H. and Yamada, M., 2007. Partial volume effect-corrected FDG PET and grey matter volume loss in patients with mild Alzheimer's disease. European Journal of Nuclear Medicine and Molecular Imaging, 34(10), pp. 1658-1669.

[Sa2009] Sawatzky, A., Brune, C., Müller, J. and Burger, M., 2009, January. Total variation processing of images with Poisson statistics. In Computer Analysis of Images and Patterns (pp. 533-540). Springer Berlin Heidelberg.

[Sa2011] Saritas, E.U., Lee, J.H. and Nishimura, D.G., 2011. SNR dependence of optimal parameters for apparent diffusion coefficient measurements. Medical Imaging, IEEE Transactions on, 30(2), pp. 424-437.

[Se2010] Segobin, S.H., Matthews, J.C., Markiewicz, P.J. and Herholz, K., 2010. A hybrid between region-based and voxel-based methods for partial volume correction in PET. In Nuclear Science Symposium Conference Record (NSS/MIC), pp. 3073-3078.

[Sh1982] Shepp, L.A. and Vardi, Y., 1982. Maximum likelihood reconstruction for emission tomography. Medical Imaging, IEEE Transactions on, 1(2), pp. 113-122.

[Sh2002] Shen, D. and Davatzikos, C., 2002. HAMMER: hierarchical attribute matching mechanism for elastic registration. Medical Imaging, IEEE Transactions on, 21(11), pp. 1421-1439.

[Sh2006] Shankar, L.K., Hoffman, J.M., Bacharach, S., Graham, M.M., Karp, J., Lammertsma, A.A., Larson, S., Mankoff, D.A., Siegel, B.A., Van den Abbeele, A. and Yap, J., 2006. Consensus recommendations for the use of 18F-FDG PET as an indicator of therapeutic response in patients in National Cancer Institute Trials. Journal of Nuclear Medicine, 47(6), pp. 1059-1066.

[Sh2009] Shidahara, M., Tsoumpas, C., Hammers, A., Boussion, N., Visvikis, D., Suhara, T., Kanno, I. and Turkheimer, F.E., 2009. Functional and structural synergy for resolution recovery and partial volume correction in brain PET. Neuroimage, 44(2), pp. 340-348.

[Sh2009b] Shi, F., Yap, P.T., Fan, Y., Cheng, J.Z., Wald, L.L., Gerig, G., Lin, W. and Shen, D., 2009, June. Cortical enhanced tissue segmentation of neonatal brain MR images acquired by a dedicated phased array coil. In Computer Vision and Pattern Recognition Workshops. CVPR Workshops 2009. IEEE Computer Society Conference on, pp. 39-45.

[Sh2009c] Shinmoto, H., Oshio, K., Tanimoto, A., Higuchi, N., Okuda, S., Kuribayashi, S. and Mulkern, R.V., 2009. Biexponential apparent diffusion coefficients in prostate cancer. Magnetic Resonance Imaging, 27(3), pp. 355-359.

[Sh2010] Shi, F., Fan, Y., Tang, S., Gilmore, J.H., Lin, W. and Shen, D., 2010. Neonatal brain image segmentation in longitudinal MRI studies. Neuroimage, 49(1), pp. 391-400.

[Sh2015] Shinmoto, H., Oshio, K., Tamura, C., Soga, S., Okamura, T., Yamada, K., Kaji, T. and Mulkern, R.V., 2015. Diffusion-weighted imaging of prostate cancer using a statistical model based on the gamma distribution. Journal of Magnetic Resonance Imaging, 42(1), pp. 56-62.

[ShFl1979] Shrout, P.E. and Fleiss, J.L., 1979. Intraclass correlations: uses in assessing rater reliability. Psychological Bulletin, 86(2), pp. 420-428.

[ShLo1974] Shepp, L.A. and Logan, B.F., 1974. The Fourier reconstruction of a head section. Nuclear Science, IEEE Transactions on, 21(3), pp. 21-43.

[Si2006] Sirola, N., 2006. Exhaustive global grid search in computing receiver position from modular satellite range measurements. In Journal of Physics: Conference Series, IOP Publishing, 52(1), pp. 73-82.

[So2007] Soret, M., Bacharach, S.L. and Buvat, I., 2007. Partial-volume effect in PET tumor imaging. Journal of Nuclear Medicine, 48(6), pp. 932-945.

[So2007b] Song, Z., Awate, S.P., Licht, D.J. and Gee, J.C., 2007. Clinical neonatal brain MRI segmentation using adaptive nonparametric data models and intensity-based Markov priors. In Medical Image Computing and Computer-Assisted Intervention-MICCAI 2007, Springer Berlin Heidelberg, pp. 883-890.

[SpNe2010] Spiess, A.N. and Neumeyer, N., 2010. An evaluation of R^2 as an inadequate measure for nonlinear models in pharmacological and biochemical research: a Monte Carlo approach. BMC Pharmacology, 10(1), p. 6.

[Sr2012] Srhoj-Egekher, V., Benders, M.J.N.L., Kersbergen, K.J., Viergever, M.A. and Isgum, I., 2012. Automatic segmentation of neonatal brain MRI using atlas based segmentation and machine learning approach. MICCAI Grand Challenge: Neonatal Brain Segmentation, 2012.

[StTa1965] Stejskal, E.O. and Tanner, J.E., 1965. Spin diffusion measurements: spin echoes in the presence of a time-dependent field gradient. The Journal of Chemical Physics, 42(1), pp. 288-292.

[Su1978] Sugiura, N., 1978. Further analysts of the data by akaike's information criterion and the finite corrections: Further analysts of the data by akaike's. Communications in Statistics-Theory and Methods, 7(1), pp. 13-26.

[Ta2011] Tan, C.H., Wang, J. and Kundra, V., 2011. Diffusion weighted imaging in prostate cancer. European Radiology, 21(3), pp. 593-603.

[Te2007] Teo, B.K., Seo, Y., Bacharach, S.L., Carrasquillo, J.A., Libutti, S.K., Shukla, H., Hasegawa, B.H., Hawkins, R.A. and Franc, B.L., 2007. Partial-volume correction in PET: validation of an iterative postreconstruction method with phantom and patient data. Journal of Nuclear Medicine, 48(5), pp. 802-810.

[Th2001] Thiel, A., Reilhac, A., Collins, D.L., Rousset, O., Neelin, P. and Evans, A.C., 2001. Volume-of-interest-based automated partial volume correction for large numbers of PET data sets. BrainPET, Taipei, Taiwan.

[Th2007] Thoeny, H.C. and De Keyzer, F., 2007. Extracranial applications of diffusion-weighted magnetic resonance imaging. European Radiology, 17(6), pp. 1385-1393.

[Th2011] Thomas, B.A., Erlandsson, K., Modat, M., Thurfjell, L., Vandenberghe, R., Ourselin, S. and Hutton, B.F., 2011. The importance of appropriate partial volume correction for PET quantification in AlzheimerŠs disease. European Journal of Nuclear Medicine and Molecular Imaging, 38(6), pp. 1104-1119.

[To1956] Torrey, H.C., 1956. Bloch equations with diffusion terms. Physical Review, 104(3), pp. 563-565.

[To1995] Toft, P.B., Leth, H., Ring, P.B., Peitersen, B., Lou, H.C. and Henriksen, O., 1995. Volumetric analysis of the normal infant brain and in intrauterine growth retardation. Early Human Development, 43(1), pp. 15-29.

[ToRe2008] Tohka, J. and Reilhac, A., 2008. Deconvolution-based partial volume correction in Raclopride-PET and Monte Carlo comparison to MR-based method. Neuroimage, 39(4), pp. 1570-1584.

[Tu1958] Tukey, J.W., 1958. Bias and confidence in not-quite large samples (Abstract). In Annals of Mathematical Statistics 29(2), p. 614

[Tu2011] Turkbey, B., Shah, V.P., Pang, Y., Bernardo, M., Xu, S., Kruecker, J., Locklin, J., Baccala Jr, A.A., Rastinehad, A.R., Merino, M.J. and Shih, J.H., 2011. Is apparent diffusion coefficient associated with clinical risk scores for prostate cancers that are visible on 3-T MR images?. Radiology, 258(2), pp. 488-495.

[Ty2010] Tylski, P., Stute, S., Grotus, N., Doyeux, K., Hapdey, S., Gardin, I., Vanderlinden, B. and Buvat, I., 2010. Comparative assessment of methods for estimating tumor volume and standardized uptake value in 18F-FDG PET. Journal of Nuclear Medicine, 51(2), pp. 268-276.

[Ue2013] Ueno, Y., Takahashi, S., Kitajima, K., Kimura, T., Aoki, I., Kawakami, F., Miyake, H., Ohno, Y. and Sugimura, K., 2013. Computed diffusion-weighted imaging using 3-T magnetic resonance imaging for prostate cancer diagnosis. European Radiology, 23(12), pp. 3509-3516.

[Uk2002] Ukoumunne, O.C., 2002. A comparison of confidence interval methods for the intraclass correlation coefficient in cluster randomized trials. Statistics in Medicine, 21(24), pp. 3757-3774.

[Va1931] Van Cittert P.H., 1931. Zum EinFluß der Spaltbreite auf die Intensitätsverteilung in Spektrallinien. Zeuschrift Für Physik, 69, pp. 298-308.

[Va2006] Vandenberghe, S., Staelens, S., Byrne, C.L., Soares, E.J., Lemahieu, I. and Glick, S.J., 2006. Reconstruction of 2D PET data with Monte Carlo generated system matrix for generalized natural pixels. Physics in Medicine and Biology, 51(12), pp. 3105-3125.

[Va2011] Vargas, H.A., Akin, O., Franiel, T., Mazaheri, Y., Zheng, J., Moskowitz, C., Udo, K., Eastham, J. and Hricak, H., 2011. Diffusion-weighted endorectal MR imaging at 3 T for prostate cancer: tumor detection and assessment of aggressiveness. Radiology, 259(3), pp. 775-784.

[Va2015] Valverde, S., Oliver, A., Cabezas, M., Roura, E. and Lladó, X., 2015. Comparison of 10 brain tissue segmentation methods using revisited IBSR annotations. Journal of Magnetic Resonance Imaging, 41(1), pp. 93-101.

[Ve2011] Verma, S. and Rajesh, A., 2011. A clinically relevant approach to imaging prostate cancer: review. American Journal of Roentgenology, 196(3_supplement), pp. S1-S10.

[Vi2008] Viswanath, S., Bloch, B.N., Genega, E., Rofsky, N., Lenkinski, R., Chappelow, J., Toth, R. and Madabhushi, A., 2008. A comprehensive segmentation, registration, and cancer detection scheme on 3 Tesla in vivo prostate DCE-MRI. In Medical Image Computing and Computer-Assisted Intervention-MICCAI 2008, Springer Berlin Heidelberg, pp. 662-669.

[Wa2000] Warfield, S.K., Kaus, M., Jolesz, F.A. and Kikinis, R., 2000. Adaptive, template moderated, spatially varying statistical classification. Medical Image Analysis, 4(1), pp. 43-55.

[Wa2012] Wang, H. and Fei, B., 2012. An MR image-guided, voxel-based partial volume correction method for PET images. Medical Physics, 39(1), pp. 179-194.

[Wa2014] Wang, L., Shi, F., Li, G., Gao, Y., Lin, W., Gilmore, J.H. and Shen, D., 2014. Segmentation of neonatal brain MR images using patch-driven level sets. NeuroImage, 84, pp. 141-158.

[WaKuSc2012] Wang, S., Kuklisova-Murgasova, M. and Schnabel, J.A., 2012. An atlas-based method for neonatal MR brain tissue segmentation. Proceedings of the MICCAI Grand Challenge: Neonatal Brain Segmentation, pp. 28-35.

[We2006] Weisenfeld, N.I., Mewes, A.U. and Warfield, S.K., 2006. Highly accurate segmentation of brain tissue and subcortical gray matter from newborn MRI. In Medical Image Computing and Computer-Assisted Intervention MICCAI 2006, Springer Berlin Heidelberg, pp. 199-206.

[We2009] Weisenfeld, N.I. and Warfield, S.K., 2009. Automatic segmentation of newborn brain MRI. Neuroimage, 47(2), pp. 564-572.

[Wi2010] Wittsack, H.J., Lanzman, R.S., Mathys, C., Janssen, H., Mödder, U. and Blondin, D., 2010. Statistical evaluation of diffusion-weighted imaging of the human kidney. Magnetic Resonance in Medicine, 64(2), pp. 616-622.

[Wu2015] Wu, W.C., Chen, Y.F., Tseng, H.M. and Yang, S.C., 2015. Caveat of measuring perfusion indexes using intravoxel incoherent motion magnetic resonance imaging in the human brain. European Radiology, 25(8), pp. 2485-2492.

[Xu2007] Xue, H., Srinivasan, L., Jiang, S., Rutherford, M., Edwards, A.D., Rueckert, D. and Hajnal, J.V., 2007. Automatic segmentation and reconstruction of the cortex from neonatal MRI. Neuroimage, 38(3), pp. 461-477.

[Xu2014] Xu, X.G., 2014. An exponential growth of computational phantom research in radiation protection, imaging, and radiotherapy: a review of the fifty-year history. Physics in Medicine and Biology, 59(18), pp. R233-R302.

[Xu2015] Xu, Z., Bagci, U., Gao, M. and Mollura, D.J., 2015. Highly Precise Partial Volume Correction for PET Images: An Iterative Approach via Shape Consistency, in: IEEE 10th International Symposium of Biomedical Imaging, NY, USA.

[Ya2010] Yang, X.S., 2010. Engineering optimization: an introduction with metaheuristic applications. John Wiley & Sons.

[Ya2013] Yan, X., Zhou, M., Ying, L., Yin, D., Fan, M., Yang, G., Zhou, Y., Song, F. and Xu, D., 2013. Evaluation of optimized b-value sampling schemas for diffusion kurtosis imaging with an application to stroke patient data. Computerized Medical Imaging and Graphics, 37(4), pp. 272-280.

[Za2006] Zaitsev, M., Dold, C., Sakas, G., Hennig, J. and Speck, O., 2006. Magnetic resonance imaging of freely moving objects: prospective real-time motion correction using an external optical motion tracking system. Neuroimage, 31(3), pp. 1038-1050.

[Za2006b] Zaidi, H., Ruest, T., Schoenahl, F. and Montandon, M.L., 2006. Comparative assessment of statistical brain MR image segmentation algorithms and their impact on partial volume correction in PET. Neuroimage, 32(4), pp. 1591-1607.

[Zh2012] Zhigljavsky, A.A., 2012. Theory of global random search (Vol. 65). Springer Science & Business Media.

[Zh2012b] Zhang, J.L., Sigmund, E.E., Rusinek, H., Chandarana, H., Storey, P., Chen, Q. and Lee, V.S., 2012. Optimization of b-value sampling for diffusion-weighted imaging of the kidney. Magnetic Resonance in Medicine, 67(1), pp. 89-97.

[Zh2015] Zhang, Y.-D., Wang Q., Wu, C.-J., Wang, X.-N., Zhang, J. Liu, H., Liu, X.-S., Shi, H.-B., 2015. The Histogram Analysis of Diffusion-Weighted Intravoxel Incoherent Motion (IVIM) Imaging for Differentiating the Gleason garde of Prostate Cancer. Eruopean Radiology, 25(4), pp. 994-1004.

[Zo2013] Zou, G.Y. and Yue, L., 2013. Using confidence intervals to compare several correlated areas under the receiver operating characteristic curves. Statistics in Medicine, 32(29), pp. 5077-5090.

Original Publications

Publication I

Merisaari H., Teräs M., Hirvonen J., Nevalainen O.S., Hietala J., 2007. Evaluation of partial volume effect correction methods for brain positron emission tomography: Quantification and reproducibility, Journal of Medical Physics, 32(3), pp.108-117.

The web page of the article:
http://www.ncbi.nlm.nih.gov/pmc/articles/PMC3000501

Publication II

Merisaari H., Parkkola R., Alhoniemi E., Teräs M., Lehtonen L., Haataja L., Lapinleimu H., Nevalainen O.S., 2009. Gaussian mixture model-based segmentation of MR images taken from premature infant brains, Journal of Neuroscience Methods, 182(1), pp.110-122.

Publication III

Jambor I., Merisaari H., Aronen H.J., Järvinen J., Saunavaara J., Kauko T., Borra R., Pesola M., 2014. Optimization of b-value distribution for biexponential diffusion-weighted MR imaging of normal prostate, Journal of Magnetic Resonance Imaging, 39(5), pp.1213-1222.

Publication IV

Jambor I., Merisaari H., Taimen P., Boström P., Minn H., Pesola M., Aronen H.J., 2014. Evaluation of different mathematical models for diffusion-weighted imaging of normal prostate and prostate cancer using high b-values: A repeatability study, Magnetic Resonance in Medicine, 73(5), pp.1988-1998.

Publication V

Merisaari H., Jambor I., 2014. Optimization of b-value distribution for four mathematical models of prostate cancer diffusion-weighted imaging using b values up to 2000sec/mm^2: Simulation and repeatability study, Magnetic Resonance in Medicine, 73(5), pp.1954-1969.

Publication VI

Toivonen J., Merisaari H., Pesola M., Taimen P., Boström P.J., Pahikkala T., Aronen H.J., Jambor I., 2015. Mathematical models for diffusion-weighted imaging of prostate cancer using b values up to 2000sec/mm^2: Correlation with Gleason score and repeatability of region of interest analysis, Magnetic Resonance in Medicine, 74(4), pp.1116-1124.

Turku Centre for Computer Science
TUCS Dissertations

1. **Marjo Lipponen**, On Primitive Solutions of the Post Correspondence Problem
2. **Timo Käkölä**, Dual Information Systems in Hyperknowledge Organizations
3. **Ville Leppänen**, Studies on the Realization of PRAM
4. **Cunsheng Ding**, Cryptographic Counter Generators
5. **Sami Viitanen**, Some New Global Optimization Algorithms
6. **Tapio Salakoski**, Representative Classification of Protein Structures
7. **Thomas Långbacka**, An Interactive Environment Supporting the Development of Formally Correct Programs
8. **Thomas Finne**, A Decision Support System for Improving Information Security
9. **Valeria Mihalache**, Cooperation, Communication, Control. Investigations on Grammar Systems.
10. **Marina Waldén**, Formal Reasoning About Distributed Algorithms
11. **Tero Laihonen**, Estimates on the Covering Radius When the Dual Distance is Known
12. **Lucian Ilie**, Decision Problems on Orders of Words
13. **Jukkapekka Hekanaho**, An Evolutionary Approach to Concept Learning
14. **Jouni Järvinen**, Knowledge Representation and Rough Sets
15. **Tomi Pasanen**, In-Place Algorithms for Sorting Problems
16. **Mika Johnsson**, Operational and Tactical Level Optimization in Printed Circuit Board Assembly
17. **Mats Aspnäs**, Multiprocessor Architecture and Programming: The Hathi-2 System
18. **Anna Mikhajlova**, Ensuring Correctness of Object and Component Systems
19. **Vesa Torvinen**, Construction and Evaluation of the Labour Game Method
20. **Jorma Boberg**, Cluster Analysis. A Mathematical Approach with Applications to Protein Structures
21. **Leonid Mikhajlov**, Software Reuse Mechanisms and Techniques: Safety Versus Flexibility
22. **Timo Kaukoranta**, Iterative and Hierarchical Methods for Codebook Generation in Vector Quantization
23. **Gábor Magyar**, On Solution Approaches for Some Industrially Motivated Combinatorial Optimization Problems
24. **Linas Laibinis**, Mechanised Formal Reasoning About Modular Programs
25. **Shuhua Liu**, Improving Executive Support in Strategic Scanning with Software Agent Systems
26. **Jaakko Järvi**, New Techniques in Generic Programming – C++ is more Intentional than Intended
27. **Jan-Christian Lehtinen**, Reproducing Kernel Splines in the Analysis of Medical Data
28. **Martin Büchi**, Safe Language Mechanisms for Modularization and Concurrency
29. **Elena Troubitsyna**, Stepwise Development of Dependable Systems
30. **Janne Näppi**, Computer-Assisted Diagnosis of Breast Calcifications
31. **Jianming Liang**, Dynamic Chest Images Analysis
32. **Tiberiu Seceleanu**, Systematic Design of Synchronous Digital Circuits
33. **Tero Aittokallio**, Characterization and Modelling of the Cardiorespiratory System in Sleep-Disordered Breathing
34. **Ivan Porres**, Modeling and Analyzing Software Behavior in UML
35. **Mauno Rönkkö**, Stepwise Development of Hybrid Systems
36. **Jouni Smed**, Production Planning in Printed Circuit Board Assembly
37. **Vesa Halava**, The Post Correspondence Problem for Market Morphisms
38. **Ion Petre**, Commutation Problems on Sets of Words and Formal Power Series
39. **Vladimir Kvassov**, Information Technology and the Productivity of Managerial Work
40. **Frank Tétard**, Managers, Fragmentation of Working Time, and Information Systems

41. **Jan Manuch**, Defect Theorems and Infinite Words
42. **Kalle Ranto**, Z_4-Goethals Codes, Decoding and Designs
43. **Arto Lepistö**, On Relations Between Local and Global Periodicity
44. **Mika Hirvensalo**, Studies on Boolean Functions Related to Quantum Computing
45. **Pentti Virtanen**, Measuring and Improving Component-Based Software Development
46. **Adekunle Okunoye**, Knowledge Management and Global Diversity – A Framework to Support Organisations in Developing Countries
47. **Antonina Kloptchenko**, Text Mining Based on the Prototype Matching Method
48. **Juha Kivijärvi**, Optimization Methods for Clustering
49. **Rimvydas Rukšėnas**, Formal Development of Concurrent Components
50. **Dirk Nowotka**, Periodicity and Unbordered Factors of Words
51. **Attila Gyenesei**, Discovering Frequent Fuzzy Patterns in Relations of Quantitative Attributes
52. **Petteri Kaitovaara**, Packaging of IT Services – Conceptual and Empirical Studies
53. **Petri Rosendahl**, Niho Type Cross-Correlation Functions and Related Equations
54. **Péter Majlender**, A Normative Approach to Possibility Theory and Soft Decision Support
55. **Seppo Virtanen**, A Framework for Rapid Design and Evaluation of Protocol Processors
56. **Tomas Eklund**, The Self-Organizing Map in Financial Benchmarking
57. **Mikael Collan**, Giga-Investments: Modelling the Valuation of Very Large Industrial Real Investments
58. **Dag Björklund**, A Kernel Language for Unified Code Synthesis
59. **Shengnan Han**, Understanding User Adoption of Mobile Technology: Focusing on Physicians in Finland
60. **Irina Georgescu**, Rational Choice and Revealed Preference: A Fuzzy Approach
61. **Ping Yan**, Limit Cycles for Generalized Liénard-Type and Lotka-Volterra Systems
62. **Joonas Lehtinen**, Coding of Wavelet-Transformed Images
63. **Tommi Meskanen,** On the NTRU Cryptosystem
64. **Saeed Salehi**, Varieties of Tree Languages
65. **Jukka Arvo**, Efficient Algorithms for Hardware-Accelerated Shadow Computation
66. **Mika Hirvikorpi**, On the Tactical Level Production Planning in Flexible Manufacturing Systems
67. **Adrian Costea**, Computational Intelligence Methods for Quantitative Data Mining
68. **Cristina Seceleanu**, A Methodology for Constructing Correct Reactive Systems
69. **Luigia Petre**, Modeling with Action Systems
70. **Lu Yan**, Systematic Design of Ubiquitous Systems
71. **Mehran Gomari**, On the Generalization Ability of Bayesian Neural Networks
72. **Ville Harkke**, Knowledge Freedom for Medical Professionals – An Evaluation Study of a Mobile Information System for Physicians in Finland
73. **Marius Cosmin Codrea**, Pattern Analysis of Chlorophyll Fluorescence Signals
74. **Aiying Rong**, Cogeneration Planning Under the Deregulated Power Market and Emissions Trading Scheme
75. **Chihab BenMoussa**, Supporting the Sales Force through Mobile Information and Communication Technologies: Focusing on the Pharmaceutical Sales Force
76. **Jussi Salmi**, Improving Data Analysis in Proteomics
77. **Orieta Celiku**, Mechanized Reasoning for Dually-Nondeterministic and Probabilistic Programs
78. **Kaj-Mikael Björk**, Supply Chain Efficiency with Some Forest Industry Improvements
79. **Viorel Preoteasa**, Program Variables – The Core of Mechanical Reasoning about Imperative Programs
80. **Jonne Poikonen**, Absolute Value Extraction and Order Statistic Filtering for a Mixed-Mode Array Image Processor
81. **Luka Milovanov**, Agile Software Development in an Academic Environment
82. **Francisco Augusto Alcaraz Garcia**, Real Options, Default Risk and Soft Applications
83. **Kai K. Kimppa**, Problems with the Justification of Intellectual Property Rights in Relation to Software and Other Digitally Distributable Media
84. **Dragoş Truşcan**, Model Driven Development of Programmable Architectures
85. **Eugen Czeizler**, The Inverse Neighborhood Problem and Applications of Welch Sets in Automata Theory

86. **Sanna Ranto**, Identifying and Locating-Dominating Codes in Binary Hamming Spaces
87. **Tuomas Hakkarainen**, On the Computation of the Class Numbers of Real Abelian Fields
88. **Elena Czeizler**, Intricacies of Word Equations
89. **Marcus Alanen**, A Metamodeling Framework for Software Engineering
90. **Filip Ginter**, Towards Information Extraction in the Biomedical Domain: Methods and Resources
91. **Jarkko Paavola**, Signature Ensembles and Receiver Structures for Oversaturated Synchronous DS-CDMA Systems
92. **Arho Virkki**, The Human Respiratory System: Modelling, Analysis and Control
93. **Olli Luoma**, Efficient Methods for Storing and Querying XML Data with Relational Databases
94. **Dubravka Ilić**, Formal Reasoning about Dependability in Model-Driven Development
95. **Kim Solin**, Abstract Algebra of Program Refinement
96. **Tomi Westerlund**, Time Aware Modelling and Analysis of Systems-on-Chip
97. **Kalle Saari**, On the Frequency and Periodicity of Infinite Words
98. **Tomi Kärki**, Similarity Relations on Words: Relational Codes and Periods
99. **Markus M. Mäkelä**, Essays on Software Product Development: A Strategic Management Viewpoint
100. **Roope Vehkalahti**, Class Field Theoretic Methods in the Design of Lattice Signal Constellations
101. **Anne-Maria Ernvall-Hytönen**, On Short Exponential Sums Involving Fourier Coefficients of Holomorphic Cusp Forms
102. **Chang Li**, Parallelism and Complexity in Gene Assembly
103. **Tapio Pahikkala**, New Kernel Functions and Learning Methods for Text and Data Mining
104. **Denis Shestakov**, Search Interfaces on the Web: Querying and Characterizing
105. **Sampo Pyysalo**, A Dependency Parsing Approach to Biomedical Text Mining
106. **Anna Sell**, Mobile Digital Calendars in Knowledge Work
107. **Dorina Marghescu**, Evaluating Multidimensional Visualization Techniques in Data Mining Tasks
108. **Tero Säntti**, A Co-Processor Approach for Efficient Java Execution in Embedded Systems
109. **Kari Salonen**, Setup Optimization in High-Mix Surface Mount PCB Assembly
110. **Pontus Boström**, Formal Design and Verification of Systems Using Domain-Specific Languages
111. **Camilla J. Hollanti**, Order-Theoretic Mehtods for Space-Time Coding: Symmetric and Asymmetric Designs
112. **Heidi Himmanen**, On Transmission System Design for Wireless Broadcasting
113. **Sébastien Lafond**, Simulation of Embedded Systems for Energy Consumption Estimation
114. **Evgeni Tsivtsivadze**, Learning Preferences with Kernel-Based Methods
115. **Petri Salmela**, On Commutation and Conjugacy of Rational Languages and the Fixed Point Method
116. **Siamak Taati**, Conservation Laws in Cellular Automata
117. **Vladimir Rogojin**, Gene Assembly in Stichotrichous Ciliates: Elementary Operations, Parallelism and Computation
118. **Alexey Dudkov**, Chip and Signature Interleaving in DS CDMA Systems
119. **Janne Savela**, Role of Selected Spectral Attributes in the Perception of Synthetic Vowels
120. **Kristian Nybom**, Low-Density Parity-Check Codes for Wireless Datacast Networks
121. **Johanna Tuominen**, Formal Power Analysis of Systems-on-Chip
122. **Teijo Lehtonen**, On Fault Tolerance Methods for Networks-on-Chip
123. **Eeva Suvitie**, On Inner Products Involving Holomorphic Cusp Forms and Maass Forms
124. **Linda Mannila**, Teaching Mathematics and Programming – New Approaches with Empirical Evaluation
125. **Hanna Suominen**, Machine Learning and Clinical Text: Supporting Health Information Flow
126. **Tuomo Saarni**, Segmental Durations of Speech
127. **Johannes Eriksson**, Tool-Supported Invariant-Based Programming

128. **Tero Jokela**, Design and Analysis of Forward Error Control Coding and Signaling for Guaranteeing QoS in Wireless Broadcast Systems
129. **Ville Lukkarila**, On Undecidable Dynamical Properties of Reversible One-Dimensional Cellular Automata
130. **Qaisar Ahmad Malik**, Combining Model-Based Testing and Stepwise Formal Development
131. **Mikko-Jussi Laakso**, Promoting Programming Learning: Engagement, Automatic Assessment with Immediate Feedback in Visualizations
132. **Riikka Vuokko**, A Practice Perspective on Organizational Implementation of Information Technology
133. **Jeanette Heidenberg**, Towards Increased Productivity and Quality in Software Development Using Agile, Lean and Collaborative Approaches
134. **Yong Liu**, Solving the Puzzle of Mobile Learning Adoption
135. **Stina Ojala**, Towards an Integrative Information Society: Studies on Individuality in Speech and Sign
136. **Matteo Brunelli**, Some Advances in Mathematical Models for Preference Relations
137. **Ville Junnila**, On Identifying and Locating-Dominating Codes
138. **Andrzej Mizera**, Methods for Construction and Analysis of Computational Models in Systems Biology. Applications to the Modelling of the Heat Shock Response and the Self-Assembly of Intermediate Filaments.
139. **Csaba Ráduly-Baka**, Algorithmic Solutions for Combinatorial Problems in Resource Management of Manufacturing Environments
140. **Jari Kyngäs**, Solving Challenging Real-World Scheduling Problems
141. **Arho Suominen**, Notes on Emerging Technologies
142. **József Mezei**, A Quantitative View on Fuzzy Numbers
143. **Marta Olszewska**, On the Impact of Rigorous Approaches on the Quality of Development
144. **Antti Airola**, Kernel-Based Ranking: Methods for Learning and Performace Estimation
145. **Aleksi Saarela**, Word Equations and Related Topics: Independence, Decidability and Characterizations
146. **Lasse Bergroth**, Kahden merkkijonon pisimmän yhteisen alijonon ongelma ja sen ratkaiseminen
147. **Thomas Canhao Xu**, Hardware/Software Co-Design for Multicore Architectures
148. **Tuomas Mäkilä**, Software Development Process Modeling – Developers Perspective to Contemporary Modeling Techniques
149. **Shahrokh Nikou**, Opening the Black-Box of IT Artifacts: Looking into Mobile Service Characteristics and Individual Perception
150. **Alessandro Buoni**, Fraud Detection in the Banking Sector: A Multi-Agent Approach
151. **Mats Neovius**, Trustworthy Context Dependency in Ubiquitous Systems
152. **Fredrik Degerlund**, Scheduling of Guarded Command Based Models
153. **Amir-Mohammad Rahmani-Sane**, Exploration and Design of Power-Efficient Networked Many-Core Systems
154. **Ville Rantala**, On Dynamic Monitoring Methods for Networks-on-Chip
155. **Mikko Pelto**, On Identifying and Locating-Dominating Codes in the Infinite King Grid
156. **Anton Tarasyuk**, Formal Development and Quantitative Verification of Dependable Systems
157. **Muhammad Mohsin Saleemi**, Towards Combining Interactive Mobile TV and Smart Spaces: Architectures, Tools and Application Development
158. **Tommi J. M. Lehtinen**, Numbers and Languages
159. **Peter Sarlin**, Mapping Financial Stability
160. **Alexander Wei Yin**, On Energy Efficient Computing Platforms
161. **Mikołaj Olszewski**, Scaling Up Stepwise Feature Introduction to Construction of Large Software Systems
162. **Maryam Kamali**, Reusable Formal Architectures for Networked Systems
163. **Zhiyuan Yao**, Visual Customer Segmentation and Behavior Analysis – A SOM-Based Approach
164. **Timo Jolivet**, Combinatorics of Pisot Substitutions
165. **Rajeev Kumar Kanth**, Analysis and Life Cycle Assessment of Printed Antennas for Sustainable Wireless Systems
166. **Khalid Latif**, Design Space Exploration for MPSoC Architectures

167. **Bo Yang**, Towards Optimal Application Mapping for Energy-Efficient Many-Core Platforms
168. **Ali Hanzala Khan**, Consistency of UML Based Designs Using Ontology Reasoners
169. **Sonja Leskinen**, m-Equine: IS Support for the Horse Industry
170. **Fareed Ahmed Jokhio**, Video Transcoding in a Distributed Cloud Computing Environment
171. **Moazzam Fareed Niazi**, A Model-Based Development and Verification Framework for Distributed System-on-Chip Architecture
172. **Mari Huova**, Combinatorics on Words: New Aspects on Avoidability, Defect Effect, Equations and Palindromes
173. **Ville Timonen**, Scalable Algorithms for Height Field Illumination
174. **Henri Korvela**, Virtual Communities – A Virtual Treasure Trove for End-User Developers
175. **Kameswar Rao Vaddina**, Thermal-Aware Networked Many-Core Systems
176. **Janne Lahtiranta**, New and Emerging Challenges of the ICT-Mediated Health and Well-Being Services
177. **Irum Rauf**, Design and Validation of Stateful Composite RESTful Web Services
178. **Jari Björne**, Biomedical Event Extraction with Machine Learning
179. **Katri Haverinen**, Natural Language Processing Resources for Finnish: Corpus Development in the General and Clinical Domains
180. **Ville Salo**, Subshifts with Simple Cellular Automata
181. **Johan Ersfolk**, Scheduling Dynamic Dataflow Graphs
182. **Hongyan Liu**, On Advancing Business Intelligence in the Electricity Retail Market
183. **Adnan Ashraf**, Cost-Efficient Virtual Machine Management: Provisioning, Admission Control, and Consolidation
184. **Muhammad Nazrul Islam**, Design and Evaluation of Web Interface Signs to Improve Web Usability: A Semiotic Framework
185. **Johannes Tuikkala**, Algorithmic Techniques in Gene Expression Processing: From Imputation to Visualization
186. **Natalia Díaz Rodríguez**, Semantic and Fuzzy Modelling for Human Behaviour Recognition in Smart Spaces. A Case Study on Ambient Assisted Living
187. **Mikko Pänkäälä**, Potential and Challenges of Analog Reconfigurable Computation in Modern and Future CMOS
188. **Sami Hyrynsalmi**, Letters from the War of Ecosystems – An Analysis of Independent Software Vendors in Mobile Application Marketplaces
189. **Seppo Pulkkinen**, Efficient Optimization Algorithms for Nonlinear Data Analysis
190. **Sami Pyöttiälä**, Optimization and Measuring Techniques for Collect-and-Place Machines in Printed Circuit Board Industry
191. **Syed Mohammad Asad Hassan Jafri**, Virtual Runtime Application Partitions for Resource Management in Massively Parallel Architectures
192. **Toni Ernvall**, On Distributed Storage Codes
193. **Yuliya Prokhorova**, Rigorous Development of Safety-Critical Systems
194. **Olli Lahdenoja**, Local Binary Patterns in Focal-Plane Processing – Analysis and Applications
195. **Annika H. Holmbom**, Visual Analytics for Behavioral and Niche Market Segmentation
196. **Sergey Ostroumov**, Agent-Based Management System for Many-Core Platforms: Rigorous Design and Efficient Implementation
197. **Espen Suenson**, How Computer Programmers Work – Understanding Software Development in Practise
198. **Tuomas Poikela**, Readout Architectures for Hybrid Pixel Detector Readout Chips
199. **Bogdan Iancu**, Quantitative Refinement of Reaction-Based Biomodels
200. **Ilkka Törmä**, Structural and Computational Existence Results for Multidimensional Subshifts
201. **Sebastian Okser**, Scalable Feature Selection Applications for Genome-Wide Association Studies of Complex Diseases
202. **Fredrik Abbors**, Model-Based Testing of Software Systems: Functionality and Performance
203. **Inna Pereverzeva**, Formal Development of Resilient Distributed Systems
204. **Mikhail Barash**, Defining Contexts in Context-Free Grammars
205. **Sepinoud Azimi**, Computational Models for and from Biology: Simple Gene Assembly and Reaction Systems
206. **Petter Sandvik**, Formal Modelling for Digital Media Distribution

207. **Jongyun Moon**, Hydrogen Sensor Application of Anodic Titanium Oxide Nanostructures
208. **Simon Holmbacka**, Energy Aware Software for Many-Core Systems
209. **Charalampos Zinoviadis**, Hierarchy and Expansiveness in Two-Dimensional Subshifts of Finite Type
210. **Mika Murtojärvi**, Efficient Algorithms for Coastal Geographic Problems
211. **Sami Mäkelä**, Cohesion Metrics for Improving Software Quality
212. **Eyal Eshet**, Examining Human-Centered Design Practice in the Mobile Apps Era
213. **Jetro Vesti**, Rich Words and Balanced Words
214. **Jarkko Peltomäki**, Privileged Words and Sturmian Words
215. **Fahimeh Farahnakian**, Energy and Performance Management of Virtual Machines: Provisioning, Placement and Consolidation
216. **Diana-Elena Gratie**, Refinement of Biomodels Using Petri Nets
217. **Harri Merisaari**, Algorithmic Analysis Techniques for Molecular Imaging

Turku
Centre *for*
Computer
Science

http://www. tucs.fi

tucs@abo.fi

University of Turku
Faculty of Mathematics and Natural Sciences
- Department of Information Technology
- Department of Mathematics and Statistics

Turku School of Economics
- Institute of Information Systems Science

Åbo Akademi University
Faculty of Science and Engineering
- Computer Engineering
- Computer Science

Faculty of Social Sciences, Business and Economics
- Information Systems

ISBN 978-952-12-3442-2
ISSN 1239-1883

Harri Merisaari

Algorithmic Analysis Techniques for Molecular Imaging

Harri Merisaari

Algorithmic Analysis Techniques for Molecular Imaging